

Highlights

- Review of nadir UV-VIS space-borne instruments for monitoring of atmospheric composition
- Description of trace gase retrieval techniques in the UV-VIS spectral range
- Summary of ozone, nitrogen dioxide, sulfur dioxide, formaldehyde, bromine monoxide, water vapor and glyoxal retrievals developed since 1970
- Illustration of the scientific and societal applications of these retrievals
- Recommendations and challenges in the following decade

Five decades observing Earth's atmospheric trace gases using ultraviolet and visible backscatter solar radiation from space

Gonzalo Gonzalez Abad^{a,*}, Amir Hossein Souri^a, Juseon Bak^a, Kelly Chance^a, Lawrence E. Flynn^b, Nickolay A. Krotkov^c, Lok Lamsal^c, Can Li^{c,d}, Xiong Liu^a, Christopher Chan Miller^a, Caroline R. Nowlan^a, Raid Suleiman^a, Huiqun Wang^a

^a*Harvard-Smithsonian Center for Astrophysics, Cambridge, MA 02138, USA*

^b*NOAA, College Park, MD 20740, USA*

^c*NASA Goddard Space Flight Center, Greenbelt, MD 20771, USA*

^d*Earth System Science Interdisciplinary Center, University of Maryland, College Park, MD 20742, USA*

Abstract

Over the last five decades, Earth's atmosphere has been extensively monitored from space using different spectral ranges. Early efforts were directed at improving weather forecasts with the first meteorological satellites launched in the 1960s. Soon thereafter, the intersection between weather, climate and atmospheric chemistry led to the observation of atmospheric composition from space. During the 1970s the Nimbus satellite program started regular monitoring of ozone integrated columns and water vapor profiles using the Backscatter Ultraviolet Spectrometer, the Infrared Interferometer Spectrometer and the Satellite Infrared Spectrometer instruments. Five decades after these pioneer efforts, continuous progress in instrument design, and retrieval techniques allow researchers to monitor tropospheric concentrations of a wide range of species with implications for air quality, climate and weather.

The time line of historic, present and future space-borne instruments measuring ultraviolet and visible backscattered solar radiation designed to quantify

*Corresponding author at: Harvard-Smithsonian Center for Astrophysics, 60 Garden Street, Cambridge, MA 02138, USA

Email address: ggonzalezabad@cfa.harvard.edu (Gonzalo Gonzalez Abad)

atmospheric trace gases is presented. We describe the instruments technological evolution and the basic concepts of retrieval theory. We include a review of algorithms developed for ozone, nitrogen dioxide, sulfur dioxide, formaldehyde, bromine monoxide, water vapor and glyoxal, a selection of studies using these algorithms, the challenges they face and how these challenges can be addressed. The paper ends by providing insights on the opportunities that new instruments will bring to the atmospheric chemistry, weather and air quality communities and how to address the pressing need for long-term, inter-calibrated data records necessary to monitor the response of the atmosphere to rapidly changing ecosystems.

Keywords: Atmosphere, Air Quality, Remote Sensing, Satellite, UV-VIS

1. Introduction

Since 1959 there have been 209 space missions devoted to the observation of the Earth's atmosphere (Earth Observation Portal). The sensors used in these missions can be classified into two categories depending on the origin of the measured radiation. Passive instruments detect radiation generated by the Sun, the Earth and its atmosphere while active instruments use radiation generated artificially. A second classification depends on the observation geometry employed by the instrument. Nadir instruments point directly at the Earth's surface while limb instruments point at the edge of the atmosphere and take measurements at different tangent heights. Occultation instruments like ACE-FTS (Bernath et al., 2005) use a limb geometry to point directly at the Sun or other stars.

Nadir observations probing the atmospheric column are sensitive to the boundary layer when using light at UV-VIS wavelengths. Limb geometries have difficulties sampling the lower layers of the atmosphere but they can provide profile information at vertical resolution unavailable in the nadir geometry. Solar occultation instruments add excellent SNRs to the vertical profiling capability. This diversity of instruments and geometries provides information about

a wide range of geophysical variables including temperature, pressure, winds,
20 trace gas concentrations, aerosols and clouds.

The launch of the BUV (Krueger et al., 1973) and TOMS (Heath et al., 1975) instruments in the 1970s marked the beginning of a new era for the study of the global distribution of atmospheric ozone (O_3). Since those early days, steady progress in instrument capabilities (e.g., increased SNR, spectral coverage and
25 spatial resolution) and algorithm development have extended the sensitivity of these instruments from the stratosphere and upper troposphere to the lower atmosphere. In 1995, ESA launched the ERS-2 satellite carrying GOME (ESA, 1995; Burrows et al., 1999), now known as GOME-1, as part of its payload. GOME-1 UV-VIS sensors provided valuable data for studying not only the
30 stratospheric O_3 layer, but also tropospheric chemistry and pollution on a global scale.

Today, UV-VIS observations from space provide significant insights into air quality and atmospheric chemistry. Satellite global observations are essential contributions to global observing systems (Barrie, 2006). For example, the
35 oxidation capacity of the troposphere is directly linked to O_3 concentration (Lelieveld and Dentener, 2000). The tropospheric O_3 concentration depends on natural (e.g., transport of stratospheric O_3 to the troposphere and photochemical production derived from biogenic precursors) and anthropogenic factors (e.g.,
40 photochemical production derived from precursors generated by human activities) (Fishman et al., 2008) that can be detected using satellite sensors (e.g., Liu et al., 2010). Moreover, O_3 photochemical production can be constrained globally using satellite observations (Zhang et al., 2008). The combination of nitrogen dioxide (NO_2), sulfur dioxide (SO_2), formaldehyde (H_2CO) and glyoxal
45 ($C_2H_2O_2$) observations can constrain the chemical regime of O_3 production and help determine the impact of human activities, informing air quality manager decisions (Duncan et al., 2014). Furthermore, satellites can also contribute to the understanding of the role of halogen chemistry in tropospheric chemistry and stratospheric O_3 (Simpson et al., 2015). Global satellite retrievals of bromine monoxide (BrO), iodine monoxide (IO) and chlorine dioxide ($OCIO$) are helping

50 researchers understand the effects of halogens in remote areas on a global scale.

A series of publications in the latter part of the first decade of the 2000s summarized the state of the field at that time and provided insights of the challenges laying ahead (Chance, 2006; Fishman et al., 2008; Martin, 2008; Burrows et al., 2011). One decade later, steady progress has resulted in a new generation 55 of instruments with enhanced capabilities. Some of these instruments are already orbiting the Earth, others like the constellation of geostationary air quality instruments, are planned to be launched in the near future. Besides instrument development, the last decade has seen significant progress on retrieval algorithms, exploitation of satellite data in scientific studies (e.g., inversions and data assimilation) and validation of satellite measurements using in-situ 60 and remote sensing fiducial measurements.

This paper aims to provide a review of historic, present and future nadir viewing instruments measuring solar UV-VIS backscattered radiation and examine how these missions have contributed to the understanding of reactive atmospheric trace gases and the complexity of air quality modelling. We include sections on O₃, NO₂, SO₂, H₂CO, BrO, H₂O and C₂H₂O₂, providing a comprehensive list of the retrievals produced for each molecule and some of their more significant applications. Discussions on aerosol retrievals derived from space-based UV-VIS instruments are beyond the selected scope of this paper despite 70 being a relevant component of air quality observing systems. Likewise, carbon monoxide is excluded as it is observed using infrared radiation.

Section 2 provides a historic review describing the evolution of instruments and technological advancements that have resulted in current observational capabilities. Section 3 focuses on the techniques used to exploit UV-VIS observations and retrieve trace gas concentrations. Section 4 summarizes UV-VIS space observations of O₃, NO₂, SO₂, H₂CO, BrO, H₂O, and C₂H₂O₂ including 75 scientific studies, applications, limitations and challenges of these datasets. Section 5 presents our conclusions and a series of recommendations for the future. Table 1 provides the definition of most acronyms and abbreviations used in the 80 text.

Table 1: List of acronyms

ACE-FTS	Atmospheric Chemistry Experiment-Fourier Transform Spectrometer
AERONET	AErosol RObotic NETwork
ADEOS	Advanced Earth Observing Satellite
AMSRE	Advanced Microwave Scanning Radiometer for EOS
ARM	Atmospheric Radiation Measurement
BUV	Backscatter UltraViolet
CCD	Charge Coupled Device
CMA	China Meteorological Administration
CNSA	China National Space Agency
COSMIC	Constellation Observing System for Meteorology, Ionosphere and Climate
CTM	Chemical Transport Model
DSCOVR	Deep Space Climate Observatory
ECV	Essential Climate Variable
EMI	Environmental Monitoring Instrument
EnviSat	Environmental Satellite
EPIC	Earth Polychromatic Imaging Camera
EOS	Earth Observing System
ERS-2	European Remote Sensing-2
ESA	European Space Agency
EUMETSAT	European Organisation for the Exploitation of Meteorological Satellites
FWHM	Full Width at Half Maximum
GCOS	Global Climate Observing System
GEMS	Geostationary Environment Monitoring Spectrometer
GEO	Geosynchronous Equatorial Orbit
GEOS-Chem	Goddard Earth Observing System-Chemistry

GEWEX	Global Energy and Water cycle EXchanges
GF-5	Gao Fen-5
GNSS	Global Navigation Satellite System
GOME(-1)	(first) Global Ozone Monitoring Experiment
GOME-2	Global Ozone Monitoring Experiment-2
GPS	Global Positioning System
GRUAN	GCOS Reference Upper-Air Network
LEO	Low Earth Orbit
MEaSURES	Making Earth System Data Records for Use in Research Environments
NASA	National Aeronautics and Space Administration
NCAR	National Center for Atmospheric Research
NIVR	Nederlands Instituut voor Vliegtuigontwikkeling en Ruimtevaart
NMVOC	Non Methane Volatile Organic Compound
NOAA	National Oceanic and Atmospheric Administration
OCO-2	Orbiting Carbon Observatory-2
OMI	Ozone Monitoring Instrument
OMPS	Ozone Mapping and Profiler Suite
OMPS-NM	OMPS-Nadir Mapper
OMPS-NP	OMPS-Nadir Profiler
OSIRIS	Optical Spectrograph and InfraRed Imager System
PDA	PhotoDiode Array
PMT	PhotoMultiplier Tube
QA4ECV	Quality Assurance for Essential Climate Variables
RTM	Radiative Transfer Model
SBUS	Solar Backscatter Ultraviolet Sounder
SBUV	Solar Backscatter UltraViolet
SCIAMACHY	SCanning Imaging Absorption SpectroMeter for Atmospheric CHartographY

S-NPP	Suomi National Polar-orbiting Partnership
SNR	Signal to Noise Ratio
SSMI	Special Sensor Microwave Imager
SSMIS	Special Sensor Microwave Imager/Sounder
S5	Sentinel 5
S5P	Sentinel 5 Precursor
SZA	Solar Zenith Angle
TEMPO	Tropospheric Emissions: Monitorig of Pollution
TOMS	Total Ozone Monitoring Spectrometer
TOMS-EP	TOMS-Earth Probe
TOU	Total Ozone Unit
TROPOMI	TROPOspheric Monitoring Instrument
UV	UltraViolet
VIS	VISible
VOC	Volatile Organic Compound
VLIDORT	Vector Linearized Discrete Ordinate Radiative Transfer

2. Past, present and future space-borne UV-VIS instruments

Early efforts to analyze atmospheric composition using remote sensing date back to the nineteenth century. Samuel P. Langley invented the bolometer (Langley, 1881) to obtain precise measurements of the infrared through the near UV
 85 Sun radiation in order to determine the mean value of the solar constant and its variations. To fully exploit the capabilities of the new instrument, Langley and Abbot developed substantial new experimental techniques (such as an early chart recorder) and various analysis techniques (e.g., the "Langley plot", introducing the air mass factor concept), including photographic techniques for
 90 high pass filtering to produce line spectra from "bolographs", foreshadowing the high pass filtering used today by researchers employing the Differential Optical Absorption Spectroscopy (DOAS) technique for analyzing atmospheric spectra

(Langley and Abbot, 1900).

Fabry and Buisson (1913, 1921) not only studied the coefficients of O₃ absorption they also conducted the first measurements of atmospheric O₃ by analyzing its absorption signatures at different wavelengths in direct sunlight observations using photographic spectographs. Gordon Dobson designed in 1927 a photoelectric spectrometer with the objective of measuring total atmospheric O₃ (Dobson, 1931) using direct observations of the Sun. The Dobson spectrometer measures solar radiation at two suitable wavelengths (305 nm and 325 nm) to work out their ratio in order to calculate the amount of O₃. Using the same type of instrument the vertical distribution of O₃ can be estimated. The "Umkehr" method, proposed by Götz et al. (1934), relies on pointing the spectrometer towards zenith to measure the intensity of scattered radiation at different altitudes. Making measurements at two different wavelengths for a set of solar zenith angles it is possible to deduce the vertical distribution of O₃. These pioneering works share similar concepts with modern ground-based and space-borne instruments. Despite decades of technological advances and theoretical studies the basic physical principles behind these works are similar to the ones supporting current ground-based and space-borne instruments.

The first space-based measurements of atmospheric O₃ using UV radiance were obtained with instruments designed to study the ionosphere and the mesosphere at wavelengths shorter than 300 nm (Krasnopol'skii, 1966; Rawcliffe and Elliott, 1966; Lozenas, 1968). Due to Rayleigh scattering and strong O₃ absorption, the penetration of photons below 300 nm is limited to the highest layers of the troposphere.

The BUV instrument on-board Nimbus-4 initiated the era of satellite instruments specifically designed to study atmospheric composition using UV backscatter solar radiance in 1970. By including spectral measurements up to 340 nm, this instrument was suitable for observations of total column O₃ with enhanced stratospheric and tropospheric sensitivity (Heath and Mateer, 1973). Over the next three decades, follow up instruments SBUV (Frederick et al., 1986; Fleig et al., 1990), SBUV/2 (DeLand and Cebula, 1998) and TOMS

(Heath et al., 1975) extended and consolidated the lessons learned from BUV
 125 and improved its spatial and spectral resolution. BUV and SBUV instruments measured twelve 1 nm wide bands ranging from 255 nm to 340 nm at direct nadir only. TOMS only measured six 1 nm bands from 312 nm to 380 nm. However, it was equipped with a cross-track scanning capability that allowed daily global observations at a resolution of $50 \times 50 \text{ km}^2$ for the first time. These
 130 early instruments used a single PMT detector, preserving the accuracy of radiometric measurements across different wavelength bands. SBUV sensors were also capable of measuring in continuous scan mode, recording spectra from 160 nm to 400 nm at 1 nm FWHM resolution and 0.14 nm sampling, with reduced temporal and spatial resolution.

The SBUV continuous mode was improved with GOME-1 (ESA, 1995),
 135 launched in 1995 on-board ESA's ERS-2 satellite, initiating the era of hyperspectral UV-VIS spectrometers. The GOME-1 innovative design consisted of a double monochromator combining a predisperser prism and four grating spectrometers with linear PDAs, allowing the measurement of continuous spectra
 140 from 240 nm to 790 nm at resolutions of 0.22 nm to 0.40 nm. GOME-1 standard operation mode provided a spatial footprint of $40 \times 320 \text{ km}^2$. This footprint combined with the scanning mechanism provided global coverage in three days. The spectral capabilities of GOME-1 were suitable for the development of retrievals beyond O₃ and SO₂ and started the era of air quality characterization
 145 from space. Exploiting the hyperspectral capabilities of the instrument, new retrievals of tropospheric O₃, NO₂, H₂CO, C₂H₂O₂, BrO, and H₂O were developed. GOME-1 was proposed as a precursor of the SCIAMACHY (Bovensmann et al., 1999) instrument launched in 2002 as part of ESA's EnviSat payload.
 SCIAMACHY had three operating modes: limb, occultation and nadir. In
 150 the nadir mode, SCIAMACHY provided higher spatial resolution and extended spectral coverage compared with GOME-1 to measure CH₄, CO and CO₂ using short-wave infrared.

The next ground breaking technological advancement happened in 2004 with the launch of OMI. The linear PDA detectors of the GOME-1 and SCIAMACHY

155 instruments were replaced by 2-dimensional CCD detectors (Leveld et al., 2006) following the success of the OSIRIS limb instrument (Llewellyn et al., 2004). This new design revolutionized monitoring of air quality from space. It allowed finer spatial resolution measurements while keeping spectral performance and eliminating the need for a scanning mechanism. This new concept, when used 160 in LEO satellites, allows for wide swaths, with daily global coverage and high spatial resolution. Besides the technological innovation in the detectors, the remarkable stability of OMI's performance (Leveld et al., 2018) and its enhanced spatial resolution has allowed for the first time the detection and quantification of point emitters (Fioletov et al., 2016), the characterization of urban scale 165 chemical processes and to study the decadal evolution of air quality (Duncan et al., 2014). The GOME-1 and OMI instruments were followed by GOME-2 (Munro et al., 2016), OMPS-NM (Seftor et al., 2014), OMPS-NP (Pan et al., 2017) and TROPOMI (Veefkind et al., 2012) instruments supported by ESA, EUMETSAT, NASA and NOAA. In recent years, China has developed its own 170 air quality program relying on the SBUS (Huang et al., 2012), TOU (Wang et al., 2012) and EMI (Zhang et al., 2018) instruments supported by the CMA and the CNSA. A comprehensive list of past and current instruments is provided in table 2 including information about their fundamental characteristics.

The instruments described in table 2 are payloads on spacecrafts in Sun- 175 synchronous polar LEOs, measuring the sunlit part of the globe in the morning (9:00-11:00 local time (LT)) or early afternoon (12:00-14:30 LT). Among all past and currently operating satellite instruments, TROPOMI offers the highest spatial resolution ($3.5 \times 7 \text{ km}^2$) while OMI offers the longest record, and least instrument degradation (Schenkeveld et al., 2017). The only exception to LEO 180 orbit instruments in table 2 is EPIC (Marshak et al., 2018). The DSCOVR spacecraft, with EPIC as payload, was launched on February 2015 reaching its first Lagrange point orbit on June 2015. From this orbit, EPIC scans Earth's sunlit full-disk with high spatial (18 km^2 at nadir) and temporal (almost hourly) resolutions. EPIC's ten spectral channels allow the retrieval of total column O₃ 185 and volcanic SO₂.

To increase the number of observations over a particular location on a day, a new generation of space air quality instruments, to be deployed on GEO satellites, are being developed, building on the heritage of spectrometers flown in LEO. Three instruments are planned to be launched in the near future:

190 Korea's Aerospace Research Institute GEMS (Kim et al., 2018) instrument will observe East Asia, NASA's TEMPO (Zoogman et al., 2017) will observe North America and ESA's Sentinel 4 (and planned follow up missions) (Ingmann et al., 2012) will observe Europe. These instruments will provide hourly measurements during the sunlit hours at unprecedented spatial resolutions as small as $\sim 2.5 \times 4.5 \text{ km}^2$. To maximize the information obtained by these GEO instruments, given their expected geographical coverage, it is of paramount importance to combine them with LEO observations provided by GOME-2, TROPOMI and OMPS-NM instruments to produce inter-calibrated products. These products will allow near-real time monitoring of air quality and facilitate scientific studies

195 at new spatial and temporal scales.

200

Along with the constellation of GEO instruments, air quality observations from LEO will continue in the next decades. The launch of Sentinel 5 (and follow up missions) starting in 2021 by ESA will provide morning observations while the afternoon overpass will be provided by OMPS-NM and OMPS-NP instruments to be launched by NOAA in several missions extending into the

205 2030s.

It is worth mentioning new initiatives in their early stages such us TROPO-LITE, aiming to achieve a lighter version of TROPOMI (Maresi et al., 2014) with enhanced spatial resolution ($1 \times 1 \text{ km}^2$), the Russian Ozonometer (Dobrolenskiy et al., 2015, 2018), the PanFTS instrument using Fourier Transform interferometry (Wu et al., 2011; Sander et al., 2015) and innovative designs using Fabry-Pérot interferometry (Kuhn et al., 2019).

Table 2: Past and current nadir instruments using solar backscatter radiation for monitoring of atmospheric composition from LEO.

Instrument (Agency)	Satellite(s)	Operation period	ECT	Global coverage	Detector	Nominal pixel resolution [km ²]	Spectral range [nm]	Spectral resolution [nm]
BUV (NASA)	Nimbus-4	1970–1980	12:00 ^a	10 days	PMT	220	255.65 273.61 283.10 287.70 292.29 297.59 301.97 305.87 312.56 317.56 331.26 339.89	1
SBUV (NASA)	Nimbus-7	1979–1994	12:00 ^a	14 days	PMT	200	As BUV	1
SBUV continuous mode (NASA)	Nimbus-7	1979–1987	12:00 ^a	N/A ^d	PMT	200	160–400	1
TOMS (NASA)	Nimbus-7/Meteor-3 TOMS-EP/ADEOS	1979–2006	12:00 ^b N/A 10:30 ^c 12:00 ^b	1 day	PMT	50 (nadir)	312.5 317.5 331.3 339.9 360.0 380.0	1
SBUV/2 (NOAA)	NOAA-9,11, 14,16,17,18,19)	1984 ^g	12:00 ^{a,c}	10 days	PMT	170	As BUV	1.1
GOME-1 (ESA)	ERS-2	1995–2011	10:30 ^a	3 days	Linear PDA	40×320 ^f 40×960 ^f	240–790	0.22–0.40
SCIAMACHY nadir mode (ESA)	EnviSat	2002–2012	10:00 ^a	6 days	Linear PDA	30×60 ^e 30×120 ^f	240–1750; 1934–2044 2259–2386	0.22–1.48
OMI (NASA/ESA/NIVR)	Aura	2004 ^g	13:45 ^b	1 day	2D CCD	13×24 (nadir)	270–500	0.42–0.63
GOME-2 (ESA/EUMETSAT)	Metop-(A/B/C)	2006 ^g	9:30 ^a	1.5 days	Linear PDA	40×80 ^e 40×160 ^f	240–790	0.24–0.53
SBUS (CMA)	FY-3(A/B/C)	2008 ^g	9:05 ^a 13.38 ^b 10.15 ^a	7 days	PMT	200	252.00 273.62 283.10 287.70 292.29 297.59 301.97 305.87 312.57 317.56 331.26 339.89	1
TOU (CMA)	FY-3(A/B/C)	2008 ^g	9:05 ^a 13.38 ^b 10.15 ^a	1 day	PMT	50 (nadir)	308.73 312.64 317.65 322.46 331.38 360.25	1
OMPS-NM (NASA/NOAA)	S-NPP NOAA-20	2011 ^g	13.35 ^b	1 day	2D CCD	50 (nadir) 17 (nadir)	300–380 297–420	1
OMPS-NP (NASA/NOAA)	S-NPP NOAA-20	2011 ^g	13.35 ^b	12 days	2D CCD	250	250–310	1
EPIC (NASA/NOAA)	DSCOVR	2015 ^g	N/A	1 day	2D CCD	8 (nadir)	317.5, 325.0, 340.0, 388.0 443.0, 551.0, 680.0, 687.75 764.0, 779.5	0.84–3.0
TROPOMI (ESA)	S5P	2017 ^g	13.30 ^b	1 day	2D CCD	3.5×7 (nadir)	270–775 2305–2385	0.5–1 0.25
EMI (CNSA)	GF-5	2018 ^g	13.30 ^b	1 day	2D CCD	13×48 (nadir)	240–710	0.3–0.5

^a Descending node ^b Ascending node ^c Orbit drift after 1–2 years (McPeters et al., 2013) ^d SBUV only operated in this mode 1 day per month^e Forward scan ^f Backward scan ^g Still operational

3. Retrieval methods

After the incoming solar radiation enters the Earth's atmosphere, part of the radiation is absorbed by atmospheric trace gases and particles, part of the radiation is backscattered by air molecules, aerosols and clouds, and part of the radiation is reflected by Earth's surface. The top panel of Figure 1 shows solar irradiance and Earth radiance measurements made by the GOME-1 instrument. The bottom panel, shows reflectance spectra derived for four different scenes. The distinct surface reflectance characteristics of clouds, oceans, deserts and

vegetation determine the overall shape of the spectra. The interaction between light and trace gases absorption (e.g., shown in Figure 2 top panel) leads to spectral signatures in the backscattered radiances as the ones shown in Figure 1 bottom panel.

At wavelengths below 340 nm, atmospheric absorption is dominated by O₃ in the Hartely and Huggins bands. The mean photon path length, shown in Figure 2 middle left panels, indicates that at shorter wavelengths (e.g., 250 nm), photons can only penetrate to \sim 40 km due to the strong O₃ absorption and Rayleigh scattering. With increasing wavelengths, O₃ absorption decreases by almost four orders of magnitude (from \sim 2 down to 10^{-4}) and Rayleigh scattering decreases proportionally to the fourth power of wavelength. In consequence more photons can penetrate deeper into the atmosphere. In the Huggins bands, a significant portion of photons can penetrate into the troposphere.

The wavelength-dependent O₃ absorption and Rayleigh scattering primarily provide information about the vertical distribution of the O₃ profile. The temperature dependent O₃ absorption in the Huggins bands further enhances sensitivity to tropospheric O₃ (Chance and Spurr, 1997). Similarly at longer wavelengths, the wide range of H₂O absorption might provide information about the H₂O profile. The wide range of O₂ absorption in the O₂-A band, and the noticeable O₂-O₂ absorption and their known concentrations can be used to derive aerosol and cloud vertical information. For most of the other trace gases, the absorption optical depth is typically on the order of 10^{-3} or smaller. Given their small optical depths, and the weak pressure and temperature dependence of their absorption features satellite measurements are mostly sensitive to their integrated vertical abundance.

The retrieval of trace gas concentrations from radiance measurements can be described as the inversion of equation 1. The goal is to estimate the values of a set of variables **x** (e.g., trace gas concentrations at different atmospheric levels, surface reflectance) given their relationship with a set of observations **y** (e.g., radiances at different wavelengths). The relationship between **x** and **y** is described by a forward model (i.e., a radiative transfer model, RTM) **F**

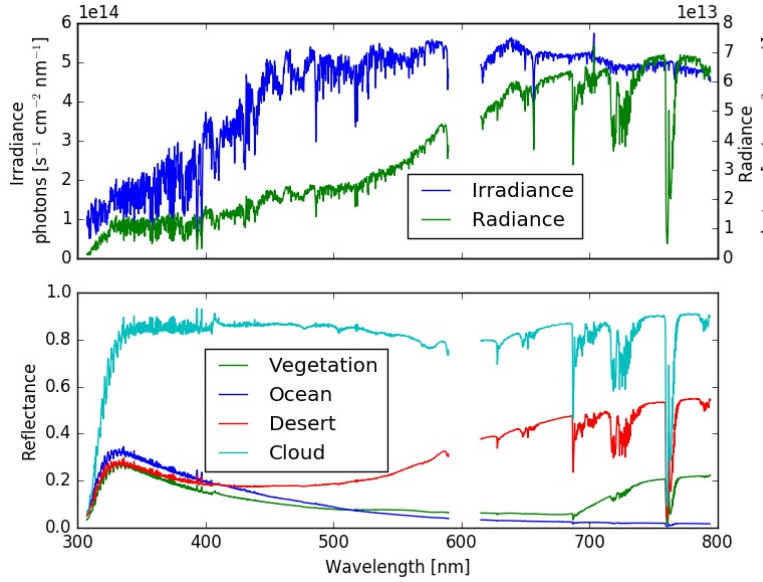


Figure 1: Upper panel shows two typical GOME-1 irradiance and radiance measurements. Lower panel shows the reflectance $[(\pi \times \text{radiance}) / (\cos(\text{SZA}) \times \text{irradiance})]$ derived from GOME-1 measurements for different scenes in the UV-VIS.

depending on the state vector (retrieved) and a vector of model parameters \mathbf{p} (not retrieved). Errors are expressed in equation 1 as ϵ .

$$\mathbf{y} = \mathbf{F}(\mathbf{x}, \mathbf{p}) + \epsilon \quad (1)$$

Due to limitations in forward models and instrumentation as well as observation errors, ϵ is never 0. For that reason the process of inverting equation 1 can only lead to a statistical estimate of \mathbf{x} , usually combining a-priori and observational information.

Below we briefly discuss the most common strategies employed to deal with the inversion problem and refer the reader to Rodgers (2000) for a detailed description of retrieval techniques. We also provide a brief description of the algorithm physics needed to support modern retrieval techniques.

3.1. Optimal estimation

Optimal estimation (OE)(Rodgers, 2000) has become the standard for O₃ profile retrievals in the UV-VIS. In the OE scheme the state vector \mathbf{x} includes the O₃ profile, geophysical parameters (e.g., other trace gases, surface reflectance and cloud parameters) and other spectroscopic fit parameters (e.g., stray light, Ring effect patterns, and bandpass shape and spectral scale prescriptions). The measurement vector \mathbf{y} is either the radiance or the ratio of the radiance to the irradiance, depending on the detailed approach.

The linearization of the forward model can be described as $\mathbf{x} = \mathbf{x}_a + \mathbf{K}^{-1}(\mathbf{y} - \mathbf{F}(\mathbf{x}_a))$ where $K_{i,j} = \partial F_i(\mathbf{x}) / \partial x_j$ is the Jacobian or weighting function matrix with retrieved (\mathbf{x}) and a priori (\mathbf{x}_a) vectors respectively. Given the information content of the satellite observations this is often an ill-posed inversion problem. OE employs additional constraints so that a-priori information complements measurement constraint information. OE simultaneously minimizes the difference between measured and simulated radiances and the difference between retrieved and a priori states with relative weights determined by the Jacobian and the a priori and measurement covariance matrices. Because of non-linearity, the minimization of the cost function χ^2 (equation 2) is iterated updating \mathbf{x} to an a-posteriori solution (3) with \mathbf{K}_i calculated for the latest completed iteration.

$$\chi^2 = \left\| \mathbf{S}_{\mathbf{y}}^{-\frac{1}{2}} \{ \mathbf{K}_i (\mathbf{X}_{i+1} - \mathbf{X}_i) - [\mathbf{Y} - \mathbf{F}(\mathbf{X}_i)] \} \right\|_2^2 + \left\| \mathbf{S}_{\mathbf{a}}^{-\frac{1}{2}} (\mathbf{X}_{i+1} - \mathbf{X}_a) \right\|_2^2 \quad (2)$$

$$\mathbf{X}_{i+1} = \mathbf{X}_i + (\mathbf{K}_i^T \mathbf{S}_{\mathbf{y}}^{-1} \mathbf{K}_i + \mathbf{S}_{\mathbf{a}}^{-1})^{-1} [\mathbf{K}_i^T \mathbf{S}_{\mathbf{y}}^{-1} (\mathbf{Y} - \mathbf{F}(\mathbf{X}_i)) - \mathbf{S}_{\mathbf{a}}^{-1} (\mathbf{X}_i - \mathbf{X}_{\mathbf{a}})] \quad (3)$$

where \mathbf{X}_i , \mathbf{X}_{i+1} , \mathbf{X}_a are previous, current and a-priori state vectors, \mathbf{Y} , \mathbf{F} are measured and simulated radiance vectors, \mathbf{K} is the weighting function matrix and $\mathbf{S}_{\mathbf{a}}$, $\mathbf{S}_{\mathbf{y}}$ the a-priori and measurement covariance matrices.

²⁸⁵ *3.2. Discrete channel ozone retrievals*

The Version 8 Total Column Ozone Algorithm (V8Toz) (Wellmeyer et al., 2004) is one of the newer versions of a long line of NASA algorithms designed to make efficient use of the sensitivity of the 317.5 vacuum nm channel to the total O₃ column and of the 331.3 vacuum nm channel to the surface and cloud reflectivity assuming that O₃ is the only absorber present in the Rayleigh atmosphere.

The algorithm uses RTM lookup tables (LUTs) to determine the geometric cloud fraction and effective reflectivity to explain the log₁₀ (radiance/irradiance measurement ratio) called N-Value for the 331.3 nm channel. The LUT are dimensioned for total O₃ amounts populated with the radiative transfer results at 50 DU intervals for low, medium and high latitudes standard profiles. The table values, interpolated to geometric cloud fraction and viewing geometry are used to determine the total O₃ amount that explains the 317.5 nm N-Value measurement. The results from this first step are further refined using a set of climatological profiles (McPeters et al., 2007) including information for each month at 10° latitude bands and temperature fields. A set of final empirical adjustments specific to atmospheric conditions is finally applied to the total O₃ value including the presence of UV-absorbing aerosols and profile shape sensitivity of the 313 nm channel at high optical path lengths.

The RTM LUTs contain information to provide measurement estimates for additional channels. The shorter wavelengths can be used to provide estimates of elevated atmospheric SO₂ amounts (Yang et al., 2007). The total O₃ values derived in the second step are used to compute measurement residuals as relative differences between the measurements and the values for these additional channels.

The Version 8 Ozone Profile Retrieval Algorithm (V8Pro) (Bhartia et al., 2013) was developed to create an O₃ profile climate data record using the 12 channel measurements of the SBUV(/2) instruments (Frith et al., 2014) but is also used in the operational near-real-time SBUV/2 and OMPS retrievals at NOAA. As shown in Figure 2, with increasing wavelength from 250 nm to 320

nm, the O₃ absorption decreases and the photons penetrate more deeply into the atmosphere sampling different altitude regions. The wavelengths used in V8Pro were selected to give good coverage of the range of O₃ absorption cross sections present in the Hartley-Huggins bands with the absorption approximately 320 doubling between adjacent wavelengths.

In this retrieval, \mathbf{Y} is defined as the ten radiance/irradiance ratios (at [253, 273, 283, 288, 292, 298, 302, 306, 313, 318] nm) and \mathbf{X} is a vector of 3 km layer O₃ amounts. The maximum likelihood retrieval is formulated using logarithms of \mathbf{Y} as they show reduced nonlinear responses to O₃ profile changes. 325 The measurement covariance matrix (\mathbf{S}_y) is a diagonal matrix of the relative noise for each channel. The a-priori profile set and its covariance are derived from McPeters et al. (2007) climatology. Cloud and reflectivity information are obtained from the V8Toz algorithm described above. As explained in the OE section, the solution to this linearized approximation to the forward model is 330 achieved using an iterative approach until the convergence criteria are meet.

3.3. Two step retrievals

Photon penetration above 330 nm (Figure 2) varies weakly with increasing wavelengths limiting the information content of the hyperspectral satellite measurements. In this case, direct fitting is a suitable technique for the retrieval of 335 slant column densities (SCDs) along the line of sight. A second step in these kind of retrievals implies the conversion of SCDs into vertical column densities (VCDs) using a-priori information and RTMs to calculate effective air mass factors (AMFs). This is the preferred approach to retrieve NO₂, SO₂, H₂CO, BrO, C₂H₂O₂ and H₂O VCDs.

The basis of this retrieval technique is to fit the high-pass filtered ratio of 340 the Earth radiance and the solar irradiance, if the DOAS equation is to be used (Platt, 2006), the ratio of the radiance to the irradiance or simply directly fitting the radiance as described by Chance (1998) to laboratory-measured absorption cross-sections ($\tau(\lambda)$) of the target species and other interfering gases, a reference 345 Ring spectrum ($R(\lambda)$) (Chance and Spurr, 1997) and scaling and baseline

polynomial functions (P_{sc} and P_{bl} respectively). The polynomials model the spectrally varying scattering effect of clouds and aerosols and reflection by the Earth's surface. Equation 4 shows the model used in the case of direct fitting.

$$F(\lambda) = [I_0(\lambda) \exp(-\tau(\lambda)) + R(\lambda)] P_{sc}(\lambda) + P_{bl}(\lambda) \quad (4)$$

The source spectrum (I_0) is usually derived from direct solar observations.
 350 However to mitigate instrument calibration errors other methods have been developed using solar monthly means (Chan Miller et al., 2014) or radiance means over reference sectors where low concentrations of the target molecule are expected (González Abad et al., 2015; De Smedt et al., 2018). Li et al. (2013) employed instead the principal components of the radiances in regions with low
 355 concentrations of SO_2 to capture the radiance variability caused by physical processes and measurement artifacts. By fitting these principal components and SO_2 Jacobians calculated with a RTM, they retrieve directly SO_2 VCDs.

The second step involves the calculation of AMFs. For optically thin absorbers, AMFs can be calculated by decoupling the radiative transfer calculation of vertically resolved sensitivities ($W(z)$) and a-priori vertical profile shapes ($S(z)$) (Palmer et al., 2001) as shown in equation 5.

$$AMF = \int_0^{\infty} W(z)S(z)dz \quad (5)$$

The $W(z)$, known as scattering weight, represents the number of times the radiation reaching the satellite has traversed an atmospheric layer ($z, z+dz$) (middle left panels of Figure 2) while the $S(z)$, known as shape factor, is the
 365 normalized trace gas profile (middle right panels of Figure 2).

Figure 2 shows that between 300 nm and 500 nm the photon penetration varies slowly with wavelength, particularly for altitudes above 2 km. It is therefore a fair approximation to compute AMFs using a single wavelength representative of the vertical sensitivities across the fitting window. Below 2 km the
 370 photon penetration at those wavelengths is greatly reduced limiting the sensitivity of satellite measurements to the boundary layer. Retrievals of SO_2 , H_2CO ,

and BrO carried out in the UV spectral range (between ~ 320 nm and 360 nm) are particularly affected by the reduction of sensitivity to the boundary layer.

Usually the scattering weights, computed with a RTM, are parameterized by observational angles, terrain/cloud pressure, and terrain/cloud reflectivity at the instrument's field-of-view (FOV) and stored in a LUT. The effect of clouds is modeled by using the cloud radiance fraction and the cloud pressure. Due to sparseness of observations and large spatial and temporal variabilities, information of a-priori profiles is obtained from CTMs. Differences in the spatial and temporal resolution between the CTM and the satellite observations, the ability of CTMs to simulate the vertical distribution of the absorbing species, the geometry-dependent surface reflectance properties and the presence of aerosols and clouds are the most significant sources of error in AMF calculations (Lorente et al., 2017). It is worth mentioning that despite being a significant source of error, aerosols are not considered explicitly in most retrievals given the difficulty to disentangle the effect of scattering by clouds and aerosols. The lower panel of Figure 2 shows vertically resolved AMFs of NO₂, SO₂, H₂CO, BrO, C₂H₂O₂ and H₂O computed using photon paths and shape factors shown in Figure 2 middle panels.

390 3.4. Algorithm physics

The challenges met in algorithm physics development allow fitting to very close to the noise levels of the atmospheric spectra, often to several times 10^{-4} of the measured radiance (cf., Saiz-Lopez et al., 2007). Reaching this level of fitting precision requires reference data, including absorption spectra, which cumulatively contribute less than this amount to the fitting uncertainties.

Solar reference spectrum. An accurate solar reference spectrum is required to support in-orbit wavelength calibration (Chance, 1998), Ring effect determination (Chance and Spurr, 1997), determination of the instrument transfer function from flight data (Chance, 1998) and correction for spectral undersampling (Chance, 1998; Chance et al., 2005). There are low-resolution extraterrestrial

solar spectra that are very accurate in absolute intensity calibration (Thuillier et al., 2003). These have been combined with a ground-based FTS spectrum from Kurucz et al. (1984) at the National Solar Observatory, supplemented at wavelengths <305 nm by balloon-based spectra from Hall and Anderson to produce a high-resolution spectrum with accurate intensity calibration Chance and Kurucz (2010).

Rayleigh scattering and the Ring effect. Rayleigh scattering is often the predominant contributor to back scattered light measured in the nadir, particularly for wavelengths shorter than 500 nm. Highly accurate parameterizations of the wavelength dependences of the cross sections and scattering phase functions for Rayleigh scattering by air are available (Bates, 1984; Chance and Spurr, 1997; Bodhaine et al., 1999), with Bodhaine et al. (1999) being the current preference.

Grainger and Ring (1962) first noticed that solar Fraunhofer lines became broadened and reduced in depth depending on the SZA when viewed from the ground in scattered sunlight. This is now known to be the effect of inelastic scattering by the fraction of the Rayleigh scattering by air that is inelastic, i.e., Raman scattering. The Raman scattering, about 97% rotational Raman and the rest vibrational Raman, constitutes 4% of the Rayleigh scattering in the wavelengths considered here. Ring effect corrections are performed using the molecular physics of the Raman scattering (Chance and Spurr, 1997) coupled with the solar reference spectrum (Chance and Kurucz, 2010), and in some cases coupled with radiative transfer calculations (Joiner et al., 1995; Vountas et al., 1998) to the level that negligible uncertainties remain in the spectral fitting from this source of spectral structure (cf. Chance, 1998).

Vibrational Raman scattering in ocean water can be readily measured in these wavelengths (it must be corrected for in the spectral analysis for some gases) and it is suggested that it may be used to estimate chlorophyll and dissolved organic matter contents of ocean water (Vasilkov et al., 2002).

Wavelength issues. Shifts from ground-based wavelength calibration can be seen on orbit due to launch stresses or the different thermal environment. It can also

vary by substantial amounts, compared to the spectral fitting needs, due to thermal and other in-flight perturbations and instrumental effects (e.g., orbital or seasonal thermal changes, partial filling of the field-of-view). Additionally, solar irradiances are obtained at substantially different Doppler shifts (up to
 435 0.01 nm at 400 nm) from Earth-view radiance measurements.

For these reasons, Caspar and Chance (1997) showed that wavelength calibration is improved by using a Fraunhofer reference spectrum, (revised in Chance and Kurucz, 2010), and applying either spectral cross-correlation (Kurtz et al., 1992) or nonlinear least-squares (NLLS) fitting to adjust window portions
 440 of radiances or irradiances. These methods can usually calibrate in vacuum wavelength to 0.01 detector pixel spacing or better (cf. Chance, 1998). The NLLS method has been implemented in operational algorithms for GOME, SCIAMACHY, OMI and OMPS.

Instrument function and sampling issues. Slit functions (instrument transfer
 445 functions, ITFs) may differ in flight from those determined in ground calibration. It is often useful to re-determine them in flight, combining this with the wavelength calibration using NLLS.

Nyquist sampling of a spectrum requires sampling to at least twice the highest spatial (i.e., wavelength) frequency admitted by the resolution limit of the
 450 instrument (the band limit, Goldman, 1953). Spectral undersampling occurs when spectral measurements are not made at fine enough spacing to Nyquist sample the ITF (Chance et al., 2005) and thus provide full knowledge of the spectrum up to the band limit. Undersampling can be a major source of fitting error in the current generation of satellite-borne spectrometers, particularly as
 455 they mostly do not take enough spectral samples relative to their spectral resolution and, as the solar irradiance spectra must be resampled in wavelength in order to be compared to radiances in the spectral fitting process, aliasing occurs (Chance, 1998). Where the trace gas absorptions are optically thin, it is possible to correct for most of the undersampling error. It is also now possible to
 460 quantitatively determine the amount a spectrum will be undersampled (or, how

close it is to being fully-sampled) for a given instrument configuration during the design phase (Chance et al., 2005).

Reference spectra. Reference spectra for UV and VIS measurements are now included in the HITRAN database (Gordon et al., 2017) and regularly updated.

465 Reference spectra are published sometimes with vacuum wavelengths and sometimes with air wavelengths. It is highly recommended that vacuum wavelengths be the standard, and that accurate conversion be made when necessary. Highly accurate conversion formulae are available (Bodhaine et al., 1999). As UV and VIS reference spectra are increasingly determined using Fourier transform spectrometers, this becomes less of an issue, since they measure frequencies, usually in wavenumbers (cm^{-1}), and these are intrinsically in vacuum. Table 3 gives the current recommendations for UV and VIS reference spectra. Files containing the current recommended spectra and treatments for the Ring effect and spectral undersampling are available from kchance@cfa.harvard.edu.

475 **4. Trace gas retrievals and applications**

4.1. Ozone

Singer and Wentworth (1957) proposed a method to determine the vertical distribution of O_3 using satellite observations. Following their seminal work, the first measurements of O_3 using satellite observations date back to the 1960s.

480 Venkateswaran et al. (1961) used the Chappuis bands around 600 nm unlike most studies which benefited from measurements made by instruments designed to study backscattered solar radiation in the UV (Krasnopol'skii, 1966; Rawcliffe and Elliott, 1966; Iozenas, 1968; Anderson et al., 1969).

In April 8, 1970, the Nimbus 4 satellite was launched as part of the Nimbus program to collect weather and meteorological data. One of its payloads, the Backscatter UltraViolet (BUV) instrument was the first satellite instrument specifically designed to carry on O_3 observations (Krueger et al., 1973). Since then the concentrations of O_3 have been monitored continuously from space. The Total Ozone Monitoring Spectrometer (TOMS) (Heath et al., 1975) is a

Table 3: Recommended reference spectra and Raman treatments.

Molecule or effect	Range [nm] (vacuum)	Temperature(s) [K]	Resolution FWHM
O ₃ ^a	195-660	218, 228, 243, 273, 295	0.02 nm
NO ₂ ^b	238-667, 280-337	220, 294	1.1658 cm ⁻¹
SO ₂ ^c	227-417	203, 223, 243, 273, 293	0.21-0.26 nm
H ₂ CO ^d	300-386	223, 233, 243, 253, 263, 273, 283, 293	0.8721 cm ⁻¹
C ₂ H ₂ O ₂ ^e	370-470	296	0.01 nm
H ₂ O ^f	440-450	Atmospheric average ^f	~0.003 nm ^f
BrO ^g	286-383	228	10.49 cm ⁻¹
IO ^h	409-474	298	0.07 nm
OClO ⁱ	312-441	213, 233, 253, 273, 293	1.0 cm ⁻¹
Oxygen collision complex (O ₂ -O ₂) ^j	336-601	203, 293	0.32-0.45 nm ^j
Raman (Ring effect) ^k	200-1001	selectable	selectable
H ₂ O (l) Raman ^l	200-1001		
Undersampling ^m	N/A	N/A	Instrument-dependent
Solar reference spectrum ⁿ	200-1001	Solar T	0.04 nm

^a Derived from Daumont et al. (1992); Brion et al. (1993); Malicet et al. (1995); Brion et al. (1998); Gorshelev et al. (2014) and Serdyuchenko et al. (2014) are an alternate choice.

^b Vandaele et al. (1998)

^c Bogumil et al. (2003)

^d Chance and Orphal (2011)

^e Derived from Volkamer et al. (2005b)

^f Harder and Brault (1997). Gordon et al. (2017) is an alternate source. HITRAN improvements incorporating Harder and Brault (1997) re underway.

^g Wilmouth et al. (1999)

^h Martin et al. (2005)

ⁱ Derived from Kromminga et al. (2003)

^j Thalman and Volkamer (2013)

^k Chance and Spurr (1997)

^l Derived from Walrafen (1967)

^m Chance et al. (2005)

ⁿ Chance and Kurucz (2010)

- 490 NASA instrument designed to detect the total amount of atmospheric O₃ on a daily global scale. Launched aboard Nimbus-7 (November 1978 - May 1993), Meteor-3 (August 1991 - November 1994), ADEOS (July 1996-June 1997), and Earth Probe (July 1996 December 2005) TOMS played a pivotal role in monitoring the evolution of the O₃ hole (Gleason et al., 1993; Herman et al., 1995).
495 Another O₃ monitoring payload of Nimbus 7 was the Solar Backscatter Ultra-Violet (SBUV) designed to monitor the vertical distribution of stratospheric O₃ with a vertical resolution of ~7 km above the O₃ layer. This monitoring activity was followed by the SBUV/2 family on-board NOAA weather satellites

(1984 to now) (Frederick et al., 1986). The merged total O₃ (MOD) and profile
 500 data sets were developed using the SBUV version 8.6 processor (McPeters et al., 2013). This algorithm implements inter-instrument calibration of the radiance guaranteeing the consistency of the record (Bhartia et al., 2013). The accuracy of the data sets is proven to be within 5% with respect to high-resolution in-situ and satellite measurements (Kramarova et al., 2013; Labow et al., 2013).
 505 The original MOD time series is being expanded with data from OMPS-NP on S-NPP and NOAA-20 satellites.

Chehade et al. (2014) used the synergy between multiple satellite sensors including BUV, SBUV and SBUV/2, to analyze the long-term trend of total O₃ over 1979-2012. They found noticeable correlations between the equivalent
 510 stratospheric chlorine and the downward trend in O₃ over 1979-1997. The evolution of the Ozone Hole is monitored by TOMS, SBUV, SBUV/2, OMI, GOME-1, GOME-2, OMPS-NM and OMPS-NP with recovery detected recently as a result of adherence to the Montreal Protocol (Solomon et al., 2016; Weber et al., 2018).

To provide information about tropospheric O₃ crucial to unravel its complex origin, several tropospheric O₃ residual methods were developed by subtracting the stratospheric O₃ amount from the total O₃ column (e.g., Fishman et al., 1990; Ziemke et al., 1998, 2006). Direct estimates of O₃ profiles with sensitivity
 515 to the lower troposphere like the ones shown in Figure 3 are possible thanks to hyperspectral sensors such as GOME-1, OMI, GOME-2, and OMPS-NM (Munro et al., 1998; Hoogen et al., 1999; Hasekamp and Landgraf, 2001; van der A et al., 2002; Müller et al., 2003; Liu et al., 2005, 2010; Kroon et al., 2011; Cai et al., 2012; van Peet et al., 2014; Miles et al., 2015; Bak et al., 2017).

Sauvage et al. (2007) compared the simulations performed using the GEOS-Chem CTM with GOME-1 observations in the tropics. In addition to providing top-down constraint on biomass burning emissions, they improved the spatial distribution of lightning NO_x emissions, which in turn, mitigated the discrepancy between the model and the satellite. Similarly, Zhang et al. (2010) studied the potential causes of disagreement between the O₃ columns simu-

530 lated by the global model and observed from TES and OMI sensors. They attributed the low biased tendency of the model over the tropics to the underestimation of emissions from a combination of sources including those from lightning, biomass burning, and biogenic soil. On the other hand, the model was high biased at higher latitudes due to uncertainties associated with the
535 stratospheric-tropospheric exchange.

Satellites have paved the way for studying the spatio-temporal variations of tropospheric O₃ at a high spatial resolution where other types of observations are rather scarce. Liu et al. (2009) provided an observational evidence from GOME that tropospheric ozone in the Tibetan Plateau in June can be exceptionally low mainly due to the Asian summer monsoon. Despite the limitations associated with the low sensitivity of the UV satellites to tropospheric O₃ Kar et al. (2010) demonstrated that they have the potential for detecting urban O₃ plumes occurring episodically. To improve the sensitivity of nadir UV satellite measurements to O₃ in the free troposphere, multi-instrument retrievals have
540 been developed combining the UV Hartley-Huggins and thermal infrared O₃ bands (Cuesta et al., 2013; Fu et al., 2013, 2018).

4.2. Nitrogen dioxide

Nitrogen dioxide (NO₂), produced during combustion, is designated as a criteria pollutant by the US Environmental Protection Agency (EPA) owing to its
550 negative effects on public health and the environment. It is regulated as nitrogen oxides (NO_x = NO₂ + NO), which are precursors of O₃ and particulate matter, both of which are also criteria pollutants that have important implications for human health, crop yields, and climate. Monitoring of NO₂ concentrations is essential because NO₂ is a toxic gas at high concentrations. Epidemiological
555 studies indicate that exposure to moderate levels of NO₂ increases bronchitis and reduces lung function in children and asthmatics (Burnett et al., 2004; EPA, 2008).

NO₂ observations from satellite remote sensing provide consistent, long-term global data that complement existing ground-based networks. Satellite NO₂

560 data have been widely used to detect and quantify NO_x emission-related anthropogenic activities of large point sources such as coal-fired power plants in the US (Duncan et al., 2013; de Foy et al., 2015), China (Wang et al., 2010; Zhang et al., 2009), and India (Lu and Streets, 2012), and of large area sources such as cities in the US (Lamsal et al., 2015; Lu et al., 2015; de Foy et al., 565 2016) and around the world (Krotkov et al., 2016; Duncan et al., 2016). For instance, Figure 4 shows dramatic declines in tropospheric NO_2 over the US, western Europe, and Japan as observed by OMI from 2005 to 2017 while the opposite trends are found in some other parts of the world. Moreover, satellite NO_2 observations have been frequently used to evaluate CTMs (e.g., Kim et al., 570 2009; Hudman et al., 2012; Pope et al., 2015; Rasool et al., 2016), and study NO_x chemistry, lifetime and deposition (e.g., Lamsal et al., 2010; Nowlan et al., 2014; Tong et al., 2015).

575 NO_2 observations from satellite remote sensing exploit strong NO_2 absorption features in the VIS and near UV. Spectroscopic ground-based measurements of NO_2 date back nearly four decades (e.g., Brewer et al., 1973). They have evolved to a new generation of instruments to measure total (e.g., Pandora, (Herman et al., 2009)) and tropospheric NO_2 columns (e.g., Multi Axis DOAS, MAXDOAS). The first global tropospheric NO_2 observations were made in the middle 1990s with GOME-1 (Burrows et al., 1999). Similar measurements, but 580 at higher spatial resolution, were continued with SCIAMACHY (Bovensmann et al., 1999), OMI (Levelt et al., 2006), GOME-2 (Munro et al., 2016) and more recently TROPOMI (Veefkind et al., 2012).

Determination of the abundance of atmospheric NO_2 from satellite instruments is performed by direct fit and DOAS algorithms in the 330 nm to 500 nm 585 spectral range (Martin et al., 2002; Boersma et al., 2011; Richter et al., 2011; Valks et al., 2011; Bucsela et al., 2013; Yang et al., 2014; Marchenko et al., 2015; Boersma et al., 2018). The spectral fit procedure yields the NO_2 SCD, which represents the integrated abundance of NO_2 along the average photon path through the atmosphere. Subsequent retrieval step of the NO_2 product includes 590 the calculation of AMF to convert the SCD into a VCD. Since the satellite-

retrieved SCDs contain both tropospheric and stratospheric contributions, a separation algorithm is necessary to estimate stratospheric and tropospheric NO₂ VCDs. To properly separate the two components, the current approach is to use near-local observations over unpolluted and cloudy areas (e.g., Bucsela et al., 2013; Beirle et al., 2016). This approach takes advantage of the large contribution of stratospheric NO₂ (90%) to the total NO₂ column in unpolluted (e.g., non-coastal oceans) and overcast areas (Martin et al., 2002) and derives stratospheric NO₂ field by spatial interpolation and smoothing of NO₂ observations over those areas. An alternative to separate the tropospheric and stratospheric components is data assimilation (e.g., Boersma et al., 2011).

Estimating measurement uncertainties in satellite-observed NO₂ is critical for allowing informed use of the data, interpretation and assimilation of the data using models and estimation of errors in satellite-derived higher level products (e.g., surface NO₂ concentration, NO_x emissions). Current error estimates for satellite NO₂ products are based on the error propagation from the measurement noise with SCDs errors (typically 0.8×10^{15} molecules cm⁻²) resulting from spectral fitting itself (Marchenko et al., 2015; Zara et al., 2018) and AMF errors (30-80%) arising from various input parameters used in AMF calculations (Bucsela et al., 2013).

610 4.3. Sulfur dioxide

SO₂ in the atmosphere can impact climate and air quality on local to global scales. SO₂ is primarily produced from anthropogenic sources through the burning of fossil fuels, with smaller contributions from the smelting of sulfur-containing ores. Natural sources of SO₂ include the oxidation of dimethyl sulfide from marine phytoplankton and volcanic activity, with small contributions from biomass burning and soil and vegetation decay. In the atmosphere, SO₂ forms sulfate aerosols, which can have regional to global effects on climate (Myhre et al., 2013). When SO₂ is injected into the stratosphere during a strong volcanic eruption, the resulting sulfate aerosols may persist for over a year (McCormick et al., 1995), significantly influencing the Earth's radiation budget. Volcanic

aerosols and SO₂ can also pose a danger to aircraft. The wet and dry deposition that removes sulfur from the atmosphere results in acid deposition to the Earth's surface. SO₂ and its resulting sulfate increase mortality and morbidity rates with significant consequences for public health (Pope and Dockery, 2006; 625 World Health Organization, 2016).

The strong SO₂ absorption band in the ultraviolet was first exploited to make SO₂ measurements from space using the TOMS (Krueger, 1983) and SBUV (McPeters et al., 1984) instruments on the Nimbus-7 satellite during the 1982 El Chichón volcanic eruptions. Later, observations from TOMS and SBUV/2 630 were used to track the global transport of SO₂ from the 1991 Pinatubo eruption (Bluth et al., 1992; McPeters, 1993; Guo et al., 2004), and TOMS instruments have been used to produce over two decades of volcanic observations (Carn et al., 2003; Krueger et al., 2013).

With the advent of GOME-1 hyperspectral UV measurements, it became 635 possible to measure lower levels of SO₂ pollution from anthropogenic emissions and small volcanic eruptions (Eisinger and Burrows, 1998). SO₂ has been measured by SCIAMACHY (Afe et al., 2004; Lee et al., 2008), GOME-2 (Bobrowski et al., 2010; Nowlan et al., 2011; Rix et al., 2012), OMI (Krotkov et al., 2006; Yang et al., 2009a; Theys et al., 2015; Li et al., 2017a) and OMPS (Yang et al., 640 2013; Li et al., 2017a; Zhang et al., 2017). These measurements have been used to study trends over time (Li et al., 2010, 2017b; Fioletov et al., 2011, 2013; Lu et al., 2011; Wang et al., 2015; Krotkov et al., 2016), sulfur deposition (Nowlan et al., 2014; Fedkin et al., 2019), emissions and inventories (Lee et al., 2011; Fioletov et al., 2015, 2016; McLinden et al., 2016; Koukouli et al., 2018; Liu 645 et al., 2018) and volcanic fluxes (Theys et al., 2013; Carn et al., 2015, 2016), as well as in aviation safety applications (Carn et al., 2009; Krotkov et al., 2014; Brenot et al., 2014).

SO₂ retrievals in the UV are complicated by the presence of O₃ absorption and strong molecular Rayleigh scattering. SO₂ retrievals have typically used 650 the wavelength range of 310-330 nm, where light is not fully extinguished by the O₃ bands or Rayleigh scattering, and where SO₂ absorption contains strong

differential spectral features. However, strong O₃ absorption in this spectral region means uncertainties in O₃ column amount and instrument calibration can drastically affect SO₂ retrievals, and both O₃ and Rayleigh scattering cause
 655 the AMF to change significantly as a function of SO₂ height and wavelength. Uncertainties are particularly prominent for volcanic cases, where plume height may be uncertain, significant aerosol loading can occur, and in the case of large SO₂ loading, there is non-linearity in the backscatter radiance due to the suppression of photon scattering inside the plume.

660 The different altitude penetration depths at different wavelengths due to O₃ and Rayleigh scattering can, however, provide information on SO₂ plume height, and have been exploited to retrieve plume height in cases of moderate and large volcanic eruptions (Yang et al., 2009b, 2010; Nowlan et al., 2011). Several retrieval approaches have been applied to improve SO₂ retrievals in the
 665 UV, including weighting function DOAS (Lee et al., 2008), iterative spectral fitting (Yang et al., 2009a, 2010), optimal estimation (Nowlan et al., 2011), principal component analysis (PCA) (Li et al., 2013, 2017a), and the use of the weaker SO₂ absorption feature in the 360-390 nm region for strong volcanic cases (Bobrowski et al., 2010; Theys et al., 2017). Despite these approaches,
 670 SO₂ retrievals often suffer from high biases in the background (greater than 100%), particularly at high SZA, which often necessitate empirical bias corrections either by retrieval algorithms (e.g., Theys et al., 2017) or in post-processing science studies (e.g., Fioletov et al., 2013).

675 Declining SO₂ emissions in developed countries (Krotkov et al., 2016; Koukouli et al., 2018) mean that anthropogenic SO₂ is becoming more difficult to measure from space using most current spaceborne instruments. However, the deployment of instruments with increasingly high spatial resolution in LEO and GEO orbits will allow the resolution of individual plumes and facilitate high-accuracy emission estimation. Applications of new retrieval techniques may
 680 also provide new opportunities in the applications of UV SO₂ data. For example, near-real-time retrievals of volcanic plume height enabled by machine learning (e.g., Efremenko et al., 2017) have potential uses in aviation safety

management, the monitoring of geoengineering using SO₂ to produce sulfate aerosol (e.g., Niemeier and Timmreck, 2015) and the study of volcanic effects
685 on climate.

4.4. Formaldehyde

Global observations of H₂CO from space were first reported using GOME-1 measurements. Chance et al. (2000) used a direct fit of the distinct H₂CO absorption in the UV to derive SCDs and RTM calculations of AMFs to convert
690 them to VCDs (Palmer et al., 2001). After this seminal work, retrievals of H₂CO have been developed with SCIAMACHY, OMI, GOME2-A/B, S-NPP OMPS-NM and TROPOMI measurements (Kurosu et al., 2004; Wittrock et al., 2006; De Smedt et al., 2008, 2012, 2018; González Abad et al., 2015, 2016; Vrekoussis et al., 2010; Hewson et al., 2015; Li et al., 2015; Zara et al., 2018).
695 Oxidation of CH₄ and NMVOCs are the major sources of atmospheric H₂CO. Background levels are determined by CH₄ oxidation. Secondary production due to oxidation of VOCs from vegetation, biomass burning, on-road vehicles and industry (Barkley et al., 2013; Zhu et al., 2014) or direct emissions from industry is the origin of regional enhancements.

The H₂CO lifetime of few hours favours its utilization as a satellite-derived proxy for VOCs emissions. Considerable amounts of research exploiting this application have provided top-down constraints on bottom-up biomass burning and biogenic VOC emissions inventories used in chemical transport models (Millet et al., 2006, 2008; Stavrakou et al., 2009b,c; Marais et al., 2012; Bauwens
705 et al., 2016). Shim et al. (2005) performed a Bayesian inversion of global isoprene emissions using GOME-1 H₂CO columns from September 1996 to August 1997. Their inversion estimate mitigated the underestimation of isoprene emissions (~50%), particularly over the tropics. Changing the global biogenic emissions reduced OH concentration by 11% in the model, showing that satellite derived
710 H₂CO provides information on the oxidation capacity of the atmosphere (Valin et al., 2016; Jin et al., 2017). Likewise, Palmer et al. (2006) provided an optimal estimation of isoprene emissions over North America using GOME-1 observa-

tions. They found a 25% seasonal bias associated with biogenic emissions higher (lower) at the beginning (end) of the growing season.

The long-term stability of the OMI sensor and inter calibration efforts has allowed the observation of multi-decadal trends of H₂CO around the world (De Smedt et al., 2010, 2015; Choi and Souri, 2015a,b; Jin and Holloway, 2015; Barkley et al., 2017; Souri et al., 2017; Zhu et al., 2017). De Smedt et al. (2010) studied long-term trends of H₂CO using GOME-1 and SCIAMACHY observations between 1997 and 2009. Enhanced anthropogenic VOC emissions caused by rapid economic and population growth in China and India, resulted in positive H₂CO trends. Opposite to this behaviour, cities in Japan and the northeast U.S. underwent downward trends reflecting the effectiveness of emission control policies. OMI revealed positive trends over China (De Smedt et al., 2015; Souri et al., 2017) with the exception of the Pearl River Delta, a region where air quality has improved due to controls on VOC emissions imposed by the eleventh five-year-plan (Zhong et al., 2013). Zhu et al. (2017) reported trends of OMI H₂CO columns across North America in the 2005–2014 period. Reduction of H₂CO was observed in the Houston-Galveston-Brazoria area, home to petrochemical facilities (Choi and Souri, 2015a; Zhu et al., 2017) while columns increased in the Cold Lake Oil sands in Canada in line with the rapid increase in crude oil production.

Despite all these scientific applications of current and past H₂CO retrievals, challenges owing to small H₂CO atmospheric optical depth still need to be addressed. For individual pixels the random error of the SCD dominates the uncertainty with values between 100% to 300% percent (De Smedt et al., 2015) depending on the instrument SNR. These random errors can be reduced by averaging in the spatial and temporal domain at the cost of reduced resolutions. Systematic uncertainties in the slant column determination are linked to the choice of reference cross sections and fitting parameters. A-priori information used in AMF calculations (surface reflectance properties, vertical distribution of H₂CO, cloud contamination, presence of aerosols) is also affected by uncertainties (Lorente et al., 2017). It is of paramount importance for the development

of robust products suitable for use in chemical forecast and data assimilation
 745 to use consistent reference data and a-priori information. For example, while
 González Abad et al. (2016) use Chance and Orphal (2011) De Smedt et al.
 (2018) use Meller and Moortgat (2000) H₂CO cross sections. To reduce SCD
 fitting uncertainties and reduce interference from other trace gases active in
 the same spectral range such as BrO higher spectral resolution instruments will
 750 help. However, designs based on dispersing grating spectrometers make SNR
 and spectral resolution compete against each other.

Initiatives like the QA4ECV (Zara et al., 2018) program and the NASA's
 MEaSUREs program aim to develop robust, reliable and traceable data records
 extending multiple decades combining measurements by multiple instruments
 755 deployed in different space crafts. These initiatives require fiducial correla-
 tive datasets to perform validation studies. Until recent years H₂CO validation
 records were sparse. Recent advances in ground-based remote sensing (Irie et al.,
 2008; Vigouroux et al., 2018; Spinei et al., 2018) and in-situ aircraft measure-
 ments (Fried et al., 2003; Richter et al., 2015; Cazorla et al., 2015) result in
 760 rigorous validation exercises (Vigouroux et al., 2009; Zhu et al., 2016). Develop-
 ing a strategy to perform these studies in a consistent way across instruments
 and locations is a-priority to increase the value of H₂CO satellite datasets. Fig-
 ure 5 shows East Asia S-NPP OMPS-NM H₂CO retrievals during KORUS-AQ
 (Spinei et al., 2018) where there are correlative ground-based and aircraft mea-
 765 surements. These field experiments provide opportunities to validate not only
 satellite data but also a-priori information used in the retrievals.

4.5. Bromine monoxide

Odd bromine chemistry is a significant contributor to global O₃ loss, particu-
 larly due to synergistic chemical cycles with odd chlorine chemistry (von Glasow
 et al., 2004; Salawitch et al., 2005). Its main stratospheric sources are CH₃Br
 (partly natural, partly anthropogenic), halons (currently being largely phased
 out) and, increasingly, very short-lived substances containing bromine (Paw-
 son et al., 2014). Tropospheric sources include polar spring rapid release (e.g.,
 770

Hausmann and Platt, 1994; Simpson et al., 2007; Abbatt et al., 2012; Blechschmidt et al., 2016), volcanos (e.g., Bobrowski et al., 2003), salt lakes (e.g., Hebestreit et al., 1999) and stratospheric transport (Salawitch et al., 2010). Polar Spring BrO enhancements are known to be associated with boundary layer O₃ depletion (Choi et al., 2018). Measurements of BrO have been used together with chemical and dynamical modeling to investigate stratospheric versus tropospheric enhancements of atmospheric BrO at high northern latitudes, including the effects of very short lived stratospheric bromocarbons, such as CH₂Br₂, in the total BrO columns (Salawitch et al., 2010; Toyota et al., 2011).

BrO was initially expected to be measurable from space in regions with stratospheric enhancements. While these enhancements are associated with the polar vortices, sensitivity studies for SCIAMACHY and GOME-1 determined that BrO should be measurable globally (Chance et al., 1991). When spectra from GOME-1 became available there were four nearly simultaneous publications of initial BrO measurements (Richter et al., 1998; Hegels et al., 1998; Chance, 1998; Platt and Wagner, 1998). Each demonstrated the expected variation of stratospheric BrO with SZA and each saw localized enhancements, apparently in the troposphere, at high latitudes. Richter et al. (1998); Hegels et al. (1998); Platt and Wagner (1998) used the DOAS approach for spectral analysis (Platt, 2006) while Chance (1998) directly fitted the radiance spectra. Chance (1998) also introduced the use of in-flight wavelength calibration using a solar reference spectrum (Caspar and Chance, 1997; Chance and Spurr, 1997; Chance and Kurucz, 2010), the undersampling correction (cf. Chance et al., 2005), the rotational Raman (Ring) correction including the O₂ ground state $^3\Sigma^-g$ structure (Chance and Spurr, 1997), and the now widely used common-mode correction. BrO is measured in the $A^2\Pi_{3/2} \leftarrow X^2\Pi_{3/2}$ ultraviolet transition, in spectral windows centered near 350 nm. Additional molecular absorbers included in the fitting are normally O₃, NO₂, OCLO, H₂CO, SO₂, and the O₂-O₂ collision complex.

After the initial GOME-1 studies demonstrated that BrO is one of the easier trace molecules to measure from space in these wavelengths, satellite BrO re-

trievals were developed using SCIAMACHY (e.g., van Roozendael et al., 2004), GOME-2 (e.g., Theys et al., 2009), OMI (e.g., Kurosu et al., 2004; Suleiman et al., 2018; Hörmann et al., 2016), OMPS-NM (González Abad et al., 2017), and TROPOMI (Seo et al., 2018) radiances. Hörmann et al. (2016) monitored the seasonal cycle of BrO formation over the Rann of Kutch, one of the largest salt marshes in the world, using OMI and GOME-2 observations. They concluded that the Rann of Kutch is one of the strongest natural sources of BrO outside the polar regions possibly having significant impacts in the local and regional O₃ chemistry. Enhancements of BrO over the Great Salt Lake and the Dead Sea have also been observed by OMI (Hörmann et al., 2016; Suleiman et al., 2018). High concentration of BrO was observed in the plume of the Ambrym volcano eruption in 2005 by Chance (2006) confirming previous ground-based observations (Bobrowski et al., 2003). Later studies have identified BrO in at least several different volcano plumes (Hörmann et al., 2013) including the Kasatochi 2008 eruption (Theys et al., 2009) and the Eyjafjallajökull 2010 (Heue et al., 2011; Rix et al., 2012).

4.6. Water vapor

Water vapor is one of the state variables measured since the beginning of the satellite era. Here, we only focus on the satellite measurements made in the visible wavelength range. Total Column Water Vapor (TCWV, also referred to as Integrated Water Vapor or Precipitable Water Vapor) can be retrieved in the near red, red, and blue wavelength range using the spectra obtained by GOME-1 (Noël et al., 1999; Wagner et al., 2003; Lang et al., 2007), SCIAMACHY (Noël et al., 2004; Piesanis et al., 2013), GOME-2 (Grossi et al., 2015) and OMI (Wang et al., 2016). The GOME-1, SCIAMACHY and GOME-2 TCWV derived from the red spectral range (Grossi et al., 2015) are combined into a homogenized monthly climate product at 1° horizontal resolution from July 1995 to December 2015 (Beirle et al., 2018).

TCWV retrievals in the near red and red spectral range use the DOAS method or its variations. As water vapor absorption is relatively strong in

835 this spectral region, individual lines can get saturated when TCWV is large. Since individual spectral lines are not resolved by the instruments, the measured differential absorption varies non-linearly with the actual TCWV. This non-linear saturation effect needs to be corrected in the retrieval.

TCWV can also be derived from the blue spectral range (Wagner et al., 840 2013), as shown by the example in Figure 6 (Wang et al., 2014, 2016). Given the weak absorption of water vapor in the blue wavelength range, it is not necessary to perform any saturation correction for the SCDs, though the fitting uncertainty is larger compared to that for the red spectral range due to reduced SNR, especially when TCWV is low (< 10 mm). Since GOME-1, 845 SCHIAMACHY and GOME-2 all cover the blue wavelength range, they can be combined with OMI to generate a long-term TCWV dataset.

Water vapor is crucial for understanding Earth's climate. It is the predominant greenhouse gas in the atmosphere and can amplify the warming associated with other greenhouse gases, such as CO₂ and CH₄. Water vapor is also 850 important for the hydrological cycle and energy budget. Through condensation, it leads to cloud formation and latent heat release, directly influencing the weather and atmospheric circulation. The tropospheric profile, stratospheric profile and total column of H₂O vapor are included by the Global Climate Observing System as ECVs that critically contribute to the characterization 855 of the climate system (<https://www.ncdc.noaa.gov/gosic/gcos-essential-climate-variable-ecv-data-access-matrix>). TCWV can be calculated by integrating water vapor profiles or retrieved from visible/NIR/IR/Microwave/GPS observations.

Water vapor is highly variable in space and time. Thus, observations on a variety of spatio-temporal scales are required to characterize its distribution. 860 Many in-situ and remote sensing techniques are used to measure water vapor concentration or total column from ground stations, aircrafts and satellites. Ground-based data provide nice temporal coverage; Aircraft data provide fine vertical resolution; Satellite data provide global perspective.

A review of satellite derived water vapor data is provided by the GEWEX 865 Water Vapor Assessment (Schröder et al., 2018). These data result from satel-

lite remote sensing in the visible/NIR/Shortwave IR/IR/microwave/GPS wavelength range. Each dataset has its own resolution, spatial and temporal coverage and characteristics. For example, data from GPS occultation are available for all weather conditions, but have relatively sparse spatial coverage; data from microwave observations are available for both clear-sky and cloudy-sky conditions, but are affected by precipitation and are usually available only over the oceans; data from NIR and shortwave IR observations are typically available only over land and are strongly affected by clouds; data from IR observations are available over both land and the oceans, but have low sensitivity in the boundary layer and are strongly affected by clouds; data from visible observations are sensitive to the boundary layer and are available for all surface types, but are strongly affected by clouds.

Satellite TVWC products are typically validated against measurements from ground-based networks, such as the radiosondes of the GCOS Reference Upper-Air Network (GRUAN) Seidel et al. (2009), the GPS data of the International GNSS Service archived at NCAR (Wang et al., 2007) or SuomiNet GPS data provided by UCAR (Ware et al., 2000), and the microwave radiometer data of the Department of Energy ARM program (Cadeddu et al., 2013). These reference datasets are usually accurate and precise to sub-mm level (Dirksen et al., 2014; Ning et al., 2016) and are well suited for satellite data validation. The version 2 sun photometer data from AERONET (Holben et al., 1998) has a dry bias of 5% and an estimated uncertainty of 13% (Pérez-Ramírez et al., 2014). Version 3 AERONET data released in 2018 are expected to have better quality and may be useful for satellite data validation.

Since most of the ground-based stations are over land, validation over the ocean is usually conducted against the TCWV derived from satellite microwave sensors. Microwave observations of TCWV are considered to have high quality over the ice-free non-precipitating ocean (Mears et al., 2015b,a). Remote Sensing Systems provides Version 7 TCWV data for SSM/I, SSMIS, AMSRE, and Wind-Sat on $0.25^\circ \times 0.25^\circ$ grid over the oceans twice per day. These data have also been homogenized into a monthly $1^\circ \times 1^\circ$ climate data record starting in 1988 (Mears

et al., 2018). Alternatively, the EUMETSAT Satellite Application Facility on Climate Monitoring provides $0.5^\circ \times 0.5^\circ$ 6-hourly and monthly TCWV climate data records (1987-2014) derived from SSM/I and SSMIS using the Hamburg
900 Ocean Atmosphere Parameters and Fluxes from Satellite Data Version 4 algorithm (<https://wui.cmsaf.eu/safira/action/viewProduktSearch>).

In addition satellite datasets that compare well with the reference data mentioned above may be useful for validation. In particular, the TCWV retrieved from the OCO-2 shortwave IR data (Nelson et al., 2016) and the TCWV integrated using the COSMIC GPS radio occultation profiles (Ho et al., 2018) may
905 serve as references.

4.7. Glyoxal

The possibility of observing $\text{C}_2\text{H}_2\text{O}_2$ from space was first suggested by Volkamer et al. (2005a), after they observed high concentrations in Mexico City. Their
910 observations translated to satellite optical depths of up to 1.7×10^{-3} in the 400 to 500 nm spectral range, however typical optical depths of $\text{C}_2\text{H}_2\text{O}_2$ are usually much smaller ($\sim 10^{-4}$). Given the current capabilities of VIS space-borne detectors and the typical amount of $\text{C}_2\text{H}_2\text{O}_2$ these are the most challenging retrievals discussed here. Adding to the problem is the limited amount of measurements
915 for validation. Ground-based remote sensing measurements of $\text{C}_2\text{H}_2\text{O}_2$ are also affected by high uncertainties derived from its weak absorption and in-situ measurements of $\text{C}_2\text{H}_2\text{O}_2$ in field campaigns are scarce. Despite these adversities several $\text{C}_2\text{H}_2\text{O}_2$ retrievals have been developed over the years.

The first global observations of $\text{C}_2\text{H}_2\text{O}_2$ were derived using GOME-1 and
920 SCIAMACHY measurements (Chance, 2006; Wittrock et al., 2006). Subsequent efforts have resulted in the development of GOME-2 (Lerot et al., 2010; Vrekoussis et al., 2010) and OMI $\text{C}_2\text{H}_2\text{O}_2$ retrievals (Alvarado et al., 2014; Chan Miller et al., 2014). The work by Wittrock et al. (2006) showed spatial correlations between $\text{C}_2\text{H}_2\text{O}_2$ and H_2CO . This is because both species are short-lived products
925 of VOC oxidation, with isoprene being the dominant precursor of both.

Studying the ratio of $\text{C}_2\text{H}_2\text{O}_2$ and H_2CO can provide insights into the VOC

precursors and chemical pathways leading to their formation (Wittrock et al., 2006; Vrekoussis et al., 2010; Kaiser et al., 2015; Chan Miller et al., 2016, 2017).

Vrekoussis et al. (2010) found a noticeable decreasing trend between the C₂H₂O₂ to H₂CO ratio and NO₂ columns over major cities around the world using GOME-2 data, which they suggest could be driven by shifts in the identity of predominant anthropogenic VOC precursors. Using the GEOS-Chem model and OMI data Chan Miller et al. (2017) tested the C₂H₂O₂ yield from isoprene and its dependence on nitrogen oxides. They found that the formation of C₂H₂O₂ is dominated by the isomerization of isoprene peroxy radicals under low nitrogen oxide conditions. Kaiser et al. (2015) used a combined set of OMI and aircraft observations over the Southeast US to evaluate the effectiveness of using this ratio as a hydrocarbon source indicator. They found that regions with high C₂H₂O₂ to H₂CO ratio were primarily associated with monoterpene emissions, whereas isoprene-rich areas led to comparatively lower values.

Stavrakou et al. (2009a) carried on inverse modeling experiments using SCIAMACHY data over continents. These studies reveled significant C₂H₂O₂ chemical transport models underestimations. Space-based constraints on direct VOC emissions from biogenic, pyrogenic and anthropogenic emissions partially reduced the underestimation of the simulated C₂H₂O₂ columns but it resulted in large overestimations of surface C₂H₂O₂ concentrations. Adding a secondary formation pathway of an unspecified precursor they found it to be the largest contributor (50%) to the C₂H₂O₂ budget. This ambiguity underscores the importance of improving our understanding of C₂H₂O₂ formation if realistic top-down constraints on the relevant emissions are to be provided (Chan Miller et al., 2016; Silva et al.).

5. Conclusion

The 1970 launch of the BUV instrument as a payload on-board Nimbus-4 initiated the era of global and regular space observations of atmospheric O₃. Since then, the evolution and improvement of space instruments able to observed the

Earth's atmosphere has been remarkable. The BUV instrument was capable of measuring twelve spectral channels with a spatial resolution of $200 \times 200 \text{ km}^2$, achieving global coverage in ten days. TROPOMI, launched in 2017, has hyperspectral capabilities covering the 270-775 nm range with a spatial resolution of $3.5 \times 7 \text{ km}^2$ and daily global coverage. Future GEO instruments (GEMS, TEMPO and Sentinel 4) will also measure at high spatial resolution while providing hourly observations. Early instruments enabled the development of O₃ and SO₂ retrievals. Later instruments, thanks to their hyperspectral capabilities, allowed retrievals of other trace gases including tropospheric O₃, NO₂, H₂CO, H₂O, BrO and C₂H₂O₂.

The information provided by these retrievals is valuable to understand a broad range of scientific questions with important societal implications. After the early studies monitoring the evolution of stratospheric O₃, the improvement of space-based instrument capabilities has led to investigations on atmospheric chemistry and atmospheric dynamics, studies assessing the impact of air quality policies and economic activity in pollution trends and transport and epidemiologic studies quantifying the health implications of pollution on a global scale.

Looking to the future, the value of historic records and future measurements can be further expanded by developing long-term, consistent data records using inter-calibrated measurements from different instruments. These long-term records will help monitor the current and past global change of the Earth system, reducing the uncertainty in the trends derived from them and providing a solid baseline to calibrate future missions.

As scientific retrievals become mature and ready to transition into operational frameworks, improving the characterization of errors is imperative. Data assimilation and air quality managers need detailed retrieval error information to fully exploit them. Recent efforts to increase the amount and quality of reference measurements for satellite validation should be exploited to establish rigorous validation procedures.

Ensuring the continuity of current LEO measurements and GEO missions should be a priority. The planned follow up missions to GEMS (East Asia)

and Sentinel-4 (Europe) instruments extend into the third decade of the first century. Over North America, the TEMPO mission has a required operational period of two years (contractually extendable up to ten years) with no follow ⁹⁹⁰ up mission currently planned. In the future it will be desirable to extend the spatial coverage of GEO observations to South America, Africa and Oceania.

The continuous push towards higher spatial resolution results in enormous amounts of data. New retrieval frameworks together with optimized processing and distribution data centers are necessary to ensure near-real time production ⁹⁹⁵ of higher level products dependent on this satellite retrievals such as chemical forecasts. After fifty years of development and evolution, space-based instruments and retrievals designed to monitor O₃ and air quality are ready to become part of our social push for healthier life styles.

Acknowledgements

¹⁰⁰⁰ The authors will like to thank NASA, NOAA and ESA for their continuous support and long-term efforts to provide Earth's atmosphere satellite observations. In particular this review was written with support from NASA grants 80NSSC18K0691 and 80NSSC18M0091.

References

¹⁰⁰⁵ References

- Abbatt, J.P.D., Thomas, J.L., Abrahamsson, K., Boxe, C., Granfors, A., Jones, A.E., King, M.D., Saiz-Lopez, A., Shepson, P.B., Sodeau, J., Toohey, D.W., Toubin, C., von Glasow, R., Wren, S.N., Yang, X., 2012. Halogen activation via interactions with environmental ice and snow in the polar lower troposphere and other regions. *Atmos. Chem. Phys.* 12, 6237–
¹⁰¹⁰ 6271. URL: <https://www.atmos-chem-phys.net/12/6237/2012/>, doi:10.5194/acp-12-6237-2012.

Afe, O.T., Richter, A., Sierk, B., Wittrock, F., Burrows, J.P., 2004. BrO emission from volcanoes: A survey using gome and sciamachy measurements.

¹⁰¹⁵ Geophys. Res. Lett. 31, L24113. URL: <https://agupubs.onlinelibrary.wiley.com/doi/abs/10.1029/2004GL020994>, doi:10.1029/2004GL020994.

Alvarado, L.M.A., Richter, A., Vrekoussis, M., Wittrock, F., Hilboll, A., Schreier, S.F., Burrows, J.P., 2014. An improved glyoxal retrieval from OMI measurements. Atmos. Meas. Tech. 7, 4133–4150. URL: <https://www.atmos-meas-tech.net/7/4133/2014/>, doi:10.5194/amt-7-4133-2014.

¹⁰²⁰ Anderson, G., Barth, C., Cayla, F., London, J., 1969. Satellite observations of the vertical ozone distribution in the upper stratosphere (Ozone vertical distribution in upper stratosphere determined from OGO 4 observations, describing calibration of satellite data and onboard instrumentation). Annales de Geophysique 25, 341–345.

Bak, J., Liu, X., Kim, J.H., Haffner, D.P., Chance, K., Yang, K., Sun, K., 2017. Characterization and correction of OMPS nadir mapper measurements for ozone profile retrievals. Atmos. Meas. Tech. 10, 4373–4388. URL: <https://www.atmos-meas-tech.net/10/4373/2017/>, doi:10.5194/amt-10-4373-2017.

¹⁰²⁵ Barkley, M.P., De Smedt, I., VanRoozendael, M., Kurosu, T.P., Chance, K., Arneth, A., Hagberg, D., Guenther, A., Paulot, F., Marais, E., Mao, J., 2013. Top-down isoprene emissions over tropical South America inferred from SCIAMACHY and OMI formaldehyde columns. J. Geophys. Res. Atmos. 118, 6849–6868. URL: <https://agupubs.onlinelibrary.wiley.com/doi/full/10.1002/jgrd.50552>, doi:10.1002/jgrd.50552.

¹⁰³⁵ Barkley, M.P., González Abad, G., Kurosu, T.P., Spurr, R., Torbatian, S., Lerot, C., 2017. OMI air-quality monitoring over the Middle East. Atmos. Chem. Phys. 17, 4687–4709. URL: <https://www.atmos-chem-phys.net/17/4687/2017/>, doi:10.5194/acp-17-4687-2017.

- Barrie, L., 2006. An integrated global atmospheric chemistry observations strategy and WMOs leading role: GAW & IGACO, in: Seminar on Global earth-system monitoring, 5-9 September 2005, ECMWF, Shinfield Park, Reading. pp. 35–41. URL: <https://www.ecmwf.int/node/7954>.
- ¹⁰⁴⁵ Bates, D., 1984. Rayleigh scattering by air. *Planet. Space Sci.* 32, 785 – 790. URL: <http://www.sciencedirect.com/science/article/pii/0032063384901028>, doi:10.1016/0032-0633(84)90102-8.
- ¹⁰⁵⁰ Bauwens, M., Stavrakou, T., Müller, J.F., De Smedt, I., Van Roozendael, M., van der Werf, G.R., Wiedinmyer, C., Kaiser, J.W., Sindelarova, K., Guenther, A., 2016. Nine years of global hydrocarbon emissions based on source inversion of OMI formaldehyde observations. *Atmos. Chem. Phys.* 16, 10133–10158. URL: <https://www.atmos-chem-phys.net/16/10133/2016/acp-16-10133-2016.html>, doi:10.5194/acp-16-10133-2016.
- ¹⁰⁵⁵ Beirle, S., Hörmann, C., Jöckel, P., Liu, S., Penning de Vries, M., Pozzer, A., Sihler, H., Valks, P., Wagner, T., 2016. The STRatospheric Estimation Algorithm from Mainz (STREAM): estimating stratospheric NO₂ from nadir-viewing satellites by weighted convolution. *Atmos. Meas. Tech.* 9, 2753–2779. URL: <https://www.atmos-meas-tech.net/9/2753/2016/>, doi:10.5194/amt-9-2753-2016.
- ¹⁰⁶⁰ Beirle, S., Lampel, J., Wang, Y., Mies, K., Dörner, S., Grossi, M., Loyola, D., Dehn, A., Danielczok, A., Schröder, M., Wagner, T., 2018. The ESA GOME-Evolution "Climate" water vapor product: a homogenized time series of H₂O columns from GOME, SCIAMACHY, and GOME-2. *Earth Syst. Sci. Data* 10, 449–468. URL: <https://www.earth-syst-sci-data.net/10/449/2018/>, doi:10.5194/essd-10-449-2018.
- ¹⁰⁶⁵ Bernath, P.F., McElroy, C.T., Abrams, M.C., Boone, C.D., Butler, M., Camy-Peyret, C., Carleer, M., Clerbaux, C., Coheur, P.F., Colin, R., DeCola, P., DeMazire, M., Drummond, J.R., Dufour, D., Evans, W.F.J., Fast, H., Fussen, D., Gilbert, K., Jennings, D.E., Llewellyn, E.J., Lowe, R.P.,

- 1070 Mahieu, E., McConnell, J.C., McHugh, M., McLeod, S.D., Michaud, R.,
 Midwinter, C., Nassar, R., Nichitiu, F., Nowlan, C., Rinsland, C.P., Ro-
 chon, Y.J., Rowlands, N., Semeniuk, K., Simon, P., Skelton, R., Sloan,
 J.J., Soucy, M.A., Strong, K., Tremblay, P., Turnbull, D., Walker, K.A.,
 Walkty, I., Wardle, D.A., Wehrle, V., Zander, R., Zou, J., 2005. At-
 mospheric chemistry experiment (ACE): Mission overview. *Geophys. Res.*
 Lett. 32. URL: <https://agupubs.onlinelibrary.wiley.com/doi/abs/10.1029/2005GL022386>, doi:10.1029/2005GL022386.
- 1075
 Bhartia, P.K., McPeters, R.D., Flynn, L.E., Taylor, S., Kramarova, N.A., Frith,
 S., Fisher, B., DeLand, M., 2013. Solar Backscatter UV (SBUV) total ozone
 1080 and profile algorithm. *Atmos. Meas. Tech.* 6, 2533–2548. URL: <https://www.atmos-meas-tech.net/6/2533/2013/>, doi:10.5194/amt-6-2533-2013.
- 1085 Blechschmidt, A.M., Richter, A., Burrows, J.P., Kaleschke, L., Strong, K.,
 Theys, N., Weber, M., Zhao, X., Zien, A., 2016. An exemplary case of a
 bromine explosion event linked to cyclone development in the Arctic. *Atmos.*
 1090 *Chem. Phys.* 16, 1773–1788. URL: <https://www.atmos-chem-phys.net/16/1773/2016/>, doi:10.5194/acp-16-1773-2016.
- Bluth, G.J., Doiron, S.D., Schnetzler, C.C., Krueger, A.J., Walter,
 L.S., 1992. Global tracking of the SO₂ clouds from the June,
 1095 1991 Mount Pinatubo eruptions. *Geophys. Res. Lett.* 19, 151–
 154. URL: <https://agupubs.onlinelibrary.wiley.com/doi/abs/10.1029/91GL02792>, doi:10.1029/91GL02792.
- Bobrowski, N., Hönninger, G., Galle, B., Platt, U., 2003. Detection of bromine
 monoxide in a volcanic plume. *Nature* 423, 273–276. URL: <https://doi.org/10.1038/nature01625>, doi:10.1038/nature01625.
- 1095 Bobrowski, N., Kern, C., Platt, U., Hörmann, C., Wagner, T., 2010. Novel SO₂
 spectral evaluation scheme using the 360–390 nm wavelength range. *Atmos.*
Meas. Tech. 3, 879–891. URL: <http://www.atmos-meas-tech.net/3/879/2010/>, doi:10.5194/amt-3-879-2010.

- Bodhaine, B.A., Wood, N.B., Dutton, E.G., Slusser, J.R., 1999. On Rayleigh
 1100 Optical Depth Calculations. *J. Atmos. Oceanic Technol.* 16, 1854–1861.
 URL: [https://doi.org/10.1175/1520-0426\(1999\)016<1854:ORODC>2.0.CO;2](https://doi.org/10.1175/1520-0426(1999)016<1854:ORODC>2.0.CO;2).
- Boersma, K.F., Eskes, H.J., Dirksen, R.J., van der A, R.J., Veefkind,
 1105 J.P., et al., 2011. An improved tropospheric NO₂ column retrieval algorithm for the ozone monitoring instrument. *Atmos. Meas. Tech.* 4, 1905–1928. URL: <https://www.atmos-meas-tech.net/4/1905/2011/>, doi:10.5194/amt-4-1905-2011.
- Boersma, K.F., Eskes, H.J., Richter, A., De Smedt, I., Lorente, A., Beirle, S.,
 1110 van Geffen, J.H.G.M., Zara, M., Peters, E., Van Roozendael, M., Wagner, T.,
 Maasakkers, J.D., van der A, R.J., Nightingale, J., De Rudder, A., Irie, H.,
 Pinardi, G., Lambert, J.C., Compernolle, S., 2018. Improving algorithms and
 uncertainty estimates for satellite NO₂ retrievals: Results from the Quality
 Assurance for Essential Climate Variables (QA4ECV) project. *Atmos. Meas.
 1115 Tech.* 11, 6651–6678. URL: <https://www.atmos-meas-tech.net/11/6651/2018/>, doi:10.5194/amt-11-6651-2018.
- Bogumil, K., Orphal, J., Homann, T., Voigt, S., Spietz, P., Fleischmann,
 1120 O., Vogel, A., Hartmann, M., Kromminga, H., Bovensmann, H., Frerick,
 J., Burrows”, J., 2003. Measurements of molecular absorption spectra with the SCIAMACHY pre-flight model: instrument characterization and reference data for atmospheric remote-sensing in the
 230–2380 nm region. *J. Photochem. Photobiol. A: Chemistry* 157,
 167–184. URL: <http://www.sciencedirect.com/science/article/pii/S1010603003000625>, doi:10.1016/S1010-6030(03)00062-5.
- Bovensmann, H., Burrows, J.P., Buchwitz, M., Frerick, J., Noël,
 1125 S., Rozanov, V.V., Chance, K.V., Goede, A.P.H., 1999. SCIAMACHY: Mission Objectives and Measurement Modes. *J. Atmos. Sci.* 56, 127–150. URL: <https://journals.ametsoc.org/doi/10.1175>

- 1520–0469%281999%29056%3C0127%3ASMOAMM%3E2.0.CO%3B2, doi:10.1175/1520-0469(1999)056<0127:SMOAMM>2.0.CO;2.
- ¹¹³⁰ Brenot, H., Theys, N., Clarisse, L., van Geffen, J., van Gent, J., Van Roozendael, M., van der A, R., Hurtmans, D., Coheur, P.F., Clerbaux, C., Valks, P., Hedelt, P., Prata, F., Rasson, O., Sievers, K., Zehner, C., 2014. Support to Aviation Control Service (SACS): an online service for near-real-time satellite monitoring of volcanic plumes. *Hazards Earth Syst. Sci* 14, 1099–1123. URL: <https://www.nat-hazards-earth-syst-sci.net/14/1099/2014/>, doi:10.5194/nhess-14-1099-2014.
- Brewer, A.C., McElroy, C.T., Kerr, J.B., 1973. Nitrogen dioxide concentrations in the atmosphere. *Nature* 246, 129–133. URL: <https://doi.org/10.1038/246129a0>, doi:10.1038/246129a0.
- ¹¹⁴⁰ Brion, J., Chakir, A., Charbonnier, J., Daumont, D., Parisse, C., Malicet, J., 1998. Absorption Spectra Measurements for the Ozone Molecule in the 350–830 nm region. *J. Atmos. Chem.* 30, 291–299. URL: <https://doi.org/10.1023/A:1006036924364>, doi:10.1023/A:1006036924364.
- Brion, J., Chakir, A., Daumont, D., Malicet, J., Parisse, C., 1993. High-resolution laboratory absorption cross section of O₃. Temperature effect. *Chem. Phys. Lett.* 213, 610–612. URL: <http://www.sciencedirect.com/science/article/pii/000926149389169I>, doi:10.1016/0009-2614(93)89169-I.
- ¹¹⁴⁵ Bucsela, E.J., Krotkov, N.A., Celarier, E.A., Lamsal, L.N., Swartz, W.H., Bharatia, P.K., Boersma, K.F., Veefkind, J.P., Gleason, J.F., Pickering, K.E., 2013. A new stratospheric and tropospheric NO₂ retrieval algorithm for nadir-viewing satellite instruments: application to OMI. *Atmos. Meas. Tech.* 6, 2607–2626. URL: <https://www.atmos-meas-tech.net/6/2607/2013/>, doi:10.5194/amt-6-2607-2013.
- ¹¹⁵⁵ Burnett, R.T., Stieb, D., Brook, J.R., Cakmak, S., Dales, R., Raizenne, M., Vincent, R., Dann, T., 2004. Associations between Short-Term Changes

in Nitrogen Dioxide and Mortality in Canadian Cities. *AEH* 59, 228–236.

URL: <https://doi.org/10.3200/AEOH.59.5.228-236>, doi:10.3200/AEOH.59.5.228-236.

- ¹¹⁶⁰ Burrows, J.P., Platt, U., Borrell, P. (Eds.), 2011. The Remote Sensing of Tropospheric Composition from Space. Physics of Earth and Space Environments, Springer-Verlag, Berlin Heidelberg. URL: www.springer.com/us/book/9783642147906, doi:10.1007/978-3-642-14791-3.

- Burrows, J.P., Weber, M., Buchwitz, M., Rozanov, V., Ladstätter-Weißenmayer, A., Richter, A., DeBeek, R., Hoogen, R., Bramstedt, K., Eichmann, K.U., Eisinger, M., Perner, D., 1999. The Global Ozone Monitoring Experiment (GOME): Mission Concept and First Scientific Results. *J. Atmos. Sci.* 56, 151–175. URL: [https://doi.org/10.1175/1520-0469\(1999\)056<0151:TGOME>2.0.CO;2](https://doi.org/10.1175/1520-0469(1999)056<0151:TGOME>2.0.CO;2), doi:10.1175/1520-0469(1999)056<0151:TGOME>2.0.CO;2.

- ¹¹⁷⁰ Cadeddu, M.P., Liljegren, J.C., Turner, D.D., 2013. The Atmospheric Radiation Measurement (ARM) program network of microwave radiometers: instrumentation, data, and retrievals. *Atmos. Meas. Tech.* 6, 2359–2372. URL: www.atmos-meas-tech.net/6/2359/2013/amt-6-2359-2013.html, doi:10.5194/amt-6-2359-2013.

- ¹¹⁷⁵ Cai, Z., Liu, Y., Liu, X., Chance, K., Nowlan, C.R., Lang, R., Munro, R., Suleiman, R., 2012. Characterization and correction of Global Ozone Monitoring Experiment 2 ultraviolet measurements and application to ozone profile retrievals. *J. Geophys. Res. Atmos.* 117. URL: <https://agupubs.onlinelibrary.wiley.com/doi/abs/10.1029/2011JD017096>, doi:10.1029/2011JD017096.

- ¹¹⁸⁰ Carn, S., Clarisse, L., Prata, A., 2016. Multi-decadal satellite measurements of global volcanic degassing. *J. Volcanol. Geotherm. Res.* 311, 99–134. URL: <https://www.sciencedirect.com/science/article/>

1185 pii/S0377027316000032?via%3Dihub, doi:10.1016/j.jvolgeores.2016.
 01.002.

1190 Carn, S.A., Krueger, A.J., Bluth, G.J.S., Schaefer, S.J., Krotkov, N.A., Watson,
 I.M., Datta, S., 2003. Volcanic eruption detection by the Total Ozone Map-
 ping Spectrometer (TOMS) instruments: a 22-year record of sulphur dioxide
 and ash emissions. Geological Society, London, Special Publications 213, 177–
 202. URL: <http://sp.lyellcollection.org/lookup/doi/10.1144/GSL.SP.2003.213.01.11>.
 SP.2003.213.01.11, doi:10.1144/GSL.SP.2003.213.01.11.

1195 Carn, S.A., Krueger, A.J., Krotkov, N.A., Yang, K., Evans, K., 2009. Track-
 ing volcanic sulfur dioxide clouds for aviation hazard mitigation. Nature.
 Haz. 51, 325–343. URL: <https://link.springer.com/article/10.1007%2Fs11069-008-9228-4>, doi:10.1007/s11069-008-9228-4.

1200 Carn, S.A., Yang, K., Prata, A.J., Krotkov, N.A., 2015. Extending
 the long-term record of volcanic SO₂ emissions with the Ozone Map-
 ping and Profiler Suite nadir mapper. Geophys. Res. Lett. 42, 925–
 932. URL: <https://agupubs.onlinelibrary.wiley.com/doi/abs/10.1002/2014GL062437>, doi:10.1002/2014GL062437.

1205 Caspar, C., Chance, K., 1997. GOME wavelength calibration using solar and
 atmospheric spectra, in: Third ERS Symposium on Space at the service of our
 Environment, p. 609. URL: <http://adsabs.harvard.edu/abs/1997ESASP.414..609C>.

1210 Cazorla, M., Wolfe, G.M., Bailey, S.A., Swanson, A.K., Arkinson, H.L., Hanisco,
 T.F., 2015. A new airborne laser-induced fluorescence instrument for in situ
 detection of formaldehyde throughout the troposphere and lower stratosphere.
 Atmos. Meas. Tech. 8, 541–552. URL: <https://www.atmos-meas-tech.net/8/541/2015/>, doi:10.5194/amt-8-541-2015.

1215 Chan Miller, C., González Abad, G., Wang, H., Liu, X., Kurosu, T., Jacob, D.J.,
 Chance, K., 2014. Glyoxal retrieval from the Ozone Monitoring Instrument.

Atmos. Meas. Tech. 7, 3891–3907. URL: <https://www.atmos-meas-tech.net/7/3891/2014/>, doi:10.5194/amt-7-3891-2014.

1215 Chan Miller, C., Jacob, D.J., González Abad, G., Chance, K., 2016. Hotspot
of glyoxal over the Pearl River delta seen from the OMI satellite instrument:
implications for emissions of aromatic hydrocarbons. Atmos. Chem. Phys.
16, 4631–4639. URL: <https://www.atmos-chem-phys.net/16/4631/2016/>,
doi:10.5194/acp-16-4631-2016.

1220 Chan Miller, C., Jacob, D.J., Marais, E.A., Yu, K., Travis, K.R., Kim,
P.S., Fisher, J.A., Zhu, L., Wolfe, G.M., Hanisco, T.F., Keutsch, F.N.,
Kaiser, J., Min, K.E., Brown, S.S., Washenfelder, R.A., González Abad,
G., Chance, K., 2017. Glyoxal yield from isoprene oxidation and relation
to formaldehyde: chemical mechanism, constraints from SENEX aircraft ob-
1225 servations, and interpretation of OMI satellite data. Atmos. Chem. Phys.
17, 8725–8738. URL: <https://www.atmos-chem-phys.net/17/8725/2017/>,
doi:10.5194/acp-17-8725-2017.

1230 Chance, K., 1998. Analysis of BrO measurements from the Global
Ozone Monitoring Experiment. Geophys. Res. Lett. 25, 3335–
3338. URL: <https://agupubs.onlinelibrary.wiley.com/doi/abs/10.1029/98GL52359>, doi:10.1029/98GL52359.

1235 Chance, K., 2006. Spectroscopic Measurements of Tropospheric Composition
from Satellite Measurements in the Ultraviolet and Visible: Steps Toward
Continuous Pollution Monitoring from Space, in: Perrin, A., Ben Sari-Zizi,
N., Demaison, J. (Eds.), Remote Sensing of the Atmosphere for Environ-
mental Security. NATO Security through Science Series (NATO Security
through Science Series C: Environmental Security, Springer Dordrecht. pp.
1–25. doi:10.1007/978-1-4020-5090-9_1.

1240 Chance, K., Kurosu, T.P., Sioris, C.E., 2005. Undersampling correc-
tion for array detector-based satellite spectrometers. Appl. Opt. 44,

1296–1304. URL: <https://www.osapublishing.org/ao/abstract.cfm?uri=ao-44-7-1296>, doi:10.1364/AO.44.001296.

Chance, K., Kurucz, R.L., 2010. An improved high-resolution solar reference spectrum for earth's atmosphere measurements in the ultraviolet, visible, and near infrared. *J. Quant. Spectrosc. Radiat. Transf.* 111, 1245 1289–1295. URL: <http://www.sciencedirect.com/science/article/pii/S0022407310000610>, doi:10.1016/j.jqsrt.2010.01.036.

Chance, K., Orphal, J., 2011. Revised ultraviolet absorption cross sections of H₂CO for the HITRAN database. *J. Quant. Spectrosc. Radiat. Transf.* 112, 1250 1509–1510. URL: <http://www.sciencedirect.com/science/article/pii/S002240731100080X>, doi:10.1016/j.jqsrt.2011.02.002.

Chance, K., Palmer, P.I., Spurr, R.J.D., Martin, R.V., Kurosu, T.P., Jacob, D.J., 2000. Satellite observations of formaldehyde over North America from GOME. *Geophys. Res. Lett.* 27, 3461–1255 3464. URL: <https://agupubs.onlinelibrary.wiley.com/doi/abs/10.1029/2000GL011857>, doi:10.1029/2000GL011857.

Chance, K.V., Burrows, J.P., Schneider, W., 1991. Retrieval and molecule sensitivity studies for the global ozone monitoring experiment and the scanning imaging absorption spectrometer for atmospheric chartography, in: Remote Sensing of Atmospheric Chemistry, SPIE. pp. 151–166. URL: <https://doi.org/10.1117/12.46657>, doi:10.1117/12.46657.

Chance, K.V., Spurr, R.J.D., 1997. Ring effect studies: Rayleigh scattering, including molecular parameters for rotational Raman scattering, and the Fraunhofer spectrum. *Appl. Opt.* 36, 5224–5230. URL: <https://www.osapublishing.org/ao/abstract.cfm?uri=ao-36-21-5224>, doi:10.1364/AO.36.005224.

Chehade, W., Weber, M., Burrows, J.P., 2014. Total ozone trends and variability during 1979–2012 from merged data sets of various satellites. *Atmos. Chem.*

- Phys. 14, 7059–7074. URL: <https://www.atmos-chem-phys.net/14/7059/>
 1270 2014/, doi:10.5194/acp-14-7059-2014.
- Choi, S., Theys, N., Salawitch, R.J., Wales, P.A., Joiner, J., Canty, T.P.,
 Chance, K., Suleiman, R.M., Palm, S.P., Cullather, R.I., Darmenov, A.S.,
 Silva, A.d., Kurosu, T.P., Hendrick, F., Van Roozendael, M., 2018. Link Between
 1275 Arctic Tropospheric BrO Explosion Observed From Space and Sea-Salt
 Aerosols From Blowing Snow Investigated Using Ozone Monitoring Instrument BrO Data and GEOS-5 Data Assimilation System. *J. Geophys. Res. Atmos.* 123, 6954–6983. URL: <https://agupubs.onlinelibrary.wiley.com/doi/abs/10.1029/2017JD026889>, doi:10.1029/2017JD026889.
- Choi, Y., Souri, A.H., 2015a. Chemical condition and surface ozone in
 1280 large cities of Texas during the last decade: Observational evidence from OMI, CAMS, and model analysis. *Rem. Sens. Environ.* 168, 90–101. URL: <http://www.sciencedirect.com/science/article/pii/S0034425715300559>, doi:10.1016/j.rse.2015.06.026.
- Choi, Y., Souri, A.H., 2015b. Seasonal behavior and long-term trends of
 1285 tropospheric ozone, its precursors and chemical conditions over Iran: A view from space. *Atmos. Environ.* 106, 232–240. URL: <http://www.sciencedirect.com/science/article/pii/S1352231015001314>, doi:10.1016/j.atmosenv.2015.02.012.
- Cuesta, J., Eremenko, M., Liu, X., Dufour, G., Cai, Z., Höpfner, M., von Clar-
 1290 mann, T., Sellitto, P., Foret, G., Gaubert, B., Beekmann, M., Orphal, J.,
 Chance, K., Spurr, R., Flaud, J.M., 2013. Satellite observation of lower-most
 tropospheric ozone by multispectral synergism of IASI thermal infrared
 and GOME-2 ultraviolet measurements over Europe. *Atmos. Chem. Phys.*
 1295 13, 9675–9693. URL: <https://www.atmos-chem-phys.net/13/9675/2013/>, doi:10.5194/acp-13-9675-2013.
- Daumont, D., Brion, J., Charbonnier, J., Malicet, J., 1992. Ozone UV spectroscopy I: Absorption cross-sections at room temperature. *J. Atmos. Chem.*

15, 145–155. URL: <https://doi.org/10.1007/BF00053756>, doi:10.1007/BF00053756.

- 1300 de Foy, B., Lu, Z., Streets, D.G., 2016. Impacts of the control strategies, the Great Recession and weekday variations on NO₂ columns above North American cities. *Atmos. Environ.* 138, 74–86. URL: <http://www.sciencedirect.com/science/article/pii/S1352231016303211>, doi:10.1016/j.atmosenv.2016.04.038.
- 1305 de Foy, B., Lu, Z., Streets, D.G., Lamsal, L.N., Duncan, B.N., 2015. Estimates of power plant NO_x emissions and lifetimes from OMI NO₂ satellite retrievals. *Atmos. Environ.* 116, 1–11. URL: <http://www.sciencedirect.com/science/article/pii/S1352231015301291>, doi:10.1016/j.atmosenv.2015.05.056.
- 1310 De Smedt, I., Müller, J.F., Stavrakou, T., van der A, R., Eskes, H., Van Roozendael, M., 2008. Twelve years of global observations of formaldehyde in the troposphere using GOME and SCIAMACHY sensors. *Atmos. Chem. Phys.* 8, 4947–4963. URL: <https://www.atmos-chem-phys.net/8/4947/2008/>, doi:10.5194/acp-8-4947-2008.
- 1315 De Smedt, I., Stavrakou, T., Hendrick, F., Danckaert, T., Vlemmix, T., Pinardi, G., Theys, N., Lerot, C., Gielen, C., Vigouroux, C., Hermans, C., Fayt, C., Veefkind, P., Müller, J.F., Van Roozendael, M., 2015. Diurnal, seasonal and long-term variations of global formaldehyde columns inferred from combined OMI and GOME-2 observations. *Atmos. Chem. Phys.* 15, 12519–12545. URL: <https://www.atmos-chem-phys.net/15/12519/2015/>, doi:10.5194/acp-15-12519-2015.
- 1320 De Smedt, I., Stavrakou, T., Müller, J.F., van der A, R.J., Van Roozendael, M., 2010. Trend detection in satellite observations of formaldehyde tropospheric columns. *Geophys. Res. Lett.* 37. URL: <https://agupubs.onlinelibrary.wiley.com/doi/abs/10.1029/2010GL044245>, doi:10.1029/2010GL044245.

De Smedt, I., Theys, N., Yu, H., Danckaert, T., Lerot, C., Compernolle, S., Van Roozendael, M., Richter, A., Hilboll, A., Peters, E., Pedergnana, M., Loyola, D., Beirle, S., Wagner, T., Eskes, H., van Geffen, J., Boersma, K.F., Veefkind, P., 2018. Algorithm theoretical baseline for formaldehyde retrievals

1330

from S5p TROPOMI and from the QA4ECV project. *Atmos. Meas. Tech.* 11, 2395–2426. URL: <https://www.atmos-meas-tech.net/11/2395/2018/>, doi:10.5194/amt-11-2395-2018.

De Smedt, I., Van Roozendael, M., Stavrakou, T., Müller, J.F., Lerot, C., Theys, N., Valks, P., Hao, N., van der A, R., 2012. Improved retrieval of

1335

global tropospheric formaldehyde columns from GOME-2/MetOp-A addressing noise reduction and instrumental degradation issues. *Atmos. Meas. Tech.* 5, 2933–2949. URL: <https://www.atmos-meas-tech.net/5/2933/2012/>, doi:10.5194/amt-5-2933-2012.

DeLand, M.T., Cebula, R.P., 1998. NOAA 11 Solar Backscatter Ultraviolet, model 2 (SBUV/2) instrument solar spectral irradiance measurements

1340

in 1989–1994: 2. Results, validation, and comparisons. *J. Geophys. Res. Atmos.* 103, 16251–16273. URL: <https://agupubs.onlinelibrary.wiley.com/doi/abs/10.1029/98JD01204>, doi:10.1029/98JD01204.

Dirksen, R.J., Sommer, M., Immel, F.J., Hurst, D.F., Kivi, R., Vömel,

1345

H., 2014. Reference quality upper-air measurements: GRUAN data processing for the Vaisala RS92 radiosonde. *Atmos. Meas. Tech.* 7, 4463–4490. URL: <https://www.atmos-meas-tech.net/7/4463/2014/>, doi:10.5194/amt-7-4463-2014.

Dobrolenskiy, Y., Dziuban, I., Ivanov, Y., Syniavskyi, I., Ionov, D., Poberovsky,

1350

A., Koralev, O., Fedorova, A., Vyazovetskiy, N., 2018. Optical design of imaging spectrometer for atmosphere monitoring from near-Earth orbit, in: *Optical Design and Engineering VII*, SPIE. pp. 10690 – 10690 – 8. URL: <https://doi.org/10.1117/12.2312021>, doi:10.1117/12.2312021.

Dobrolenskiy, Y.S., Ionov, D.V., Koralev, O.I., Fedorova, A.A., Zherebtsov,

- 1355 E.A., Shatalov, A.E., Mantsevich, S.N., Belyaev, D.A., Vyazovetskiy, N.A.,
 Moiseev, P.P., Tchikov, K.N., Krasavtsev, V.M., Savushkin, A.V., Rumyantsev,
 D.M., Kananykhin, I.V., Viktorov, A.I., Kozyura, A.V., Moryakin, S.A.,
 Poberovskii, A.V., 2015. Development of a space-borne spectrometer to monitor
 atmospheric ozone. *Appl. Opt.* 54. URL: <https://www.osapublishing.org/ao/abstract.cfm?uri=ao-54-11-3315>, doi:10.1364/AO.54.003315.
- 1360 Dobson, G.M.B., 1931. A photoelectric spectrophotometer for measuring the amount of atmospheric ozone. *Proc. Phys. Soc.* 43, 324–339.
 URL: <https://doi.org/10.1088%2F0959-5309%2F43%2F3%2F308>, doi:10.1088/0959-5309/43/3/308.
- 1365 Duncan, B.N., Lamsal, L.N., Thompson, A.M., Yoshida, Y., Lu, Z., Streets,
 D.G., Hurwitz, M.M., Pickering, K.E., 2016. A space-based, high-resolution view of notable changes in urban NO_x pollution around the world (2005–2014). *J. Geophys. Res.* 121, 976–996. URL: <https://agupubs.onlinelibrary.wiley.com/doi/abs/10.1002/2015JD024121>, doi:10.1002/2015JD024121.
- 1370 Duncan, B.N., Prados, A.I., Lamsal, L.N., Liu, Y., Streets, D.G., Gupta, P.,
 Hilsenrath, E., Kahn, R.A., Nielsen, J.E., Beyersdorf, A.J., Burton, S.P.,
 Fiore, A.M., Fishman, J., Henze, D.K., Hostetler, C.A., Krotkov, N.A., Lee,
 P., Lin, M., Pawson, S., Pfister, G., Pickering, K.E., Pierce, R.B., Yoshida,
 Y., Ziembka, L.D., 2014. Satellite data of atmospheric pollution for U.S. air
 1375 quality applications: Examples of applications, summary of data end-user resources, answers to FAQs, and common mistakes to avoid. *Atmos. Environ.* 94, 647 – 662. URL: <http://www.sciencedirect.com/science/article/pii/S1352231014004270>, doi:10.1016/j.atmosenv.2014.05.061.
- Duncan, B.N., Yoshida, Y., de Foy, B., Lamsal, L.N., Streets, D., Lu,
 Z., Pickering, K.E., Krotkov, N.A., 2013. The observed response of the Ozone Monitoring Instrument (OMI) NO₂ column to NO_x emission controls on power plants in the United States: 2005–2011. *Atmos. Environ.* 81,
- 1380

- 102–111. URL: <http://www.sciencedirect.com/science/article/pii/S1352231013006894>, doi:10.1016/j.atmosenv.2013.08.068.
- 1385 Earth Observation Portal, . Satellite Missions Directory - Earth Observation Missions - eoPortal. URL: <https://directory.eoportal.org/web/eoportal/satellite-missions>.
- 1390 Efremenko, D.S., Loyola R., D.G., Hedelt, P., Spurr, R.J.D., 2017. Volcanic SO₂ plume height retrieval from UV sensors using a full-physics inverse learning machine algorithm. Int. J. Remote Sen. 38, 1–27. URL: <https://www.tandfonline.com/doi/full/10.1080/01431161.2017.1348644>, doi:10.1080/01431161.2017.1348644.
- Eisinger, M., Burrows, J.P., 1998. Tropospheric sulfur dioxide observed by the ERS-2 GOME instrument. Geophys. Res. Lett. 25, 4177–4180. URL: <http://doi.wiley.com/10.1029/1998GL900128>, doi:10.1029/1998GL900128.
- 1395 EPA, 2008. Integrated Science Assessment for Oxides of Nitrogen - Health Criteria (First External Review Draft). Technical Report. U.S. Environmental Protection Agency, Research Triangle Park, NC 27711. EPA/600/R-07/093.
- 1400 ESA, 1995. Global Ozone Monitoring Experiment GOME Users Manual. URL: <https://earth.esa.int/documents/10174/1596664/GOME05.pdf>.
- Fabry, C., Buisson, H., 1913. L'absorption de l'ultra-violet par l'ozone et la limite du spectre solaire. J. Phys. Theor. Appl. 3, 196–206. URL: <https://hal.archives-ouvertes.fr/jpa-00241833>, doi:10.1051/jphysap:019130030019601.
- 1405 Fabry, C., Buisson, H., 1921. Étude de l'extrême ultra-violette du spectre solaire. J. Phys. Radium 2, 197–226. URL: <https://hal.archives-ouvertes.fr/jpa-00204283>, doi:10.1051/jphysrad:0192100207019700.
- Fedkin, N.M., Li, C., Dickerson, R.R., Carty, T., Krotkov, N.A., 2019. Linking improvements in sulfur dioxide emissions to decreasing sulfate

- 1410 wet deposition by combining satellite and surface observations with trajectory analysis. *Atmos. Environ.* 199, 210–223. URL: <https://www.sciencedirect.com/science/article/pii/S1352231018308197>, doi:10.1016/J.ATMOSENV.2018.11.039.
- 1415 Fioletov, V.E., McLinden, C.A., Krotkov, N., Li, C., 2015. Lifetimes and emissions of SO₂ from point sources estimated from OMI. *Geophys. Res. Lett.* 42, 1969–1976. URL: <http://doi.wiley.com/10.1002/2015GL063148>, doi:10.1002/2015GL063148.
- 1420 Fioletov, V.E., McLinden, C.A., Krotkov, N., Li, C., Joiner, J., Theys, N., Carn, S., Moran, M.D., 2016. A global catalogue of large SO₂ emissions derived from the Ozone Monitoring Instrument. *Atmos. Chem. Phys.* 16, 11497–11519. URL: <https://www.atmos-chem-phys.net/16/11497/2016/>, doi:10.5194/acp-16-11497-2016.
- 1425 Fioletov, V.E., McLinden, C.A., Krotkov, N., Moran, M.D., Yang, K., 2011. Estimation of SO₂ emissions using OMI retrievals. *Geophys. Res. Lett.* 38, L21811. URL: <http://doi.wiley.com/10.1029/2011GL049402>, doi:10.1029/2011GL049402.
- 1430 Fioletov, V.E., McLinden, C.a., Krotkov, N., Yang, K., Loyola, D.G., Valks, P., Theys, N., Van Roozendael, M., Nowlan, C.R., Chance, K., Liu, X., Lee, C., Martin, R.V., 2013. Application of OMI, SCIAMACHY, and GOME-2 satellite SO₂ retrievals for detection of large emission sources. *J. Geophys. Res. Atmos.* 118, 11,399–11,418. URL: <http://doi.wiley.com/10.1002/jgrd.50826>, doi:10.1002/jgrd.50826.
- 1435 Fishman, J., Bowman, K.W., Burrows, J.P., Richter, A., Chance, K.V., Edwards, D.P., Martin, R.V., Morris, G.A., Pierce, R.B., Ziemke, J.R., Al-Saadi, J.A., Creilson, J.K., Schaack, T.K., Thompson, A.M., 2008. Remote Sensing of Tropospheric Pollution from Space. *Bull. Amer. Meteor. Soc.* 89, 805–822. URL: <https://journals.ametsoc.org/doi/10.1175/2008BAMS2526.1>.

Fishman, J., Watson, C.E., Larsen, J.C., Logan, J.A., 1990. Distribution of tropospheric ozone determined from satellite data. *J. Geophys. Res. Atmos.* 95, 3599–3617. URL: <https://agupubs.onlinelibrary.wiley.com/doi/abs/10.1029/JD095iD04p03599>, doi:10.1029/JD095iD04p03599.

Fleig, J., McPeters, R.D., Taylor, L., 1990. Nimbus 7 solar backscatter ultraviolet (SBUV) spectral scans solar irradiance and Earth radiance product user's guide. NASA Reference Publication 1234 , 130 URL: <https://ntrs.nasa.gov/archive/nasa/casi.ntrs.nasa.gov/19900007911.pdf>.

Frederick, S.E., Cebula, R.P., Heath, D.F., 1986. Instrument Characterization for the Detection of Long-term Changes in Stratospheric Ozone: An Analysis of the SBUY/2 Radiometer. *J. Atmos. Oceanic Technol.* 3, 472–480. URL: <https://journals.ametsoc.org/doi/10.1175/1520-0426%281986%29003%3C0472%3AICFTD0%3E2.0.CO%3B2>, doi:10.1175/1520-0426(1986)003<0472:ICFTD0>2.0.CO;2.

Fried, A., Crawford, J., Olson, J., Walega, J., Potter, W., Wert, B., Jordan, C., Anderson, B., Shetter, R., Lefer, B., Blake, D., Blake, N., Meinardi, S., Heikes, B., O'Sullivan, D., Snow, J., Fuelberg, H., Kiley, C.M., Sandholm, S., Tan, D., Sachse, G., Singh, H., Faloona, I., Harward, C.N., Carmichael, G.R., 2003. Airborne tunable diode laser measurements of formaldehyde during TRACE-P: Distributions and box model comparisons. *J. Geophys. Res. Atmos.* 108, URL: <https://agupubs.onlinelibrary.wiley.com/doi/abs/10.1029/2003JD003451>, doi:10.1029/2003JD003451.

Frith, S.M., Kramarova, N.A., Stolarski, R.S., McPeters, R.D., Bhartia, P.K., Labow, G.J., 2014. Recent changes in total column ozone based on the SBUV Version 8.6 Merged Ozone Data Set. *J. Geophys. Res. Atmos.* 119, 9735–9751. URL: <https://agupubs.onlinelibrary.wiley.com/doi/abs/10.1002/2014JD021889>, doi:10.1002/2014JD021889.

Fu, D., Kulawik, S.S., Miyazaki, K., Bowman, K.W., Worden, J.R., Eldering, A., Livesey, N.J., Teixeira, J., Irion, F.W., Herman, R.L., Osterman, G.B.,

- Liu, X., Levelt, P.F., Thompson, A.M., Luo, M., 2018. Retrievals of tropospheric ozone profiles from the synergism of AIRS and OMI: methodology and validation. *Atmos. Meas. Tech.* 11, 5587–5605. URL: <https://www.atmos-meas-tech.net/11/5587/2018/>, doi:10.5194/amt-11-5587-2018.
 1470
- Fu, D., Worden, J.R., Liu, X., Kulawik, S.S., Bowman, K.W., Natraj, V., 2013. Characterization of ozone profiles derived from Aura TES and OMI radiances. *Atmos. Chem. Phys.* 13, 3445–3462. URL: <https://www.atmos-chem-phys.net/13/3445/2013/>, doi:10.5194/acp-13-3445-2013.
 1475
- Gleason, J.F., Bhartia, P.K., Herman, J.R., McPeters, R., Newman, P., Stolarski, R.S., Flynn, L., Labow, G., Larko, D., Seftor, C., Wellemeyer, C., Komhyr, W.D., Miller, A.J., Planet, W., 1993. Record Low Global Ozone in 1992. *Science* 260, 523–526. URL: <http://science.sciencemag.org/content/260/5107/523>, doi:10.1126/science.260.5107.523.
 1480
- Goldman, S., 1953. Information theory. Prentice-Hall.,
 1485
- González Abad, G., Liu, X., Chance, K., Wang, H., Kurosu, T.P., Suleiman, R., 2015. Updated Smithsonian Astrophysical Observatory Ozone Monitoring Instrument (SAO OMI) formaldehyde retrieval. *Atmos. Meas. Tech.* 8, 19–32. URL: <https://www.atmos-meas-tech.net/8/19/2015/>, doi:10.5194/amt-8-19-2015.
- González Abad, G., Liu, X., Suleiman, R.M., Saiz-Lopez, A., Chance, K., 2017. SAO OMPS bromine monoxide retrievals, in: AGU Fall Meeting Abstracts.
 1490
- González Abad, G., Vasilkov, A., Seftor, C., Liu, X., Chance, K., 2016. Smithsonian Astrophysical Observatory Ozone Mapping and Profiler Suite (SAO OMPS) formaldehyde retrieval. *Atmos. Meas. Tech.* 9, 2797–2812. URL: <https://www.atmos-meas-tech.net/9/2797/2016/>, doi:10.5194/amt-9-2797-2016.
- Gordon, I.E., Rothman, L.S., Hill, C., Kochanov, R.V., Tan, Y., Bernath, P.F., Birk, M., Boudon, V., Campargue, A., Chance, K.V., Drouin, B.J.,
 1495

- Flaud, J.M., Gamache, R.R., Hodges, J.T., Jacquemart, D., Perevalov, V.I., Perrin, A., Shine, K.P., Smith, M.A.H., Tennyson, J., Toon, G.C., Tran, H., Tyuterev, V.G., Barbe, A., Császár, A.G., Devi, V.M., Furtenbacher, T., Harrison, J.J., Hartmann, J.M., Jolly, A., Johnson, T.J., Karman, T., Kleiner, I., Kyuberis, A.A., Loos, J., Lyulin, O.M., Massie, S.T., Mikhailyko, S.N., Moazzen-Ahmadi, N., Müller, H.S.P., Naumenko, O.V., Nikitin, A.V., Polyansky, O.L., Rey, M., Rotger, M., Sharpe, S.W., Sung, K., Starikova, E., Tashkum, S.A., Auwera, J.V., Wagner, G., Wilzewski, J., Wcislo, P., Yu, S., Zak, E.J., 2017. The HITRAN2016 molecular spectroscopic database. *J. Quant. Spectrosc. Radiat. Transf.* 203, 3–69. URL: <http://www.sciencedirect.com/science/article/pii/S0022407317301073>, doi:10.1016/j.jqsrt.2017.06.038.
- Gorshelev, V., Serdyuchenko, A., Weber, M., Chehade, W., Burrows, J.P., 2014. High spectral resolution ozone absorption cross-sections – part 1: Measurements, data analysis and comparison with previous measurements around 293 k. *Atmos. Meas. Tech.* 7, 609–624. URL: <https://www.atmos-meas-tech.net/7/609/2014/>, doi:10.5194/amt-7-609-2014.
- Götz, F.W.P., Meetham, A.R., Dobson, G.M.B., 1934. The Vertical Distribution of Ozone in the Atmosphere. *Proc. R. Soc. A, Containing Papers of a Mathematical and Physical Character (1905-1934)* 145, 416–446.
- Grainger, J.F., Ring, J., 1962. Anomalous Fraunhofer Line Profiles. *Nature* 193, 762. URL: <https://doi.org/10.1038/193762a0>, doi:10.1038/193762a0.
- Grossi, M., Valks, P., Loyola, D., Aberle, B., Slijkhuis, S., Wagner, T., Beirle, S., Lang, R., 2015. Total column water vapour measurements from GOME-2 MetOp-A and MetOp-B. *Atmos. Meas. Tech.* 8, 1111–1133. URL: <https://www.atmos-meas-tech.net/8/1111/2015/>, doi:10.5194/amt-8-1111-2015.
- Guo, S., Bluth, G.J.S., Rose, W.I., Watson, I.M., Prata, A.J., 2004. Re-evaluation of SO₂ release of the 15 June 1991 Pinatubo eruption using

- 1525 ultraviolet and infrared satellite sensors. *Geochem. Geophys. Geosyst.* 5, Q04001. URL: <http://doi.wiley.com/10.1029/2003GC000654>, doi:10.1029/2003GC000654.
- Hall, L.A., Anderson, G.P., . High-resolution solar spectrum between 2000 and 3100 Å. *J. Geophys. Res. Atmos.* 96, 12927–1530 12931. URL: <https://agupubs.onlinelibrary.wiley.com/doi/abs/10.1029/91JD01111>, doi:10.1029/91JD01111.
- Harder, J.W., Brault, J.W., 1997. Atmospheric measurements of water vapor in the 442-nm region. *J. Geophys. Res. Atmos.* 102, 6245–6252. URL: <https://agupubs.onlinelibrary.wiley.com/doi/abs/10.1029/96JD01730>, doi:10.1029/96JD01730.
- Hasekamp, O.P., Landgraf, J., 2001. Ozone profile retrieval from backscattered ultraviolet radiances: The inverse problem solved by regularization. *J. Geophys. Res. Atmos.* 106, 8077–8088. URL: <https://agupubs.onlinelibrary.wiley.com/doi/abs/10.1029/2000JD900692>, doi:10.1029/2000JD900692.
- 1540 Hausmann, M., Platt, U., 1994. Spectroscopic measurement of bromine oxide and ozone in the high Arctic during Polar Sunrise Experiment 1992. *J. Geophys. Res. Atmos.* 99, 25399–25413. URL: <https://agupubs.onlinelibrary.wiley.com/doi/abs/10.1029/94JD01314>, doi:10.1029/94JD01314.
- 1545 Heath, D.F., Krueger, A.J., Roeder, H.A., Henderson, B.D., 1975. The Solar Backscatter Ultraviolet and Total Ozone Mapping Spectrometer (SBUV/TOMS) for NIMBUS G. *Opt. Engineering* 14, 14 – 14 – 9. URL: <https://doi.org/10.1117/12.7971839>, doi:10.1117/12.7971839.
- Heath, D.F., Mateer, C. L., a.K.A.R., 1973. The Nimbus-4 backscatter ultraviolet (BUV) atmospheric ozone experiment two years operation. Technical Report. NASA Goddard Space Flight Center. URL: <https://ntrs.nasa.gov/search.jsp?R=19730010658>.

Hebestreit, K., Stutz, J., Rosen, D., Matveiv, V., Peleg, M., Luria, M., Platt, U.,
 1555 1999. DOAS Measurements of Tropospheric Bromine Oxide in Mid-Latitudes.
 Science 283, 55–57. URL: <http://science.sciencemag.org/content/283/5398/55>, doi:10.1126/science.283.5398.55.

Hegels, E., Crutzen, P.J., Klüpfel, T., Perner, D., Burrows, J.P., 1998.
 Global distribution of atmospheric bromine-monoxide from GOME on
 Earth Observing Satellite ERS-2. Geophys. Res. Lett. 25, 3127–
 1560 3130. URL: <https://agupubs.onlinelibrary.wiley.com/doi/abs/10.1029/98GL02417>, doi:10.1029/98GL02417.

Herman, J.R., Cede, A., Spinei, E., Mount, G., Tzortziou, M., Abuhasan, N., 2009. NO₂ column amounts from ground-based Pandora and MFDOAS spectrometers using the direct-sun DOAS technique: Inter-comparisons and application to OMI validation. J. Geophys. Res. 114, D13307. URL: <https://agupubs.onlinelibrary.wiley.com/doi/abs/10.1029/2009JD011848>, doi:10.1029/2009JD011848.

Herman, J.R., Newman, P.A., McPeters, R., Krueger, A.J., Bhartia, P.K., Seftor, C.J., Torres, O., Jaross, G., Cebula, R.P., Larko, D., Welle-meyer, C., 1995. Meteor 3/total ozone mapping spectrometer observations of the 1993 ozone hole. J. Geophys. Res. Atmos. 100, 2973–
 1570 2983. URL: <https://agupubs.onlinelibrary.wiley.com/doi/abs/10.1029/94JD02316>, doi:10.1029/94JD02316.

Heue, K.P., Brenninkmeijer, C.A.M., Baker, A.K., Rauthe-Schöch, A., Wal-
 1575 ter, D., Wagner, T., Hörmann, C., Sihler, H., Dix, B., Frieß, U., Platt, U., Martinsson, B.G., van Velthoven, P.F.J., Zahn, A., Ebinghaus, R., 2011. SO₂ and BrO observation in the plume of the Eyjafjallajökull volcano
 2010: CARIBIC and GOME-2 retrievals. Atmos. Chem. Phys. 11, 2973–
 2989. URL: <https://www.atmos-chem-phys.net/11/2973/2011/>, doi:10.5194/acp-11-2973-2011.

Hewson, W., Barkley, M.P., González Abad, G., Bösch, H., Kurosu, T., Spurr,

- R., Tilstra, L.G., 2015. Development and characterisation of a state-of-the-art GOME-2 formaldehyde air-mass factor algorithm. *Atmos. Meas. Tech.* 8, 4055–4074. URL: <https://www.atmos-meas-tech.net/8/4055/2015/>, doi:10.5194/amt-8-4055-2015.
- 1585
- Ho, S.P., Peng, L., Mears, C., Anthes, R.A., 2018. Comparison of global observations and trends of total precipitable water derived from microwave radiometers and COSMIC radio occultation from 2006 to 2013. *Atmos. Chem. Phys.* 18, 259–274. URL: <https://www.atmos-chem-phys.net/18/259/2018/>, doi:10.5194/acp-18-259-2018.
- 1590
- Holben, B.N., Eck, T.F., Slutsker, I., Tanré, D., Buis, J.P., Setzer, A., Vermote, E., Reagan, J.A., Kaufman, Y.J., Nakajima, T., Lavenu, F., Jankowiak, I., Smirnov, A., 1998. AERONET—A Federated Instrument Network and Data Archive for Aerosol Characterization. *Rem. Sens. Environ.* 66, 1–16. URL: <http://www.sciencedirect.com/science/article/pii/S0034425798000315>, doi:10.1016/S0034-4257(98)00031-5.
- 1595
- Hoogen, R., Rozanov, V.V., Burrows, J.P., 1999. Ozone profiles from GOME satellite data: Algorithm description and first validation. *J. Geophys. Res. Atmos.* 104, 8263–8280. URL: <https://agupubs.onlinelibrary.wiley.com/doi/abs/10.1029/1998JD100093>, doi:10.1029/1998JD100093.
- 1600
- Hörmann, C., Sihler, H., Beirle, S., Penning de Vries, M., Platt, U., Wagner, T., 2016. Seasonal variation of tropospheric bromine monoxide over the Rann of Kutch salt marsh seen from space. *Atmos. Chem. Phys.* 16, 13015–13034. URL: <https://www.atmos-chem-phys.net/16/13015/2016/>, doi:10.5194/acp-16-13015-2016.
- 1605
- Hörmann, C., Sihler, H., Bobrowski, N., Beirle, S., Penning de Vries, M., Platt, U., Wagner, T., 2013. Systematic investigation of bromine monoxide in volcanic plumes from space by using the GOME-2 instrument. *Atmos. Chem. Phys.* 13, 4749–4781. URL: <https://www.atmos-chem-phys.net/13/4749/2013/>, doi:10.5194/acp-13-4749-2013.
- 1610

- Huang, F., Huang, Y., Flynn, L.E., Wang, W., Cao, D., Wang, S., 2012. Radiometric Calibration of the Solar Backscatter Ultraviolet Sounder and Validation of Ozone Profile Retrievals. *IEEE Trans. Geo. Rem. Sens.* 50, 4956–4964. doi:10.1109/TGRS.2012.2211368.
- ¹⁶¹⁵ Hudman, R.C., Moore, N.E., Martin, R.V., Russell, A.R., Mebust, A.K., Valin, L.C., Cohen, R.C., 2012. A mechanistic model of global soil nitric oxide emissions: implementation and space based constraints. *Atmos. Chem. Phys.* 12, 7779–7795. URL: <https://www.atmos-chem-phys.net/12/7779/2012/>, doi:10.5194/acp-12-7779-2012.
- ¹⁶²⁰ Ingmann, P., Veihelmann, B., Langen, J., Lamarre, D., Stark, H., Courrèges-Lacoste, G.B., 2012. Requirements for the GMES atmosphere service and ESA's implementation concept: Sentinels-4/-5 and -5p. *Rem. Sens. Environ.* 120, 58–69. URL: <http://www.sciencedirect.com/science/article/pii/S0034425712000673>, doi:10.1016/j.rse.2012.01.023.
- ¹⁶²⁵ Iozenas, V., 1968. Determination of the vertical ozone distribution in the upper layers of the atmosphere from satellite measurements of ultraviolet solar radiation scattered by the earth's atmosphere. *Geomagn. Aeron.* 8, 403–410.
- ¹⁶³⁰ Irie, H., Kanaya, Y., Akimoto, H., Iwabuchi, H., Shimizu, A., Aoki, K., 2008. First retrieval of tropospheric aerosol profiles using MAX-DOAS and comparison with lidar and sky radiometer measurements. *Atmos. Chem. Phys.* 8, 341–350. URL: <https://www.atmos-chem-phys.net/8/341/2008/acp-8-341-2008.html>, doi:10.5194/acp-8-341-2008.
- ¹⁶³⁵ Jin, X., Fiore, A.M., Murray, L.T., Valin, L.C., Lamsal, L.N., Duncan, B., Boersma, K.F., De Smedt, I., González Abad, G., Chance, K., Tonnesen, G.S., 2017. Evaluating a Space-Based Indicator of Surface Ozone-NOx-VOC Sensitivity Over Midlatitude Source Regions and Application to Decadal Trends. *J. Geophys. Res. Atmos.* 122, 10,439–10,461. URL: <https://agupubs.onlinelibrary.wiley.com/doi/abs/10.1002/2017JD026720>, doi:10.1002/2017JD026720.

- 1640 Jin, X., Holloway, T., 2015. Spatial and temporal variability of ozone sensitivity over China observed from the Ozone Monitoring Instrument. *J. Geophys. Res. Atmos.* 120, 7229–7246. URL: <https://agupubs.onlinelibrary.wiley.com/doi/abs/10.1002/2015JD023250>, doi:10.1002/2015JD023250.
- 1645 Joiner, J., Bhartia, P.K., Cebula, R.P., Hilsenrath, E., McPeters, R.D., Park, H., 1995. Rotational Raman scattering (Ring effect) in satellite backscatter ultraviolet measurements. *Appl. Opt.* 34, 4513–4525. URL: <http://ao.osa.org/abstract.cfm?URI=ao-34-21-4513>, doi:10.1364/AO.34.004513.
- 1650 Kaiser, J., Wolfe, G.M., Min, K.E., Brown, S.S., Miller, C.C., Jacob, D.J., deGouw, J.A., Graus, M., Hanisco, T.F., Holloway, J., Peischl, J., Pollack, I.B., Ryerson, T.B., Warneke, C., Washenfelder, R.A., Keutsch, F.N., 2015. Reassessing the ratio of glyoxal to formaldehyde as an indicator of hydrocarbon precursor speciation. *Atmos. Chem. Phys.* 15, 7571–7583. URL: <https://www.atmos-chem-phys.net/15/7571/2015/acp-15-7571-2015.html>, doi:10.5194/acp-15-7571-2015.
- 1655 Kar, J., Fishman, J., Creilson, J.K., Richter, A., Ziemke, J., Chandra, S., 2010. Are there urban signatures in the tropospheric ozone column products derived from satellite measurements? *Atmos. Chem. Phys.* 10, 5213–5222. URL: <https://www.atmos-chem-phys.net/10/5213/2010/>, doi:10.5194/acp-10-5213-2010.
- 1660 Kim, J., Jeong, U., Ahn, M.H., Kim, J.H.K.e.a., 2018. Geostationary Environment Monitoring Spectrometer (GEMS): Monitoring air quality from GEO in high temporal and spatial resolution over Asia. *Bull. Amer. Meteor. Soc.* submitted.
- 1665 Kim, S.W., Heckel, A., Frost, G.J., Richter, A., Gleason, J., Burrows, J.P., McKeen, S.A., Hsie, E.Y., Granier, C., Trainer, M.K., 2009. NO₂ columns in the western United States observed from space and simulated by a regional chemistry model and their implications for NO_x emissions. *J. Geophys. Res.* 114,

- D11301. URL: <https://agupubs.onlinelibrary.wiley.com/doi/abs/10.1029/2008JD011343>, doi:10.1029/2008JD011343.
- 1670 Koukouli, M.E., Theys, N., Ding, J., Zyrichidou, I., Mijling, B., Balis, D., van der A, R.J., 2018. Updated SO₂ emission estimates over China using OMI/Aura observations. *Atmos. Meas. Tech.* 11, 1817–1832. URL: <https://doi.org/10.5194/amt-11-1817-2018>, doi:10.5194/amt-11-1817-2018.
- 1675 Kramarova, N.A., Frith, S.M., Bhartia, P.K., McPeters, R.D., Taylor, S.L., Fisher, B.L., Labow, G.J., DeLand, M.T., 2013. Validation of ozone monthly zonal mean profiles obtained from the version 8.6 solar backscatter ultraviolet algorithm. *Atmos. Chem. Phys.* 13, 6887–6905. URL: <https://www.atmos-chem-phys.net/13/6887/2013/>, doi:10.5194/acp-13-6887-2013.
- 1680 Krasnopol'skii, V., 1966. Ultraviolet spectrum of the radiation reflected by the earth's atmosphere and its use in determining the total content and vertical distribution of atmospheric ozone (Solar UV reflection and scattering from earth atmosphere, use in determining total concentration and vertical distribution of ozone). *Geomagn. Aeron.* 6, 236–242.
- 1685 Kromminga, H., Orphal, J., Spietz, P., Voigt, S., Burrows, J., 2003. New measurements of OCIO absorption cross-sections in the 325–435 nm region and their temperature dependence between 213 and 293 K. *J. Photochem. Photobiol. A: Chemistry* 157, 149–160. URL: <http://www.sciencedirect.com/science/article/pii/S1010603003000716>, doi:10.1016/S1010-6030(03)00071-6.
- 1690 Kroon, M., de Haan, J.F., Veefkind, J.P., Froidevaux, L., Wang, R., Kivi, R., Hakkila, J.J., 2011. Validation of operational ozone profiles from the Ozone Monitoring Instrument. *J. Geophys. Res. Atmos.* 116. URL: <https://agupubs.onlinelibrary.wiley.com/doi/abs/10.1029/2010JD015100>, doi:10.1029/2010JD015100.
- 1695 Krotkov, N., Carn, S., Krueger, A., Bhartia, P., Yang, K., 2006. Band residual difference algorithm for retrieval of SO₂ from the aura ozone

monitoring instrument (OMI). IEEE Trans. Geo. Rem. Sens. 44, 1259–1266. URL: http://ieeexplore.ieee.org/xpls/abs_all.jsp?arnumber=1624604, doi:10.1109/TGRS.2005.861932.

¹⁷⁰⁰ Krotkov, N., Habib, S., da Silva, A., Hughes, E., Yang, K., Brentzel, K., Seftor, C., Schneider, D., Guffanti, M., Hoffman, R.L., Myers, T., Tamminen, J., Hassinen, S., 2014. Real Time Volcanic Cloud Products and Predictions for Aviation Alerts, in: 6th AIAA Atmospheric and Space Environments Conference, American Institute of Aeronautics and Astronautics. URL: <http://arc.aiaa.org/doi/10.2514/6.2014-2618>, doi:10.2514/6.2014-2618.

Krotkov, N.A., McLinden, C.A., Li, C., Lamsal, L.N., Celarier, E.A., Marchenko, S.V., Swartz, W.H., Bucsela, E.J., Joiner, J., Duncan, B.N., Folkert Boersma, K., Pepijn Veefkind, J., Levelt, P.F., Fioletov, V.E., Dickerson, R.R., He, H., Lu, Z., Streets, D.G., 2016. Aura OMI observations of regional SO₂ and NO₂ pollution changes from 2005 to 2015. Atmos. Chem. Phys. 16, 4605–4629. URL: <https://www.atmos-chem-phys.net/16/4605/2016/>, doi:10.5194/acp-16-4605-2016.

¹⁷¹⁰ Krueger, A., 1983. Sighting of El Chichón Sulfur Dioxide Clouds with the Nimbus 7 Total Ozone Mapping Spectrometer. Science 220, 1377–1379. URL: <http://science.sciencemag.org/content/220/4604/1377>, doi:10.1126/science.220.4604.1377.

¹⁷²⁰ Krueger, A.J., Heath, D.F., Mateer, C.L., 1973. Variations in the stratospheric ozone field inferred from Nimbus satellite observations. Pure Appl. Geophys. 106, 1254–1263. URL: <https://doi.org/10.1007/BF00881077>, doi:10.1007/BF00881077.

¹⁷²⁰ Krueger, A.J., Schaefer, S.J., Krotkov, N., Bluth, G., Barker, S., 2013. Ultraviolet Remote Sensing of Volcanic Emissions. American Geophysical Union (AGU). pp. 25–43. URL: <https://agupubs.onlinelibrary.wiley.com/doi/abs/10.1029/GM116p0025>, doi:10.1029/GM116p0025.

- 1725 Kuhn, J., Platt, U., Bobrowski, N., Wagner, T., 2019. Towards imaging of atmospheric trace gases using fabry-pérot interferometer correlation spectroscopy in the uv and visible spectral range. *Atmos. Meas. Tech.* 12, 735–747. URL: <https://www.atmos-meas-tech.net/12/735/2019/>, doi:10.5194/amt-12-735-2019.
- 1730 Kurosu, T.P., Chance, K., Sioris, C.E., 2004. Preliminary results for HCHO and BrO from the EOS-Aura Ozone Monitoring Instrument, in: Passive Optical Remote Sensing of the Atmosphere and Clouds IV, SPIE. pp. 116–124. URL: <https://www.spiedigitallibrary.org/conference-proceedings-of-spie/5652/0000/Preliminary-results-for-HCHO-and-BrO-from-the-EOS-Aura/> 10.1117/12.578606.short, doi:10.1117/12.578606.
- Kurtz, M.J., Mink, D.J., Wyatt, W.F., Fabricant, D.G., Torres, G., Kriss, G.A., Tonry, J.L., 1992. XCSAO: A Radial Velocity Package for the IRAF Environment, in: Worrall, D.M., Biemesderfer, C., Barnes, J. (Eds.), Astronomical Data Analysis Software and Systems I, ASP Conf. Ser., pp. 432–438. 1740
- Kurucz, R.L., Furenlid, I., Brault, J., Testerman, L., 1984. Solar flux atlas from 296 to 1300 nm, National Solar Observatory Atlas, Sunspot, New Mexico: National Solar Observatory.
- 1745 Labow, G.J., McPeters, R.D., Bhartia, P.K., Kramarova, N., 2013. A comparison of 40 years of sbuv measurements of column ozone with data from the dobson/brewer network. *J. Geophys. Res. Atmos.* 118, 7370–7378. URL: <https://agupubs.onlinelibrary.wiley.com/doi/abs/10.1002/jgrd.50503>, doi:10.1002/jgrd.50503.
- Lamsal, L.N., Duncan, B.N., Yoshida, Y., Krotkov, N.A., Pickering, K.E., Streets, D.G., Lu, Z., 2015. U.S. NO₂ trends: EPA Air Quality System (AQS) data versus improved observations from the Ozone Monitoring Instrument (OMI). *Atmos. Environ.* 110, 130–143. URL: <http://www>. 1750

[sciencedirect.com/science/article/pii/S1352231015002794](https://doi.org/10.1016/j.atmosenv.2015.03.055), doi:10.1016/j.atmosenv.2015.03.055.

- 1755 Lamsal, L.N., Martin, R.V., van Donkelaar, A., Celarier, E.A., Bucsela, E.J., Boersma, K.F., Luo, R.D.C., Wang, Y., 2010. Indirect validation of tropospheric nitrogen dioxide retrieved from the OMI satellite instrument: Insight into the seasonal variation of nitrogen oxides at northern midlatitudes. *J. Geophys. Res.* 115, D05302. URL: <https://agupubs.onlinelibrary.wiley.com/doi/abs/10.1029/2009JD013351>, doi:10.1029/2009JD013351.
- Lang, R., Casadio, S., Maurellis, A.N., Lawrence, M.G., 2007. Evaluation of the GOME Water Vapor Climatology 1995–2002. *J. Geophys. Res. Atmos.* 112. URL: <https://agupubs.onlinelibrary.wiley.com/doi/abs/10.1029/2006JD008246>, doi:10.1029/2006JD008246.
- 1760 Langley, S.P., 1881. The bolometer and radiant energy. Cambridge.
- Langley, S.P., Abbot, C.G., 1900. Annals of the Astrophysical Observatory of the Smithsonian Institution. URL: <http://hdl.handle.net/2027/uva.x002221386>.
- Lee, C., Martin, R.V., van Donkelaar, A., Lee, H., Dickerson, R.R., Hains, J.C., Krotkov, N., Richter, A., Vinnikov, K., Schwab, J.J., 2011. SO₂ emissions and lifetimes: Estimates from inverse modeling using in situ and global, space-based (SCIAMACHY and OMI) observations. *J. Geophys. Res.* 116, D06304. URL: <https://agupubs.onlinelibrary.wiley.com/doi/full/10.1029/2010JD014758>, doi:10.1029/2010JD014758.
- 1775 Lee, C., Richter, A., Weber, M., Burrows, J.P., 2008. SO₂ Retrieval from SCIAMACHY using the Weighting Function DOAS (WFDOAS) technique: comparison with Standard DOAS retrieval. *Atmos. Chem. Phys.* 8, 6137–6145. URL: <https://doi.org/10.5194/acp-8-6137-2008>, doi:10.5194/acp-8-6137-2008.

¹⁷⁸⁰ Lelieveld, J., Dentener, F.J., 2000. What controls tropospheric ozone? *J. Geophys. Res. Atmos.* 105, 3531–3551. URL: <https://agupubs.onlinelibrary.wiley.com/doi/abs/10.1029/1999JD901011>, doi:10.1029/1999JD901011.

¹⁷⁸⁵ Lerot, C., Stavrakou, T., De Smedt, I., Müller, J.F., Van Roozendael, M., 2010. Glyoxal vertical columns from GOME-2 backscattered light measurements and comparisons with a global model. *Atmos. Chem. Phys.* 10, 12059–12072. URL: <https://www.atmos-chem-phys.net/10/12059/2010/>, doi:10.5194/acp-10-12059-2010.

¹⁷⁹⁰ Levelt, P.F., Joiner, J., Tamminen, J., Veefkind, J.P., Bhartia, P.K., Stein Zweers, D.C., Duncan, B.N., Streets, D.G., Eskes, H., van der A, R., McLinden, C., Fioletov, V., Carn, S., de Laat, J., DeLand, M., Marchenko, S., McPeters, R., Ziemke, J., Fu, D., Liu, X., Pickering, K., Apituley, A., González Abad, G., Arola, A., Boersma, F., Chan Miller, C., Chance, K., de Graaf, M., Hakkarainen, J., Hassinen, S., Ialongo, I., Kleipool, Q., Krotkov, N., Li, C., Lamsal, L., Newman, P., Nowlan, C., Suleiman, R., Tilstra, L.G., Torres, O., Wang, H., Wargan, K., 2018. The Ozone Monitoring Instrument: overview of 14 years in space. *Atmos. Chem. Phys.* 18, 5699–5745. URL: <https://www.atmos-chem-phys.net/18/5699/2018/>, doi:10.5194/acp-18-5699-2018.

¹⁸⁰⁰ Levelt, P.F., van der Oord, G.H.J., Dobber, M.R., Malkki, A., Visser, H., de Vries, J., Stammes, P., Lundell, J.O.V., Saari, H., 2006. The ozone monitoring instrument. *IEEE Trans. Geo. Rem. Sens.* 44, 1093–1101. doi:10.1109/TGRS.2006.872333.

¹⁸⁰⁵ Li, C., Joiner, J., Krotkov, N.A., Bhartia, P.K., 2013. A fast and sensitive new satellite SO₂ retrieval algorithm based on principal component analysis: Application to the ozone monitoring instrument. *Geophys. Res. Lett.* 40, 6314–6318. URL: <http://doi.wiley.com/10.1002/2013GL058134>, doi:10.1002/2013GL058134.

Li, C., Joiner, J., Krotkov, N.A., Dunlap, L., 2015. A new method for

- global retrievals of HCHO total columns from the Suomi National Polar-orbiting Partnership Ozone Mapping and Profiler Suite. *Geophys. Res. Lett.* 42, 2015GL063204. URL: <http://onlinelibrary.wiley.com/doi/10.1002/2015GL063204/abstract>, doi:10.1002/2015GL063204.
- Li, C., Krotkov, N.A., Carn, S., Zhang, Y., Spurr, R.J.D., Joiner, J., 2017a. New-generation NASA Aura Ozone Monitoring Instrument (OMI) volcanic SO₂ dataset: algorithm description, initial results, and continuation with the Suomi-NPP Ozone Mapping and Profiler Suite (OMPS). *Atmos. Meas. Tech.* 10, 445–458. URL: <https://www.atmos-meas-tech.net/10/445/2017/>, doi:10.5194/amt-10-445-2017.
- Li, C., McLinden, C., Fioletov, V., Krotkov, N., Carn, S., Joiner, J., Streets, D., He, H., Ren, X., Li, Z., Dickerson, R.R., 2017b. India Is Overtaking China as the World's Largest Emitter of Anthropogenic Sulfur Dioxide. *Sci. Rep.* 7, 14304. URL: <http://www.nature.com/articles/s41598-017-14639-8>, doi:10.1038/s41598-017-14639-8.
- Li, C., Zhang, Q., Krotkov, N.a., Streets, D.G., He, K., Tsay, S.C., Gleason, J.F., 2010. Recent large reduction in sulfur dioxide emissions from Chinese power plants observed by the Ozone Monitoring Instrument. *Geophys. Res. Lett.* 37, L08807. URL: <http://doi.wiley.com/10.1029/2010GL042594>, doi:10.1029/2010GL042594.
- Liu, F., Choi, S., Li, C., Fioletov, V.E., McLinden, C.A., Joiner, J., Krotkov, N.A., Bian, H., Janssens-Maenhout, G., Darmenov, A.S., da Silva, A.M., 2018. A new global anthropogenic SO₂ emission inventory for the last decade: a mosaic of satellite-derived and bottom-up emissions. *Atmos. Chem. Phys.* 18, 16571–16586. URL: <https://www.atmos-chem-phys.net/18/16571/2018/>, doi:10.5194/acp-18-16571-2018.
- Liu, X., Bhartia, P.K., Chance, K., Spurr, R.J.D., Kurosu, T.P., 2010. Ozone profile retrievals from the ozone monitoring instrument. *Atmos. Chem. Phys.*

10, 2521–2537. URL: <https://www.atmos-chem-phys.net/10/2521/2010/>, doi:10.5194/acp-10-2521-2010.

- 1840 Liu, X., Chance, K., Sioris, C.E., Spurr, R.J.D., Kurosu, T.P., Martin, R.V., Newchurch, M.J., 2005. Ozone profile and tropospheric ozone retrievals from the Global Ozone Monitoring Experiment: Algorithm description and validation. *J. Geophys. Res.* 110, D20307. URL: <http://onlinelibrary.wiley.com/doi/10.1029/2005JD006240/abstract>, doi:10.1029/2005JD006240.
- 1845 Liu, Y., Wang, Y., Liu, X., Cai, Z., Chance, K., 2009. Tibetan middle tropospheric ozone minimum in June discovered from GOME observations. *Geophys. Res. Lett.* 36. URL: <https://agupubs.onlinelibrary.wiley.com/doi/abs/10.1029/2008GL037056>, doi:10.1029/2008GL037056.
- 1850 Llewellyn, E.J., Lloyd, N.D., Degenstein, D.A., Gattinger, R.L., Petelina, S.V., Bourassa, A.E., Wiensz, J.T., Ivanov, E.V., McDade, I.C., Solheim, B.H., McConnell, J.C., Haley, C.S., von Savigny, C., Sioris, C.E., McLinden, C.A., Griffioen, E., Kaminski, J., Evans, W.F., Puckrin, E., Strong, K., Wehrle, V., Hum, R.H., Kendall, D.J., Matsushita, J., Murtagh, D.P., Brohede, S., Stegman, J., Witt, G., Barnes, G., Payne, W.F., Pich, L., Smith, K., Warshaw, G., Deslauniers, D.L., Marchand, P., Richardson, E.H., King, R.A., Wevers, I., McCreathe, W., Kyrl, E., Oikarinen, L., Leppelmeier, G.W., Auvinen, H., Mgie, G., Hauchecorne, A., Lefvre, F., de La Ne, J., Ricaud, P., Frisk, U., Sjoberg, F., von Schele, F., Nordh, L., 2004. The OSIRIS instrument on the Odin spacecraft. *Can. J. Phys.* 82, 411–422. URL: <https://doi.org/10.1139/p04-005>, doi:10.1139/p04-005.
- 1860 Lorente, A., Folkert Boersma, K., Yu, H., Dörner, S., Hilboll, A., Richter, A., Liu, M., Lamsal, L.N., Barkley, M., De Smedt, I., Van Roozendael, M., Wang, Y., Wagner, T., Beirle, S., Lin, J.T., Krotkov, N., Stammes, P., Wang, P., Eskes, H.J., Krol, M., 2017. Structural uncertainty in air mass factor calculation for NO₂ and HCHO satellite retrievals. *Atmos. Meas. Tech.*

¹⁸⁶⁵ 10, 759–782. URL: <https://www.atmos-meas-tech.net/10/759/2017/>, doi:10.5194/amt-10-759-2017.

¹⁸⁷⁰ Lu, Z., Streets, D.G., 2012. Increase in NO_x emissions from Indian thermal power plants during 1996–2010: Unit-based inventories and multisatellite observations. Environ. Sci. Technol. 46, 7463–7470. URL: <https://doi.org/10.1021/es300831w>, doi:10.1021/es300831w.

¹⁸⁷⁵ Lu, Z., Streets, D.G., de Foy, B., Lamsal, L.N., Duncan, B.N., Xing, J., 2015. Emissions of nitrogen oxides from US urban areas: estimation from Ozone Monitoring Instrument retrievals for 2005–2014. Atmos. Chem. Phys. 15, 10367–10383. URL: <https://www.atmos-chem-phys.net/15/10367/2015/>, doi:10.5194/acp-15-10367-2015.

¹⁸⁸⁰ Lu, Z., Zhang, Q., Streets, D.G., 2011. Sulfur dioxide and primary carbonaceous aerosol emissions in China and India, 1996–2010. Atmos. Chem. Phys. 11, 9839–9864. URL: <http://www.atmos-chem-phys.net/11/9839/2011/>, doi:10.5194/acp-11-9839-2011.

¹⁸⁸⁵ Malicet, J., Daumont, D., Charbonnier, J., Parisse, C., Chakir, A., Brion, J., 1995. Ozone UV spectroscopy. II. Absorption cross-sections and temperature dependence. J. Atmos. Chem. 21, 263–273. URL: <https://doi.org/10.1007/BF00696758>, doi:10.1007/BF00696758.

¹⁸⁹⁰ Marais, E.A., Jacob, D.J., Kurosu, T.P., Chance, K., Murphy, J.G., Reeves, C., Mills, G., Casadio, S., Millet, D.B., Barkley, M.P., Paulot, F., Mao, J., 2012. Isoprene emissions in Africa inferred from OMI observations of formaldehyde columns. Atmos. Chem. Phys. 12, 6219–6235. URL: <https://www.atmos-chem-phys.net/12/6219/2012/acp-12-6219-2012.html>, doi:10.5194/acp-12-6219-2012.

¹⁸⁹⁵ Marchenko, S., Krotkov, N.A., Lamsal, L.N., Celarier, E.A., Swartz, W.H., Bucsela, E.J., 2015. Revising the slant column density retrieval of nitrogen

- dioxide observed by the ozone monitoring instrument. *J. Geophys. Res. Atmos.* 120, 5670–5692. URL: <https://agupubs.onlinelibrary.wiley.com/doi/abs/10.1002/2014JD022913>, doi:10.1002/2014JD022913.
- ¹⁸⁹⁵ Maresi, L., Van Der Meulen, W., Vink, R., 2014. TROPOLITE, on the path of atmospheric chemistry made simple, in: Sensor, Systems, and Next-Generation Satellites XVIII, pp. 9241–9252. URL: <https://doi.org/10.1117/12.2067473>, doi:10.1117/12.2067473.
- ¹⁹⁰⁰ Marshak, A., Herman, J., Adam, S., Karin, B., Carn, S., Cede, A., Geogdzhayev, I., Huang, D., Huang, L.K., Knyazikhin, Y., Kowalewski, M., Krotkov, N., Lyapustin, A., McPeters, R., Meyer, K.G., Torres, O., Yang, Y., 2018. Earth Observations from DSCOVR EPIC Instrument. *Bull. Amer. Meteor. Soc.* 99, 1829–1850. URL: <https://doi.org/10.1175/BAMS-D-17-0223.1>, doi:10.1175/BAMS-D-17-0223.1.
- ¹⁹⁰⁵ Martin, R.V., 2008. Satellite remote sensing of surface air quality. *Atmos. Environ.* 42, 7823–7843. URL: <http://www.sciencedirect.com/science/article/pii/S1352231008006328>, doi:10.1016/j.atmosenv.2008.07.018.
- ¹⁹¹⁰ Martin, R.V., Chance, K., Jacob, D.J., et al., 2002. An improved retrieval of tropospheric nitrogen dioxide from GOME. *J. Geophys. Res.* 107. URL: <https://agupubs.onlinelibrary.wiley.com/doi/abs/10.1029/2001JD001027>, doi:10.1029/2001JD001027.
- ¹⁹¹⁵ Martn, J.C.G., Spietz, P., Burrows, J.P., 2005. Spectroscopic studies of the I₂/O₃ photochemistry: Part 1: Determination of the absolute absorption cross sections of iodine oxides of atmospheric relevance. *J. Photochem. Photobiol. A: Chemistry* 176, 15–38. URL: <http://www.sciencedirect.com/science/article/pii/S1010603005004661>, doi:10.1016/j.jphotochem.2005.09.024.
- ¹⁹²⁰ McCormick, M.P., Thomason, L.W., Trepte, C.R., 1995. Atmospheric effects of the Mt Pinatubo eruption. *Nature* 373, 399–404. URL: <https://www.nature.com/articles/373399a0>, doi:10.1038/373399a0.

- McLinden, C.A., Fioletov, V., Shephard, M.W., Krotkov, N., Li, C., Martin, R.V., Moran, M.D., Joiner, J., 2016. Space-based detection of missing sulfur dioxide sources of global air pollution. *Nature. Geo.* 9, 496–500. URL: <http://www.nature.com/articles/ngeo2724>, doi:10.1038/ngeo2724.
- ¹⁹²⁵ McPeters, R.D., 1993. The atmospheric SO₂ budget for Pinatubo derived from Noaa-11 SBUV/2 spectral data. *Geophys. Res. Lett.* 20, 1971–1974. URL: <http://doi.wiley.com/10.1029/93GL02360>, doi:10.1029/93GL02360.
- McPeters, R.D., Bhartia, P.K., Haffner, D., Labow, G.J., Flynn, L., 2013. The version 8.6 SBUV ozone data record: An overview. *J. Geophys. Res. Atmos.* 118, 8032–8039. doi:10.1002/jgrd.50597.
- ¹⁹³⁰ McPeters, R.D., Heath, D.F., Schlesinger, B.M., 1984. Satellite observation of SO₂ from El Chichón: Identification and measurement. *Geophys. Res. Lett.* 11, 1203–1206. URL: <http://doi.wiley.com/10.1029/GL011i012p01203>, doi:10.1029/GL011i012p01203.
- ¹⁹³⁵ McPeters, R.D., Labow, G.J., Logan, J.A., 2007. Ozone climatological profiles for satellite retrieval algorithms. *J. Geophys. Res. Atmos.* 112. URL: <https://agupubs.onlinelibrary.wiley.com/doi/abs/10.1029/2005JD006823>, doi:10.1029/2005JD006823.
- ¹⁹⁴⁰ Mears, C.A., Smith, D.K., Ricciardulli, L., Wang, J., Huelsing, H., Wentz, F.J., 2018. Construction and Uncertainty Estimation of a Satellite-Derived Total Precipitable Water Data Record Over the World's Oceans. *Earth Space Sci.* 5, 197–210. URL: <https://agupubs.onlinelibrary.wiley.com/doi/abs/10.1002/2018EA000363>, doi:10.1002/2018EA000363.
- ¹⁹⁴⁵ Mears, C.A., Smith, D.K., Wentz, F.J., 2015a. Estimated errors in retrievals of ocean parameters from SSMIS. *J. Geophys. Res. Atmos.* 120, 5816–5830. URL: <https://agupubs.onlinelibrary.wiley.com/doi/abs/10.1002/2014JD023049>, doi:10.1002/2014JD023049.

Mears, C.A., Wang, J., Smith, D., Wentz, F.J., 2015b. Intercomparison of total precipitable water measurements made by satellite-borne microwave radiometers and ground-based GPS instruments. *J. Geophys. Res. Atmos.* 120, 2492–2504. URL: <https://agupubs.onlinelibrary.wiley.com/doi/abs/10.1002/2014JD022694>, doi:10.1002/2014JD022694.

Meller, R., Moortgat, G.K., 2000. Temperature dependence of the absorption cross sections of formaldehyde between 223 and 323 K in the wavelength range 225–375 nm. *J. Geophys. Res. Atmos.* 105, 7089–7101. URL: <https://agupubs.onlinelibrary.wiley.com/doi/abs/10.1029/1999JD901074>, doi:10.1029/1999JD901074.

Miles, G.M., Siddans, R., Kerridge, B.J., Latter, B.G., Richards, N.A.D., 2015. Tropospheric ozone and ozone profiles retrieved from GOME-2 and their validation. *Atmos. Meas. Tech.* 8, 385–398. URL: <https://www.atmos-meas-tech.net/8/385/2015/>, doi:10.5194/amt-8-385-2015.

Millet, D.B., Jacob, D.J., Boersma, K.F., Fu, T.M., Kurosu, T.P., Chance, K., Heald, C.L., Guenther, A., 2008. Spatial distribution of isoprene emissions from North America derived from formaldehyde column measurements by the OMI satellite sensor. *J. Geophys. Res. Atmos.* 113. URL: <https://agupubs.onlinelibrary.wiley.com/doi/abs/10.1029/2007JD008950>, doi:10.1029/2007JD008950.

Millet, D.B., Jacob, D.J., Turquety, S., Hudman, R.C., Wu, S., Fried, A., Walega, J., Heikes, B.G., Blake, D.R., Singh, H.B., Anderson, B.E., Clarke, A.D., 2006. Formaldehyde distribution over North America: Implications for satellite retrievals of formaldehyde columns and isoprene emission. *J. Geophys. Res. Atmos.* 111. URL: <https://agupubs.onlinelibrary.wiley.com/doi/abs/10.1029/2005JD006853>, doi:10.1029/2005JD006853.

Müller, M.D., Kaifel, A.K., Weber, M., Tellmann, S., Burrows, J.P., Loyola, D., 2003. Ozone profile retrieval from Global Ozone Monitoring Experiment (GOME) data using a neural network approach (Neu-

ral Network Ozone Retrieval System (NNORSY)). *J. Geophys. Res. Atmos.* 108. URL: <https://agupubs.onlinelibrary.wiley.com/doi/abs/10.1029/2002JD002784>, doi:10.1029/2002JD002784.

¹⁹⁸⁰ Munro, R., Lang, R., Klaes, D., Poli, G., Retscher, C., Lindstrot, R., Huckle, R., Lacan, A., Grzegorski, M., Holdak, A., Kokhanovsky, A., Livschitz, J., Eisinger, M., 2016. The GOME-2 instrument on the Metop series of satellites: instrument design, calibration, and level 1 data processing – an overview. *Atmos. Meas. Tech.* 9, 1279–1301. URL: <https://www.atmos-meas-tech.net/9/1279/2016/>, doi:10.5194/amt-9-1279-2016.

Munro, R., Siddans, R., Reburn, W.J., Kerridge, B.J., 1998. Direct measurement of tropospheric ozone distributions from space. *Nature* 392, 168–171. URL: <https://doi.org/10.1038/32392>, doi:10.1038/32392.

¹⁹⁹⁰ Myhre, G., Shindell, D., Bréon, F.M., Collins, W., Fuglestvedt, J., Huang, J., Koch, D., Lamarque, J.F., Lee, D., Mendoza, B., Nakajima, T., Robock, A., Stephens, G., Takemura, T., Zhang, H., 2013. Anthropogenic and Natural Radiative Forcing. *Climate Change 2013: The Physical Science Basis. Contribution of Working Group I to the Fifth Assessment Report of the Intergovernmental Panel on Climate Change*, 659–740 doi:10.1017/CBO9781107415324.

¹⁹⁹⁵ 018.

²⁰⁰⁰ Nelson, R.R., Crisp, D., Ott, L.E., O'Dell, C.W., 2016. High-accuracy measurements of total column water vapor from the Orbiting Carbon Observatory-2. *Geophys. Res. Lett.* 43, 12,261–12,269. URL: <https://agupubs.onlinelibrary.wiley.com/doi/abs/10.1002/2016GL071200>, doi:10.1002/2016GL071200.

²⁰⁰⁵ Niemeier, U., Timmreck, C., 2015. What is the limit of climate engineering by stratospheric injection of SO₂? *Atmos. Chem. Phys.* 15, 9129–9141. URL: <https://www.atmos-chem-phys.net/15/9129/2015/>, doi:10.5194/acp-15-9129-2015.

- 2005 Ning, T., Wang, J., Elgered, G., Dick, G., Wickert, J., Bradke, M., Sommer, M.,
 Querel, R., Smale, D., 2016. The uncertainty of the atmospheric integrated
 water vapour estimated from GNSS observations. *Atmos. Meas. Tech.* 9, 79–
 92. URL: <https://www.atmos-meas-tech.net/9/79/2016/>, doi:10.5194/
amt-9-79-2016.
- 2010 Noël, S., Buchwitz, M., Bovensmann, H., Hoogen, R., Burrows, J.P., 1999.
 Atmospheric water vapor amounts retrieved from GOME satellite data. *Geo-
 phys. Res. Lett.* 26, 1841–1844. URL: <https://agupubs.onlinelibrary.wiley.com/doi/abs/10.1029/1999GL900437>, doi:10.1029/1999GL900437.
- 2015 Noël, S., Buchwitz, M., Burrows, J.P., 2004. First retrieval of global water
 vapour column amounts from SCIAMACHY measurements. *Atmos. Chem.
 Phys.* 4, 111–125. URL: <https://www.atmos-chem-phys.net/4/111/2004/>,
 doi:10.5194/acp-4-111-2004.
- 2020 Nowlan, C.R., Liu, X., Chance, K., Cai, Z., Kurosu, T.P., Lee, C., Martin,
 R.V., 2011. Retrievals of sulfur dioxide from the Global Ozone Mon-
 itoring Experiment 2 (GOME-2) using an optimal estimation approach:
 Algorithm and initial validation. *Journal of Geophysical Research* 116,
 D18301. URL: <https://agupubs.onlinelibrary.wiley.com/doi/full/10.1029/2011JD015808>, doi:10.1029/2011JD015808.
- 2025 Nowlan, C.R., Martin, R.V., Philip, S., Lamsal, L.N., Krotkov, N.A., Marais,
 E.A., Wang, S., Zhang, Q., 2014. Global dry deposition of nitrogen diox-
 ide and sulfur dioxide inferred from space-based measurements. *Global Bio-
 geochem. Cycles* 28, 1025–1043. URL: <https://agupubs.onlinelibrary.wiley.com/doi/abs/10.1002/2014GB004805>, doi:10.1002/2014GB004805.
- 2030 Palmer, P.I., Abbot, D.S., Fu, T.M., Jacob, D.J., Chance, K., Kurosu,
 T.P., Guenther, A., Wiedinmyer, C., Stanton, J.C., Pilling, M.J., Press-
 ley, S.N., Lamb, B., Sumner, A.L., 2006. Quantifying the seasonal and
 interannual variability of North American isoprene emissions using satel-
 lite observations of the formaldehyde column. *J. Geophys. Res. At-*

mos. 111. URL: <https://agupubs.onlinelibrary.wiley.com/doi/abs/10.1029/2005JD006689>, doi:10.1029/2005JD006689.

Palmer, P.I., Jacob, D.J., Chance, K., Martin, R.V., Spurr, R.J.D., Kurosu, T.P., Bey, I., Yantosca, R., Fiore, A., Li, Q., 2001. Air mass factor formulation for spectroscopic measurements from satellites: Application to formaldehyde retrievals from the Global Ozone Monitoring Experiment. *J. Geophys. Res. Atmos.* 106, 14539–14550. URL: <https://agupubs.onlinelibrary.wiley.com/doi/abs/10.1029/2000JD900772>, doi:10.1029/2000JD900772.

Pan, C., Weng, F., Flynn, L., 2017. Spectral Performance and Calibration of the Suomi NPP OMPS Nadir Profiler Sensor. *Earth Space Sci.* 4, 737–745. URL: <https://agupubs.onlinelibrary.wiley.com/doi/abs/10.1002/2017EA000336>, doi:10.1002/2017EA000336.

Pawson, S., Steinbrecht, W., Charlton-Perez, A., Fujiwara, M., Karpechko, A., Petropavlovskikh, I., Urban, J., Weber, M., 2014. Update on global ozone: Past, present, and future, Chapter 2 in Scientific Assessment of Ozone Depletion: 2014. Technical Report 55. World Meteorological Organization. Geneva, Switzerland. URL: https://www.wmo.int/pages/prog/arep/gaw/ozone_2014/full_report_TOC.html.

Pérez-Ramírez, D., Whiteman, D.N., Smirnov, A., Lyamani, H., Holben, B.N., Pinker, R., Andrade, M., Alados-Arboledas, L., 2014. Evaluation of aeronet precipitable water vapor versus microwave radiometry, gps, and radiosondes at arm sites. *J. Geophys. Res. Atmos.* 119, 9596–9613. URL: <https://agupubs.onlinelibrary.wiley.com/doi/abs/10.1002/2014JD021730>, doi:10.1002/2014JD021730.

Piesanie, A.d., Piters, A.J.M., Aben, I., Schrijver, H., Wang, P., Noël, S., 2013. Validation of two independent retrievals of SCIAMACHY water vapour columns using radiosonde data. *Atmos. Meas. Tech.* 6, 2925–2940. URL: <https://www.atmos-meas-tech.net/6/2925/2013/>, doi:10.5194/amt-6-2925-2013.

Platt, U., 2006. Differential Optical Absorption Spectroscopy, Air Monitoring.
 American Cancer Society. URL: <https://onlinelibrary.wiley.com/doi/abs/10.1002/9780470027318.a0706>, doi:10.1002/9780470027318.a0706.

2065
 Platt, U., Wagner, T., 1998. Satellite mapping of enhanced BrO concentrations in the troposphere. *Nature* 395, 486–490. URL: <https://www.nature.com/articles/26723>, doi:10.1038/26723.

Pope, C.A., Dockery, D.W., 2006. Health Effects of Fine Particulate Air
 2070 Pollution: Lines that Connect. *J. Air Waste Manage. Assoc.* 56, 709–742. URL: <https://www.tandfonline.com/doi/full/10.1080/10473289.2006.10464485>.

Pope, R.J., Chipperfield, M.P., Savage, N.H., Ordonez, C., Neal, L.S., Lee, L.A.,
 Dhomse, S.S., Richards, N.A.D., Keslake, T.D., 2015. Evaluation of a regional
 2075 air quality model using satellite column NO₂: treatment of observation errors and model boundary conditions and emissions. *Atmos. Chem. Phys.* 15, 5611–5626. URL: <https://www.atmos-chem-phys.net/15/5611/2015/>, doi:10.5194/acp-15-5611-2015.

Rasool, Q.Z., Zhang, R., Lash, B., Cohan, D.S., Cooter, E., Bash, J., Lamsal,
 L.N., 2016. Enhanced representation of soil NO emissions in the Community
 Multiscale Air Quality (CMAQ) model version 5.0.2. *Geosci. Model Dev.*
 2080 9, 3177–3197. URL: <https://www.geosci-model-dev.net/9/3177/2016/>, doi:10.5194/gmd-9-3177-2016.

Rawcliffe, R.D., Elliott, D.D., 1966. Latitude distribution of ozone at high
 2085 altitudes, deduced from a satellite measurement of the Earth's radiance at 2840 Å. *J. Geophys. Res.* 71, 5077–5089. URL: <https://agupubs.onlinelibrary.wiley.com/doi/abs/10.1029/JZ071i021p05077>, doi:10.1029/JZ071i021p05077.

Richter, A., Begoin, M., Hilboll, A., Burrows, J.P., 2011. An improved
 2090 NO₂ retrieval for the GOME-2 satellite instrument. *Atmos. Meas. Tech.*

4, 1147–1159. URL: <https://www.atmos-meas-tech.net/4/1147/2011/>, doi:10.5194/amt-4-1147-2011.

Richter, A., Wittrock, F., Eisinger, M., Burrows, J.P., 1998. GOME observations of tropospheric BrO in northern hemispheric spring and summer 1997. *Geophys. Res. Lett.* 25, 2683–2686. URL: <https://agupubs.onlinelibrary.wiley.com/doi/abs/10.1029/98GL52016>, doi:10.1029/98GL52016.

Richter, D., Weibring, P., Walega, J.G., Fried, A., Spuler, S.M., Taubman, M.S., 2015. Compact highly sensitive multi-species airborne mid-IR spectrometer. *Appl. Phys. B* 119, 119–131. URL: <https://doi.org/10.1007/s00340-015-6038-8>, doi:10.1007/s00340-015-6038-8.

Rix, M., Valks, P., Hao, N., Loyola, D., Schlager, H., Huntrieser, H., Flemming, J., Koehler, U., Schumann, U., Inness, A., 2012. Volcanic SO₂, BrO and plume height estimations using GOME-2 satellite measurements during the eruption of Eyjafjallajökull in May 2010. *J. Geophys. Res. Atmos.* 117, 1–19. URL: <https://agupubs.onlinelibrary.wiley.com/doi/abs/10.1029/2011JD016718>, doi:10.1029/2011JD016718.

Rodgers, C.D., 2000. Inverse Methods for Atmospheric Sounding. World Scientific. URL: <https://www.worldscientific.com/doi/abs/10.1142/3171>, doi:10.1142/3171.

Saiz-Lopez, A., Chance, K., Liu, X., Kurosu, T.P., Sander, S.P., 2007. First observations of iodine oxide from space. *Geophys. Res. Lett.* 34. URL: <https://agupubs.onlinelibrary.wiley.com/doi/abs/10.1029/2007GL030111>, doi:10.1029/2007GL030111.

Salawitch, R.J., Canty, T., Kurosu, T., Chance, K., Liang, Q., da Silva, A., Pawson, S., Nielsen, J.E., Rodriguez, J.M., Bhartia, P.K., Liu, X., Huey, L.G., Liao, J., Stickel, R.E., Tanner, D.J., Dibb, J.E., Simpson, W.R., Donohoue, D., Weinheimer, A., Flocke, F., Knapp, D., Montzka, D., Neuman, J.A., Nowak, J.B., Ryerson, T.B., Oltmans, S., Blake, D.R., Atlas,

- 2120 E.L., Kinnison, D.E., Tilmes, S., Pan, L.L., Hendrick, F., Van Roozen-dael, M., Kreher, K., Johnston, P.V., Gao, R.S., Johnson, B., Bui, T.P., Chen, G., Pierce, R.B., Crawford, J.H., Jacob, D.J., 2010. A new interpretation of total column BrO during Arctic spring. *Geophys. Res. Lett.* 37. URL: <https://agupubs.onlinelibrary.wiley.com/doi/abs/10.1029/2010GL043798>.
- 2125 Salawitch, R.J., Weisenstein, D.K., Kovalenko, L.J., Sioris, C.E., Wennberg, P.O., Chance, K., Ko, M.K.W., McLinden, C.A., 2005. Sensitivity of ozone to bromine in the lower stratosphere. *Geophys. Res. Lett.* 32. URL: <https://agupubs.onlinelibrary.wiley.com/doi/abs/10.1029/2004GL021504>.
- 2130 Sander, S., Bekker, D., Blavier, J.F., Bryk, M., Donahue, C., Goullioud, R., Hancock, B., Johnson, D., Key, R., Lamborn, A., Manatt, K., Moore, J., Nastal, J., Neville, T., Preston, D., Rider, D., Ryan, M., Wincentsen, J., Wu, Y.H., 2015. Panchromatic Fourier Transform Spectrometer Engineering Model (PanFTS-EM) for Geostationary Atmospheric Measurements, in: Fourier Transform Spectroscopy and Hyperspectral Imaging and Sounding of the Environment, Optical Society of America. p. FW4A.2. URL: <http://www.osapublishing.org/abstract.cfm?URI=FTS-2015-FW4A.2>, doi:10.1364/FTS.2015.FW4A.2.
- 2140 Sauvage, B., Martin, R.V., van Donkelaar, A., Liu, X., Chance, K., Jaeglé, L., Palmer, P.I., Wu, S., Fu, T.M., 2007. Remote sensed and in situ constraints on processes affecting tropical tropospheric ozone. *Atmos. Chem. Phys.* 7, 815–838. URL: <https://www.atmos-chem-phys.net/7/815/2007/>, doi:10.5194/acp-7-815-2007.
- 2145 Schenkeveld, V.M.E., Jaross, G., Marchenko, S., Haffner, D., Kleipool, Q.L., Rozemeijer, N.C., Veefkind, J.P., Levelt, P.F., 2017. In-flight performance of the ozone monitoring instrument. *Atmos. Meas. Tech.* 10, 1957–1986.

URL: <https://www.atmos-meas-tech.net/10/1957/2017/>, doi:/10.5194/amt-10-1957-2017.

2150 Schröder, M., Lockhoff, M., Fell, F., Forsythe, J., Trent, T., Bennartz, R., Borbas, E., Bosilovich, M.G., Castelli, E., Hersbach, H., Kachi, M., Kobayashi, S., Kursinski, E.R., Loyola, D., Mears, C., Preusker, R., Rossow, W.B., Saha, S., 2018. The GEWEX Water Vapor Assessment archive of water vapour products from satellite observations and reanalyses. *Earth Syst. Sci. Data* 10, 1093–1117. URL: <https://www.earth-syst-sci-data.net/10/1093/2018/>, doi:10.5194/essd-10-1093-2018.

2160 Seftor, C.J., Jaross, G., Kowitz, M., Haken, M., Li, J., Flynn, L.E., 2014. Post-launch performance of the Suomi National Polar-orbiting Partnership Ozone Mapping and Profiler Suite (OMPS) nadir sensors. *J. Geophys. Res. Atmos.* 119, 4413–4428. URL: <https://agupubs.onlinelibrary.wiley.com/doi/abs/10.1002/2013JD020472>, doi:10.1002/2013JD020472.

2165 Seidel, D.J., Berger, F.H., Diamond, H.J., Dykema, J., Goodrich, D., Immel, F., Murray, W., Peterson, T., Sisterson, D., Sommer, M., Thorne, P., Vomel, H., Wang, J., 2009. Reference Upper-Air Observations for Climate: Rationale, Progress, and Plans. *Bull. Amer. Meteor. Soc.* 90, 361–369. URL: <https://journals.ametsoc.org/doi/10.1175/2008BAMS2540.1>, doi:10.1175/2008BAMS2540.1.

2170 Seo, S., Richter, A., Blechschmidt, A.M., Bougoudis, I., Burrows, J.P., 2018. First high resolution BrO column retrievals from TROPOMI. *Atmos. Meas. Tech. Discuss.* 2018, 1–26. URL: <https://www.atmos-meas-tech-discuss.net/amt-2018-365/>, doi:10.5194/amt-2018-365.

2175 Serdyuchenko, A., Gorshelev, V., Weber, M., Chehade, W., Burrows, J.P., 2014. High spectral resolution ozone absorption cross-sections – part 2: Temperature dependence. *Atmos. Meas. Tech.* 7, 625–636. URL: <https://www.atmos-meas-tech.net/7/625/2014/>, doi:10.5194/amt-7-625-2014.

Shim, C., Wang, Y., Choi, Y., Palmer, P.I., Abbot, D.S., Chance, K., 2005.

Constraining global isoprene emissions with Global Ozone Monitoring Experiment (GOME) formaldehyde column measurements. *J. Geophys. Res. Atmos.* 110. URL: <https://agupubs.onlinelibrary.wiley.com/doi/full/10.1029/2004JD005629>, doi:10.1029/2004JD005629.

Silva, S.J., Heald, C.L., Li, M., . Space-based Constraints on Terrestrial Glyoxal Production. *J. Geophys. Res. Atmos.* 123, 13,583–13,594. URL: <https://agupubs.onlinelibrary.wiley.com/doi/abs/10.1029/2018JD029311>, doi:10.1029/2018JD029311.

2185 Simpson, W.R., Brown, S.S., Saiz-Lopez, A., Thornton, J.A., von Glasow, R., 2015. Tropospheric halogen chemistry: Sources, cycling, and impacts. *Chem. Rev.* 115, 4035–4062. URL: <https://doi.org/10.1021/cr5006638>, doi:10.1021/cr5006638.

2190 Simpson, W.R., von Glasow, R., Riedel, K., Anderson, P., Ariya, P., Bottenheim, J., Burrows, J., Carpenter, L.J., Frieß, U., Goodsite, M.E., Heard, D., Hutterli, M., Jacobi, H.W., Kaleschke, L., Neff, B., Plane, J., Platt, U., Richter, A., Roscoe, H., Sander, R., Shepson, P., Sodeau, J., Steffen, A., Wagner, T., Wolff, E., 2007. Halogens and their role in polar boundary-layer ozone depletion. *Atmos. Chem. Phys.* 7, 4375–4418. URL: <https://www.atmos-chem-phys.net/7/4375/2007/>, doi:10.5194/acp-7-4375-2007.

Singer, S.F., Wentworth, R.C., 1957. A method for the determination of the vertical ozone distribution from a satellite. *J. Geophys. Res.* 62, 299–308. URL: <https://agupubs.onlinelibrary.wiley.com/doi/abs/10.1029/JZ062i002p00299>, doi:10.1029/JZ062i002p00299.

2200 Solomon, S., Ivy, D.J., Kinnison, D., Mills, M.J., Neely, R.R., Schmidt, A., 2016. Emergence of healing in the Antarctic ozone layer. *Science* 353, 269–274. URL: <http://science.sciencemag.org/content/353/6296/269>, doi:10.1126/science.aae0061.

- Souri, A.H., Choi, Y., Jeon, W., Woo, J.H., Zhang, Q., Kurokawa, J.i.,
 2205 2017. Remote sensing evidence of decadal changes in major tropospheric ozone precursors over East Asia. *J. Geophys. Res. Atmos.* 122, 2474–2492. URL: <https://agupubs.onlinelibrary.wiley.com/doi/abs/10.1002/2016JD025663>, doi:10.1002/2016JD025663.
- Spinei, E., Whitehill, A., Fried, A., Tiefengrabner, M., Knepf, T.N., Herndon,
 2210 S., Herman, J.R., Müller, M., Abuhaman, N., Cede, A., Richter, D., Walega, J., Crawford, J., Szykman, J., Valin, L., Williams, D.J., Long, R., Swap, R.J., Lee, Y., Nowak, N., Poche, B., 2018. The first evaluation of formaldehyde column observations by improved pandora spectrometers during the korus-aq field study. *Atmos. Meas. Tech.* 11, 4943–4961. URL: <https://www.atmos-meas-tech.net/11/4943/2018/>, doi:10.5194/amt-11-4943-2018.
- Stavrakou, T., Müller, J.F., De Smedt, I., Van Roozendael, M., Kanakidou, M., Vrekoussis, M., Wittrock, F., Richter, A., Burrows, J.P., 2009a. The continental source of glyoxal estimated by the synergistic use of space-borne measurements and inverse modelling. *Atmos. Chem. Phys.* 9, 8431–8446. URL: <https://www.atmos-chem-phys.net/9/8431/2009/>, doi:10.5194/acp-9-8431-2009.
- Stavrakou, T., Müller, J.F., De Smedt, I., Van Roozendael, M., van der Werf, G.R., Giglio, L., Guenther, A., 2009b. Evaluating the performance of pyrogenic and biogenic emission inventories against one decade of space-based formaldehyde columns. *Atmos. Chem. Phys.* 9, 1037–1060. URL: <https://www.atmos-chem-phys.net/9/1037/2009/acp-9-1037-2009.html>, doi:10.5194/acp-9-1037-2009.
- Stavrakou, T., Müller, J.F., De Smedt, I., Van Roozendael, M., van der Werf, G.R., Giglio, L., Guenther, A., 2009c. Global emissions of non-methane hydrocarbons deduced from SCIAMACHY formaldehyde columns through 2003–2006. *Atmos. Chem. Phys.* 9, 3663–3679. URL: <https://www.atmos-chem-phys.net/9/3663/2009/acp-9-3663-2009.html>, doi:10.5194/acp-9-3663-2009.

www.atmos-chem-phys.net/9/3663/2009/acp-9-3663-2009.html, doi:10.5194/acp-9-3663-2009.

Suleiman, R.M., Chance, K., Liu, X., González Abad, G., Kurosu, T.P., Hen-

2235 drick, F., Theys, N., 2018. OMI total bromine monoxide (OMBRO) data product: Algorithm, retrieval and measurement comparisons. *Atmos. Meas. Tech. Discuss.*, 1–33 URL: <https://www.atmos-meas-tech-discuss.net/amt-2018-1/>, doi:10.5194/amt-2018-1.

Thalman, R., Volkamer, R., 2013. Temperature dependent absorption cross-

2240 sections of O₂-O₂ collision pairs between 340 and 630 nm and at atmospherically relevant pressure. *Phys. Chem. Chem. Phys.* 15, 15371–15381. URL: <http://dx.doi.org/10.1039/C3CP50968K>, doi:10.1039/C3CP50968K.

Theys, N., Campion, R., Clarisse, L., Brenot, H., van Gent, J., Dils, B., Cor-

2245 radini, S., Merucci, L., Coheur, P.F., Van Roozendael, M., Hurtmans, D., Clerbaux, C., Tait, S., Ferrucci, F., 2013. Volcanic SO₂ fluxes derived from satellite data: a survey using OMI, GOME-2, IASI and MODIS. *Atmos. Chem. Phys.* 13, 5945–5968. URL: <https://www.atmos-chem-phys.net/13/5945/2013/>, doi:10.5194/acp-13-5945-2013.

Theys, N., De Smedt, I., van Gent, J., Danckaert, T., Wang, T., Hendrick,

2250 F., Stavrakou, T., Bauduin, S., Clarisse, L., Li, C., Krotkov, N., Yu, H., Brenot, H., Van Roozendael, M., 2015. Sulfur dioxide vertical column DOAS retrievals from the Ozone Monitoring Instrument: Global observations and comparison to ground-based and satellite data. *J. Geophys. Res. Atmos.* 120, 2470–2491. URL: <https://agupubs.onlinelibrary.wiley.com/doi/abs/10.1002/2014JD022657>, doi:10.1002/2014JD022657.

Theys, N., De Smedt, I., Yu, H., Danckaert, T., van Gent, J., Hörmann, C.,

2255 Wagner, T., Hedelt, P., Bauer, H., Romahn, F., Pedergnana, M., Loyola, D., Van Roozendael, M., 2017. Sulfur dioxide retrievals from TROPOMI onboard Sentinel-5 Precursor: algorithm theoretical basis. *Atmos. Meas. Tech.*

²²⁶⁰ 10, 119–153. URL: <https://www.atmos-meas-tech.net/10/119/2017/>, doi:10.5194/amt-10-119-2017.

Theys, N., Van Roozendael, M., Dils, B., Hendrick, F., Hao, N., De Maziére, M., 2009. First satellite detection of volcanic bromine monoxide emission after the Kasatochi eruption. *Geophys. Res. Lett.* 36. URL: <https://agupubs.onlinelibrary.wiley.com/doi/abs/10.1029/2008GL036552>, doi:10.1029/2008GL036552.

²²⁷⁰ Thuillier, G., Hersé, M., Labs, D., Foujols, T., Peetermans, W., Gillotay, D., Simon, P.C., Mandel, H., 2003. The Solar Spectral Irradiance from 200 to 2400 nm as Measured by the SOLSPEC Spectrometer from the Atlas and Eureca Missions. *Sol. Phys.* 214, 1–22. URL: <https://doi.org/10.1023/A:1024048429145>, doi:10.1023/A:1024048429145.

²²⁷⁵ Tong, D., Lamsal, L.N., Pan, L., Kim, H., Lee, P., Chai, T., Pickering, K.E., 2015. Long-term NO_x trends over large cities in the United States: Comparison of satellite retrievals, ground observations, and emission inventories. *Atmos. Environ.* 107, 70–84. URL: <http://www.sciencedirect.com/science/article/pii/S1352231015000564>, doi:10.1016/j.atmosenv.2015.01.035.

²²⁸⁰ Toyota, K., McConnell, J.C., Lupu, A., Neary, L., McLinden, C.A., Richter, A., Kwok, R., Semeniuk, K., Kaminski, J.W., Gong, S.L., Jarosz, J., Chipperfield, M.P., Sioris, C.E., 2011. Analysis of reactive bromine production and ozone depletion in the arctic boundary layer using 3-D simulations with GEM-AQ: inference from synoptic-scale patterns. *Atmos. Chem. Phys.* 11, 3949–3979. URL: <https://www.atmos-chem-phys.net/11/3949/2011/>, doi:10.5194/acp-11-3949-2011.

²²⁸⁵ Valin, L.C., Fiore, A.M., Chance, K., González Abad, G., 2016. The role of OH production in interpreting the variability of CH₂O columns in the southeast U.S. *J. Geophys. Res. Atmos.* 121, 478–493. URL: <https://agupubs.onlinelibrary.wiley.com/doi/abs/10.1002/2015JD024012>, doi:10.1002/2015JD024012.

Valks, P., Pinardi, G., Richter, A., Lambert, J.C., Hao, N., Loyola, D.,
 2290 Van Roozendael, M., Emmadi, S., 2011. Operational total and tropospheric NO₂ column retrieval for GOME-2. *Atmos. Meas. Tech.* 4, 1491–1514. URL: <https://www.atmos-meas-tech.net/4/1491/2011/>, doi:10.5194/amt-4-1491-2011.

van der A, R.J., van Oss, R.F., Piters, A.J.M., Fortuin, J.P.F., Meijer, Y.J., Kelder, H.M., 2002. Ozone profile retrieval from recalibrated Global Ozone Monitoring Experiment data. *J. Geophys. Res. Atmos.* 107. URL: <https://agupubs.onlinelibrary.wiley.com/doi/abs/10.1029/2001JD000696>, doi:10.1029/2001JD000696.

van Peet, J.C.A., van der A, R.J., Tuinder, O.N.E., Wolfram, E., Salvador, J., Levelt, P.F., Kelder, H.M., 2014. Ozone ProfilE Retrieval Algorithm (OPERA) for nadir-looking satellite instruments in the UVVIS. *Atmos. Meas. Tech.* 7, 859–876. URL: <https://www.atmos-meas-tech.net/7/859/2014/>, doi:10.5194/amt-7-859-2014.

van Roozendael, M., de Smedt, I., Fayt, C., Wittrock, F., Richter, A., Afe, O., 2004. First Validation of SCIAMACHY BrO Columns. *Atmospheric Chemistry Validation of ENVISAT (ACVE-2)* 562.

Vandaele, A., Hermans, C., Simon, P., Carleer, M., Colin, R., Fally, S., Mrienne, M., Jenouvier, A., Coquart, B., 1998. Measurements of the NO₂ absorption cross-section from 42000 cm⁻¹ to 10000 cm⁻¹ (2381000 nm) at 220 k and 294 k. *J. Quant. Spectrosc. Radiat. Transf.* 59, 171–184. URL: <http://www.sciencedirect.com/science/article/pii/S0022407397001684>, doi:10.1016/S0022-4073(97)00168-4.

Vasilkov, A.P., Joiner, J., Gleason, J., Bhartia, P.K., 2002. Ocean Raman scattering in satellite backscatter UV measurements. *Geophys. Res. Lett.* 29, 18–1–18–4. doi:10.1029/2002GL014955.

Veefkind, J.P., Aben, I., McMullan, K., Förster, H., de Vries, J., Otter, G., Claas, J., Eskes, H.J., de Haan, J.F., Kleipool, Q., van Weele, M., Hasekamp,

- O., Hoogeveen, R., Landgraf, J., Snel, R., Tol, P., Ingmann, P., Voors, R.,
 Kruizinga, B., Vink, R., Visser, H., Levelt, P.F., 2012. TROPOMI on the
 2320 ESA Sentinel-5 Precursor: A GMES mission for global observations of the atmospheric composition for climate, air quality and ozone layer applications.
Rem. Sens. Environ. 120, 70–83. URL: <http://www.sciencedirect.com/science/article/pii/S0034425712000661>, doi:10.1016/j.rse.2011.09.027.
- 2325 Venkateswaran, S.V., Moore, J.G., Krueger, A.J., 1961. Determination of the vertical distribution of ozone by satellite photometry. *J. Geophys. Res.* 66, 1751–1771. URL: <https://agupubs.onlinelibrary.wiley.com/doi/abs/10.1029/JZ066i006p01751>, doi:10.1029/JZ066i006p01751.
- Vigouroux, C., Aquino, B., Augusto, C., Bauwens, M., Becker, C., Blumenthal, T., De Mazière, M., García, O., Grutter, M., Guarin, C., Hannigan, J., Hase, F., Jones, N., Kivi, R., Koshelev, D., Langerock, B., Lutsch, E., Makarova, M., Metzger, J.M., Müller, J.F., Notholt, J., Ortega, I., Palm, M., Paton-Walsh, C., Poberovskii, A., Rettinger, M., Robinson, J., Smale, D., Stavrakou, T., Stremme, W., Strong, K., Sussmann, R., Té, Y., Toon, G., 2018. NDACC harmonized formaldehyde time series from 21 FTIR stations covering a wide range of column abundances. *Atmos. Meas. Tech.* 11, 5049–5073. URL: <https://www.atmos-meas-tech.net/11/5049/2018/amt-11-5049-2018.html>, doi:10.5194/amt-11-5049-2018.
- Vigouroux, C., Hendrick, F., Stavrakou, T., Dils, B., De Smedt, I., Hermans, C., Merlaud, A., Scolas, F., Senten, C., Vanhaelewijn, G., Fally, S., Carleer, M., Metzger, J.M., Müller, J.F., Van Roozendael, M., Maziére, M.D., 2009. Ground-based FTIR and MAX-DOAS observations of formaldehyde at Réunion Island and comparisons with satellite and model data. *Atmos. Chem. Phys.* 9, 9523–9544. URL: <https://www.atmos-chem-phys.net/9/9523/2009/>, doi:10.5194/acp-9-9523-2009.
- 2340 Volkamer, R., Molina, L.T., Molina, M.J., Shirley, T., Brune, W.H., 2005a.

- DOAS measurement of glyoxal as an indicator for fast voc chemistry in urban air. *Geophys. Res. Lett.* 32. URL: <https://agupubs.onlinelibrary.wiley.com/doi/abs/10.1029/2005GL022616>, doi:10.1029/2005GL022616.
- 2350 Volkamer, R., Spietz, P., Burrows, J., Platt, U., 2005b. High-resolution absorption cross-section of glyoxal in the UV-vis and IR spectral ranges. *J. Photochem. Photobiol. A: Chemistry* 172, 35–46. URL: <http://www.sciencedirect.com/science/article/pii/S1010603004005143>, doi:10.1016/j.jphotochem.2004.11.011.
- 2355 von Glasow, R., von Kuhlmann, R., Lawrence, M.G., Platt, U., Crutzen, P.J., 2004. Impact of reactive bromine chemistry in the troposphere. *Atmos. Chem. Phys.* 4, 2481–2497. URL: <https://www.atmos-chem-phys.net/4/2481/2004/>, doi:10.5194/acp-4-2481-2004.
- 2360 Vountas, M., Rozanov, V., Burrows, J., 1998. Ring effect: Impact of rotational Raman scattering on radiative transfer in Earth's atmosphere. *J. Quant. Spectrosc. Radiat. Transf.* 60, 943 – 961. URL: <http://www.sciencedirect.com/science/article/pii/S0022407397001866>, doi:10.1016/S0022-4073(97)00186-6.
- 2365 Vrekoussis, M., Wittrock, F., Richter, A., Burrows, J.P., 2010. GOME-2 observations of oxygenated VOCs: what can we learn from the ratio glyoxal to formaldehyde on a global scale? *Atmos. Chem. Phys.* 10, 10145–10160. URL: <https://www.atmos-chem-phys.net/10/10145/2010/>, doi:10.5194/acp-10-10145-2010.
- 2370 Wagner, T., Beirle, S., Sihler, H., Mies, K., 2013. A feasibility study for the retrieval of the total column precipitable water vapour from satellite observations in the blue spectral range. *Atmos. Meas. Tech.* 6, 2593–2605. URL: <https://www.atmos-meas-tech.net/6/2593/2013/>, doi:10.5194/amt-6-2593-2013.
- 2375 Wagner, T., Heland, J., Zöger, M., Platt, U., 2003. A fast H₂O total column density product from GOME Validation with in-situ aircraft measurements.

- Atmos. Chem. Phys. 3, 651–663. URL: <https://www.atmos-chem-phys.net/3/651/2003/>, doi:10.5194/acp-3-651-2003.
- Walrafen, G.E., 1967. Raman Spectral Studies of the Effects of Temperature on Water Structure. J. Chem. Phys. 47, 114–126. URL: <https://doi.org/10.1063/1.1711834>, doi:10.1063/1.1711834.
- Wang, H., González Abad, G., Liu, X., Chance, K., 2016. Validation and update of OMI Total Column Water Vapor product. Atmos. Chem. Phys. 16, 11379–11393. URL: <https://www.atmos-chem-phys.net/16/11379/2016/>, doi:10.5194/acp-16-11379-2016.
- Wang, H., Liu, X., Chance, K., González Abad, G., Chan Miller, C., 2014. Water vapor retrieval from OMI visible spectra. Atmos. Meas. Tech. 7, 1901–1913. URL: <https://www.atmos-meas-tech.net/7/1901/2014/>, doi:10.5194/amt-7-1901-2014.
- Wang, J., Zhang, L., Dai, A., Van Hove, T., Van Baelen, J., 2007. A near-global, 2-hourly data set of atmospheric precipitable water from ground-based GPS measurements. J. Geophys. Res. Atmos. 112. URL: <https://agupubs.onlinelibrary.wiley.com/doi/abs/10.1029/2006JD007529>, doi:10.1029/2006JD007529.
- Wang, S., Streets, D.G., Zhang, Q., He, K., Kang, D.C.S., Lu, Z., Wang, Y., 2010. Satellite detection and model verification of NO_x emissions from power plants in Northern China. Environ. Res. Lett. 5, 044007. URL: [https://doi.org/10.1088/1748-9326/5/4/044007](https://doi.org/10.1088%2F1748-9326%2F5%2F4%2F044007), doi:10.1088/1748-9326/5/4/044007.
- Wang, S., Zhang, Q., Martin, R.V., Philip, S., Liu, F., Li, M., Jiang, X., He, K., 2015. Satellite measurements oversee China's sulfur dioxide emission reductions from coal-fired power plants. Environ. Res. Lett. 10, 114015. URL: <http://stacks.iop.org/1748-9326/10/i=11/a=114015?key=crossref.12bf840455e95fc2cd51b5d496ef860f>, doi:10.1088/1748-9326/10/11/114015.

- 2405 Wang, W., Flynn, L., Zhang, X., Wang, Y., Wang, Y., Jiang, F., Zhang, Y.,
 Huang, F., Li, X., Liu, R., Zheng, Z., Yu, W., Liu, G., 2012. Cross-Calibration
 of the Total Ozone Unit (TOU) With the Ozone Monitoring Instrument
 (OMI) and SBUV/2 for Environmental Applications. *IEEE Trans. Geo. Rem.
 Sens.* 50, 4943–4955. doi:10.1109/TGRS.2012.2210902.
- 2410 Ware, R.H., Fulker, D.W., Stein, S.A., Anderson, D.N., Avery, S.K., Clark,
 R.D., Droegemeier, K.K., Kuettner, J.P., Minster, J.B., Sorooshian, S.,
 2000. SuomiNet: A Real-Time National GPS Network for Atmospheric
 Research and Education. *BAMS* 81, 677–694. URL: [https://doi.org/10.1175/1520-0477\(2000\)081<0677:SARNGN>2.3.CO;2](https://doi.org/10.1175/1520-0477(2000)081<0677:SARNGN>2.3.CO;2), doi:10.1175/1520-0477(2000)081<0677:SARNGN>2.3.CO;2.
- 2415 Weber, M., Coldewey-Egbers, M., Fioletov, V.E., Frith, S.M., Wild, J.D., Bur-
 rows, J.P., Long, C.S., Loyola, D., 2018. Total ozone trends from 1979 to
 2016 derived from five merged observational datasets – the emergence into
 ozone recovery. *Atmos. Chem. Phys.* 18, 2097–2117. URL: <https://www.atmos-chem-phys.net/18/2097/2018/>, doi:10.5194/acp-18-2097-2018.
- 2420 Wellemeyer, C.G., Bhartia, P.K., Taylor, S., Qin, W., 2004. Version 8 Total
 Ozone Mapping Spectrometer (TOMS) Algorithm, in: Proceedings of the XX
 Quadrennial Ozone Symposium, 1-8 June, Kos, Greece, edited by C. Zerefos,
 Int. Ozone Comm., Athens., pp. 635–641.
- 2425 Wilmouth, D.M., Hanisco, T.F., Donahue, N.M., Anderson, J.G., 1999. Fourier
 Transform Ultraviolet Spectroscopy of the $A^2\Pi_{3/2} \leftarrow X^2\Pi_{3/2}$ Transition of
 BrO. *J. Phys. Chem. A* 103, 8935–8945. URL: <https://doi.org/10.1021/jp991651o>, doi:10.1021/jp991651o.
- 2430 Wittrock, F., Richter, A., Oetjen, H., Burrows, J.P., Kanakidou, M., Myriokefal-
 itakis, S., Volkamer, R., Beirle, S., Platt, U., Wagner, T., 2006. Simultaneous
 global observations of glyoxal and formaldehyde from space. *Geophys. Res.
 Lett.* 33. URL: <https://agupubs.onlinelibrary.wiley.com/doi/abs/10.1029/2006GL026310>, doi:10.1029/2006GL026310.

World Health Organization, 2016. Ambient air pollution: A global assessment of exposure and burden of disease. World Health Organization, Geneva, Switzerland. URL: <https://www.who.int/phe/publications/air-pollution-global-assessment/en/>.

2435 Wu, Y.H., Key, R., Sander, S., Blavier, J.F., Rider, D., 2011. A Panchromatic Imaging Fourier Transform Spectrometer for the NASA Geostationary Coastal and Air Pollution Events Mission. Proc.SPIE 8150, 81500O. URL: <https://doi.org/10.1117/12.892437>, doi:10.1117/12.892437.

2440 Yang, K., Carn, S.A., Ge, C., Wang, J., Dickerson, R.R., 2014. Advancing measurements of tropospheric NO₂ from space: New algorithm and first global results from OMPS. Geophys. Res. Lett. 41, 4777–4786. URL: <https://agupubs.onlinelibrary.wiley.com/doi/abs/10.1002/2014GL060136>, doi:10.1002/2014GL060136.

2445 Yang, K., Dickerson, R.R., Carn, S.A., Ge, C., Wang, J., 2013. First observations of SO₂ from the satellite Suomi NPP OMPS: Widespread air pollution events over China. Geophys. Res. Lett. 40, 4957–4962. URL: <http://doi.wiley.com/10.1002/grl.50952>, doi:10.1002/grl.50952.

2450 Yang, K., Krotkov, N.A., Krueger, A.J., Carn, S.A., Bhartia, P.K., Levelt, P.F., 2007. Retrieval of large volcanic SO₂ columns from the Aura Ozone Monitoring Instrument: Comparison and limitations. J. Geophys. Res. Atmos. 112. URL: <https://agupubs.onlinelibrary.wiley.com/doi/abs/10.1029/2007JD008825>, doi:10.1029/2007JD008825.

2455 Yang, K., Krotkov, N.a., Krueger, A.J., Carn, S.a., Bhartia, P.K., Levelt, P.F., 2009a. Improving retrieval of volcanic sulfur dioxide from backscattered UV satellite observations. Geophys. Res. Lett. 36, L03102. URL: <https://agupubs.onlinelibrary.wiley.com/doi/abs/10.1029/2008GL036036>, doi:10.1029/2008GL036036.

2460 Yang, K., Liu, X., Bhartia, P., Krotkov, N., 2010. Direct retrieval of sulfur

dioxide amount and altitude from spaceborne hyperspectral UV measurements: Theory and application. *J. Geophys. Res.* 115, 1–15. URL: http://so2.gsfc.nasa.gov/pdfs/Yang_KAsatochi_2010JD013982.pdf, doi:10.1029/2010JD013982.

2465

Yang, K., Liu, X., Krotkov, N.a., Krueger, A.J., Carn, S.a., 2009b. Estimating the altitude of volcanic sulfur dioxide plumes from space borne hyper-spectral UV measurements. *Geophys. Res. Lett.* 36, L10803. URL: <http://www.agu.org/pubs/crossref/2009/2009GL038025.shtml>, doi:10.1029/2009GL038025.

2470

Zara, M., Boersma, K.F., De Smedt, I., Richter, A., Peters, E., Van Geffen, J.H.G.M., Beirle, S., Wagner, T., Van Roozendael, M., Marchenko, S., Lam-sal, L.N., Eskes, H.J., 2018. Improved slant column density retrieval of nitrogen dioxide and formaldehyde for OMI and GOME-2A from QA4ECV: inter-comparison, uncertainty characterization, and trends. *Atmos. Meas. Tech.* 2018, 1–47. URL: <https://www.atmos-meas-tech.net/11/4033/2018/>, doi:10.5194/amt-11-4033-2018.

2475

Zhang, C., Liu, C., Wang, Y., Si, F., Zhou, H., Zhao, M., Su, W., Zhang, W., Chan, K.L., Liu, X., Xie, P., Liu, J., Wagner, T., 2018. Preflight Evaluation of the Performance of the Chinese Environmental Trace Gas Monitoring Instrument (EMI) by Spectral Analyses of Nitrogen Dioxide. *IEEE Trans. Geo. Rem. Sens.* 56, 3323–3332. doi:10.1109/TGRS.2018.2798038.

2480

Zhang, L., Jacob, D.J., Boersma, K.F., Jaffe, D.A., Olson, J.R., Bowman, K.W., Worden, J.R., Thompson, A.M., Avery, M.A., Cohen, R.C., Dibb, J.E., Flock, F.M., Fuelberg, H.E., Huey, L.G., McMillan, W.W., Singh, H.B., Weinheimer, A.J., 2008. Transpacific transport of ozone pollution and the effect of recent asian emission increases on air quality in north america: an integrated analysis using satellite, aircraft, ozonesonde, and surface observations. *Atmos. Chem. Phys.* 8, 6117–6136. URL: <https://www.atmos-chem-phys.net/8/6117/2008/>, doi:10.5194/acp-8-6117-2008.

2485

2490

Zhang, L., Jacob, D.J., Liu, X., Logan, J.A., Chance, K., Eldering, A., Bojkov, B.R., 2010. Intercomparison methods for satellite measurements of atmospheric composition: application to tropospheric ozone from TES and OMI. *Atmos. Chem. Phys.* 10, 4725–4739. URL: <https://www.atmos-chem-phys.net/10/4725/2010/>, doi:10.5194/acp-10-4725-2010.

²⁴⁹⁵ Zhang, Q., Streets, D.G., Carmichael, G.R., He, K., Huo, H., Kannari, A., Klimont, Z., Park, I., Reddy, S., Fu, J.S., Chen, D., Duan, L., Lei, Y., Wang, L., Yao, Z., 2009. Asian emissions in 2006 for the NASA INTEX-B mission. *Atmos. Chem. Phys.* 9, 5131–5153. URL: <https://www.atmos-chem-phys.net/9/5131/2009/>, doi:10.5194/acp-9-5131-2009.

Zhang, Y., Li, C., Krotkov, N.A., Joiner, J., Fioletov, V., McLinden, C., 2017. Continuation of long-term global SO₂ pollution monitoring from OMI to OMPS. *Atmos. Meas. Tech* 10, 1495–1509. URL: www.atmos-meas-tech.net/10/1495/2017/, doi:10.5194/amt-10-1495-2017.

²⁵⁰⁰ Zhong, L., Louie, P.K.K., Zheng, J., Yuan, Z., Yue, D., Ho, J.W.K., Lau, A.K.H., 2013. Science-policy interplay: Air quality management in the Pearl River Delta region and Hong Kong. *Atmos. Environ.* 76, 3–10. URL: <http://www.sciencedirect.com/science/article/pii/S1352231013001787>, doi:10.1016/j.atmosenv.2013.03.012.

²⁵¹⁰ Zhu, L., Jacob, D.J., Kim, P.S., Fisher, J.A., Yu, K., Travis, K.R., Mickley, L.J., Yantosca, R.M., Sulprizio, M.P., De Smedt, I., González Abad, G., Chance, K., Li, C., Ferrare, R., Fried, A., Hair, J.W., Hanisco, T.F., Richter, D., Jo Scarino, A., Walega, J., Weibring, P., Wolfe, G.M., 2016. Observing atmospheric formaldehyde (HCHO) from space: validation and intercomparison of six retrievals from four satellites (OMI, GOME2A, GOME2B, OMPS) with SEAC4RS aircraft observations over the southeast US. *Atmos. Chem. Phys.* 16, 13477–13490. URL: <https://www.atmos-chem-phys.net/16/13477/2016/>, doi:10.5194/acp-16-13477-2016.

Zhu, L., Jacob, D.J., Mickley, L.J., Marais, E.A., Cohan, D.S., Yoshida, Y.,

- 2520 Duncan, B.N., González Abad, G., Chance, K.V., 2014. Anthropogenic emissions of highly reactive volatile organic compounds in eastern Texas inferred from oversampling of satellite (OMI) measurements of HCHO columns. Environ. Res. Lett. 9, 114004. URL: <http://stacks.iop.org/1748-9326/9/i=11/a=114004>, doi:10.1088/1748-9326/9/11/114004.
- 2525 Zhu, L., Mickley, L.J., Jacob, D.J., Marais, E.A., Sheng, J., Hu, L., González Abad, G., Chance, K., 2017. Long-term (2005–2014) trends in formaldehyde (HCHO) columns across North America as seen by the OMI satellite instrument: Evidence of changing emissions of volatile organic compounds. Geophys. Res. Lett. 44, 7079–7086. URL: <https://agupubs.onlinelibrary.wiley.com/doi/abs/10.1002/2017GL073859>, doi:10.1002/2017GL073859.
- 2530 Ziemke, J.R., Chandra, S., Bhartia, P.K., 1998. Two new methods for deriving tropospheric column ozone from toms measurements: Assimilated uars mls/haloe and convective-cloud differential techniques. J. Geophys. Res. Atmos. 103, 22115–22127. URL: <https://agupubs.onlinelibrary.wiley.com/doi/abs/10.1029/98JD01567>, doi:10.1029/98JD01567.
- 2535 Ziemke, J.R., Chandra, S., Duncan, B.N., Froidevaux, L., Bhartia, P.K., Lev elt, P.F., Waters, J.W., 2006. Tropospheric ozone determined from Aura OMI and MLS: Evaluation of measurements and comparison with the Global Modeling Initiative's Chemical Transport Model. J. Geophys. Res. Atmos. 111. URL: <https://agupubs.onlinelibrary.wiley.com/doi/abs/10.1029/2006JD007089>, doi:10.1029/2006JD007089.
- 2540 Zoogman, P., Liu, X., Suleiman, R.M., Pennington, W.F., Flittner, D.E., Al Saadi, J.A., Hilton, B.B., Nicks, D.K., Newchurch, M.J., Carr, J.L., Janz, S.J., Andraschko, M.R., Arola, A., Baker, B.D., Canova, B.P., Chan Miller, C., Cohen, R.C., Davis, J.E., Dussault, M.E., Edwards, D.P., Fishman, J., Ghulam, A., González Abad, G., Grutter, M., Herman, J.R., Houck, J., Jacob, D.J., Joiner, J., Kerridge, B.J., Kim, J., Krotkov, N.A., Lamsal, L., Li,

- C., Lindfors, A., Martin, R.V., McElroy, C.T., McLinden, C., Natraj, V.,
2550 Neil, D.O., Nowlan, C.R., OSullivan, E.J., Palmer, P.I., Pierce, R.B., Pippin,
M.R., Saiz-Lopez, A., Spurr, R.J.D., Szykman, J.J., Torres, O., Veefkind,
J.P., Veihelmann, B., Wang, H., Wang, J., Chance, K., 2017. Tropospheric
emissions: Monitoring of pollution (TEMPO). *J. Quant. Spectrosc. Radiat. Transf.* 186, 17–39. URL: <http://www.sciencedirect.com/science/article/pii/S0022407316300863>, doi:10.1016/j.jqsrt.2016.05.008.
2555

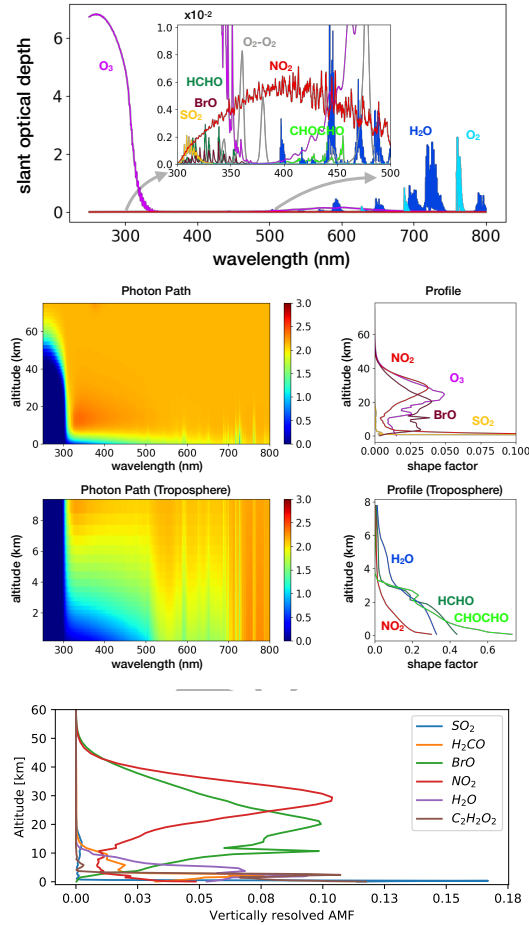


Figure 2: Top panel: slant optical depths of the strongest absorbers. Middle left panels: simulated photon path detected by satellite sensors as functions of wavelength and atmospheric pressure for 30° SZA, 0° VZA and homogeneous 0.1 surface reflectance. Simulations shown here were performed with the VLIDORT RTM for a Rayleigh atmosphere and molecular absorption from O₃, NO₂, O₂, O₂-O₂ and H₂O plus other minor species not relevant for the calculation of the photon paths. Middle right panels: shape factors for the different species assumed in the simulations. To enhance the spectral signatures of weak absorbers the simulations have considered high atmospheric loading of SO₂ and C₂H₂O₂. Bottom panel: vertically resolved AMFs computed at 326 nm (SO₂), 340 nm (H₂CO and BrO) and 440 nm (NO₂, H₂O and C₂H₂O₂).

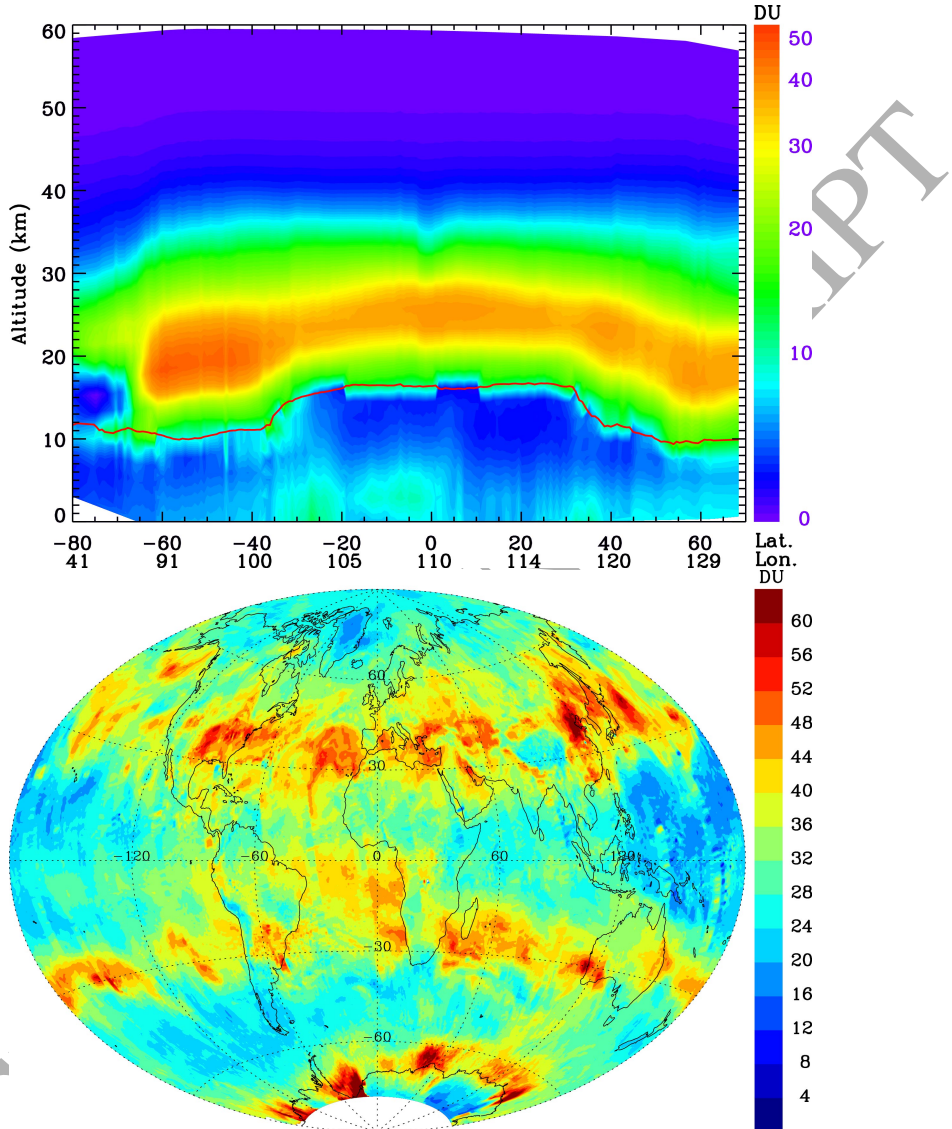


Figure 3: Upper panel shows an orbit of partial (layer) column O₃ (DU) profiles retrieved using GOME-1 measurements for orbit 71022024 on 22 October 1997. The red lines indicates the tropopause height. Lower pannel shows a global map of OMI tropospheric O₃ column on 26 August 2006 gridded to 0.5° longitude \times 0.5° latitude grid cells. Some systematic cross-track position dependent biases have been removed before gridding by assuming these data do not vary with cross-track position within a month.

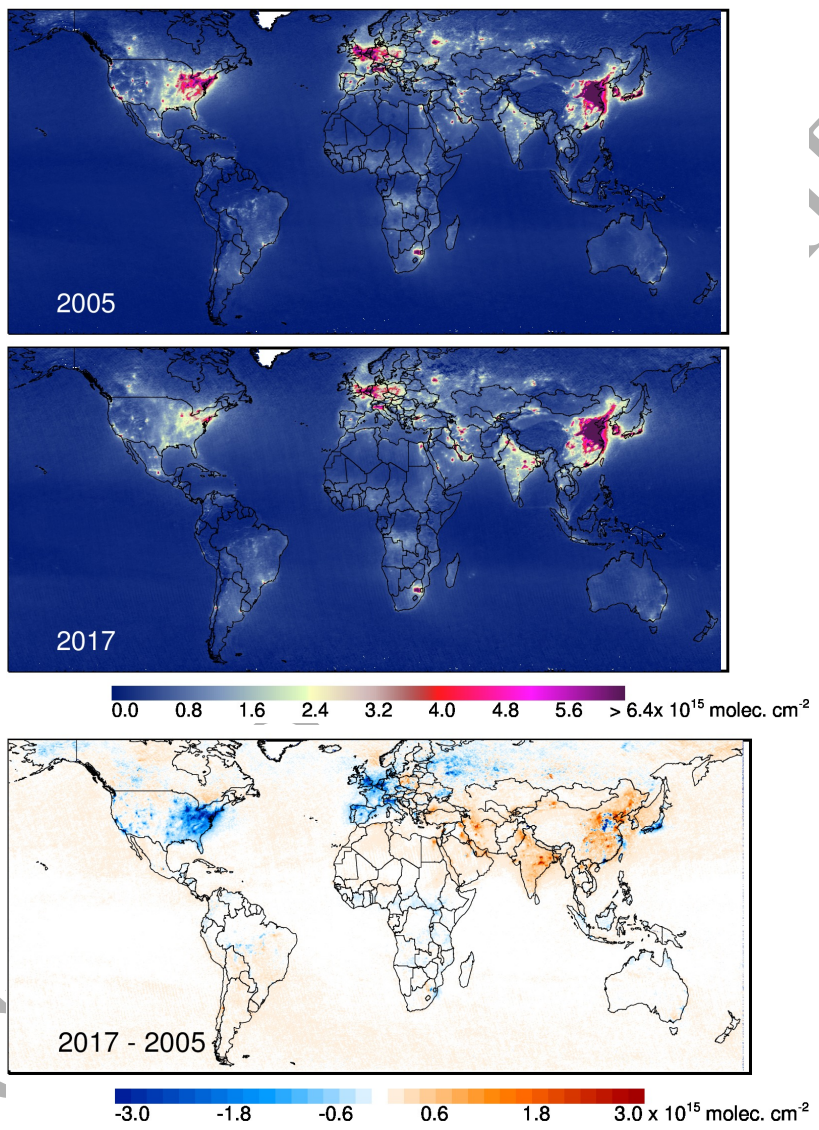


Figure 4: Annual average OMI tropospheric NO₂ VCDs at 0.25° latitude × 0.25° longitude spatial resolution for 2005 (top) and 2017 (middle). Bottom panel shows changes in tropospheric NO₂ VCDs between 2005 and 2017.

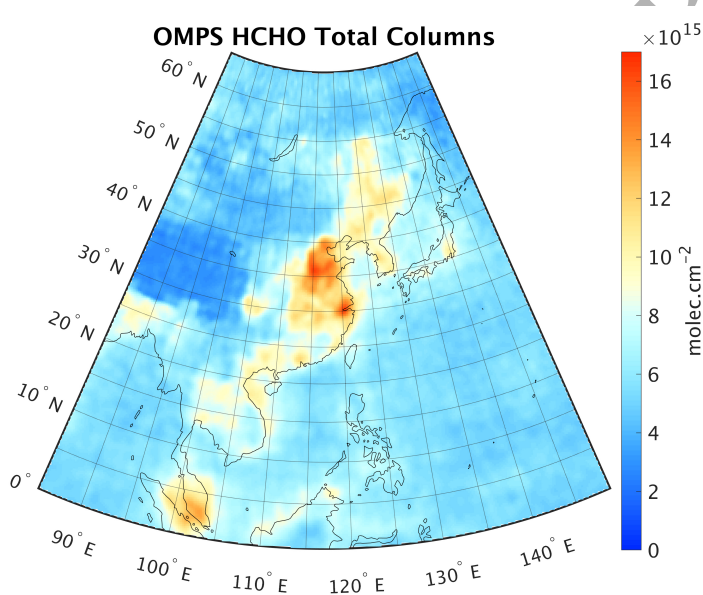


Figure 5: H_2CO columns observed by the OMPS-NM sensor on-board S-NPP satellite over East Asia. Observations for the months of June and July 2015 are over-sampled to a $27 \times 27 \text{ km}^2$ grid. H_2CO enhancements linked to urban concentrations can be appreciated over China, South Korea and Japan as well as biogenic and pyrogenic signatures in Indonesia.

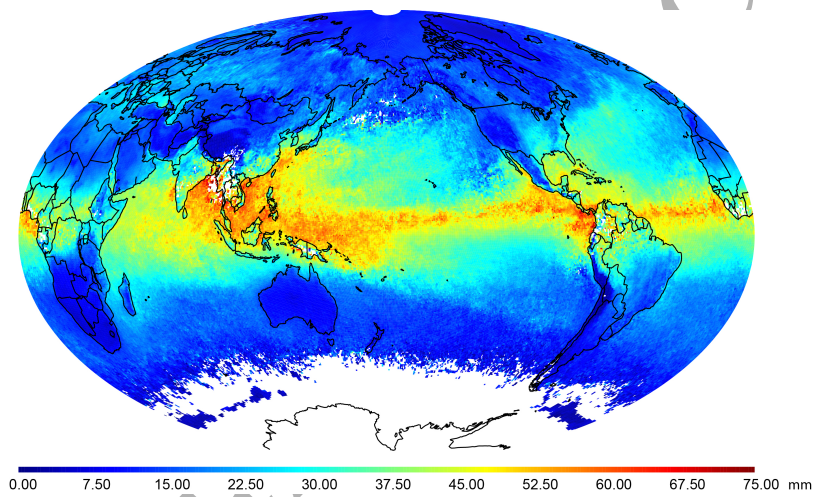


Figure 6: Global TCWV observed by the OMI instrument. Only observations with cloud fractions below 5% for the months of June, July and August 2006 are included in the average at each $0.5^\circ \times 0.5^\circ$ grid.